Charge dynamics in superconducting double dots

ADAM ASHIQ ESMAIL

Fitzwilliam College, University of Cambridge

October 2017

This dissertation is submitted for the degree of

Doctor of Philosophy

Dedicated to my father
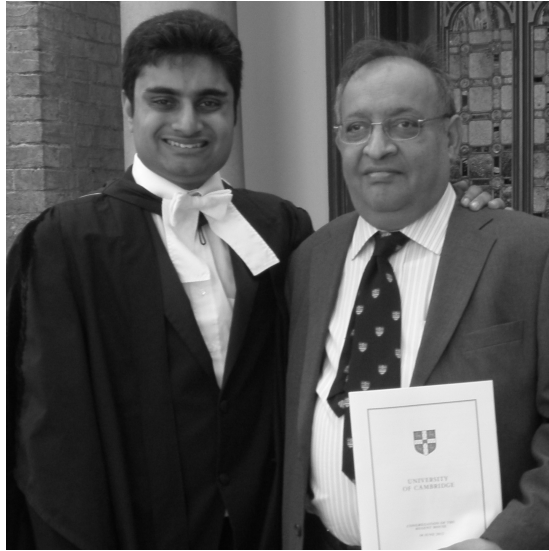
Dr A. F. Esmail

1950 - 2016

Declaration

This dissertation is my own work and contains nothing which is the outcome of work done in collaboration with others, except where specified in the text. This dissertation is not substantially the same as any that I have submitted for a degree or diploma or other qualification at any other university. This dissertation does not exceed the prescribed limit of 60,000 words.

List of Publications

The majority of the results in this thesis have been published in peer-reviewed journals as follows:

[1] N. J. Lambert, M. Edwards, **A. A. Esmail**, F. A. Pollock, S. D. Barrett, B. W. Lovett and A. J. Ferguson. "Experimental observation of the breaking and recombination of single Cooper pairs," *Physical Review B* **90**, 140503(R) (2014).

[2] N. J. Lambert, **A. A. Esmail**, M. Edwards, F. A. Pollock, B. W. Lovett, and A. J. Ferguson. "Quantum capacitance and charge sensing of a superconducting double dot," *Applied Physics Letters* **109**, 112603 (2016).

[3] N. J. Lambert, **A. A. Esmail**, F. A. Pollock, M. Edwards, B. W. Lovett and A. J. Ferguson. "Microwave irradiation and quasiparticles in a superconducting double dot," *Physical Review B* **95** 235413 (2017).

Contributions towards the experimental work

The results presented in this thesis are a result of a valiant team effort, and I wish to clarify the contributions to the project.

For the results presented in Chapter 4, device design and fabrication was carried out jointly between myself and Dr Nicholas Lambert. Experimental measurements were carried out by Dr Lambert. Theoretical analyses were carried out jointly by myself and Dr Lambert.

For the results presented in Chapters 5 & 6, device design and fabrication was carried out jointly between myself and Dr Nicholas Lambert. Experimental measurements were carried out between myself, Dr Lambert and Dr Megan Edwards. Theoretical analyses were carried out by myself, Dr Lambert and Dr Edwards and in collaboration with Dr Felix Pollock from Oxford University and Dr Brendon Lovett from University of St. Andrews.

For the results presented in Chapter 7, device design, fabrication, measurements and analyses were carried out by myself exclusively.

All of the work described above has been under the supervision of Dr Andrew Ferguson and Dr Nicholas Lambert.

Adam A. Esmail,
University of Cambridge 2017

ACKNOWLEDGEMENTS

My time as a PhD student has been a bit of a roller-coaster. There have been some stressful times, but most of it was rewarding, stimulating and, most importantly, fun. There are many people who I'd like to acknowledge for the work gone into this thesis.

I would first like to thank Dr Andrew Ferguson, who has been an enthusiastic and attentive supervisor. I decided to join his group when I noticed his passion and kindness, both of which continued throughout my time as a student. I wish him well in his new position at Evonetix Ltd.

A gargantuan token of my gratitude goes to Dr Nicholas Lambert, who has been the driving force for the superconducting double dot. Nick started out as my post-doc advisor, guiding me through almost all of the technical skills that I have gained. When he later ended up as my supervisor, he was extremely meticulous in his proofreading of this thesis. I don't think I could have asked for a better advisor, and he has also been a good friend too.

Dr Megan Edwards has been a wonderful colleague for most of my time here. I have very fond memories of her as my lab-buddy and fellow occupant of "The Cell". She is now in an important role in the Houses of Parliament, and I am very proud to have her as a friend. My thanks also goes to my other Cell occupants, Dr Tim Skinner, Dr Vahe Tshitoyan, Zhou Fang and Imtiaz Ahmed, for their company.

I would like to acknowledge our collaborators, Prof. Brendon Lovett and Dr Felix Pollock, for their contributions to the project, and also to Dr Malcolm Connolley and Vivek Chidambaram for their fruitful discussions about superconducting devices.

In addition, I would like to thank the group staff: Radoslav Chakolav for his training and guidance in the clean-room, and the group secretaries Emily Heavens-Ward and Emma Ball, for helping out at times of personal crisis.

I must also thank past and present members of the Microelectronics Group and Hitachi Laboratory for their help. Far too many to mention, but I would like to thank

CHARGE DYNAMICS IN SUPERCONDUCTING DOUBLE DOTS
ADAM A. ESMAIL

The work presented in this thesis investigates transitions between quantum states in the superconducting double dot (SDD), a nanoscale device consisting of two aluminium superconducting islands coupled together by a Josephson junction, with each dot connected to a normal state lead. The energy landscape consists of a two level manifold of even charge parity Cooper pair states, and continuous bands corresponding to charge states with single quasiparticles in one or both islands.

These devices are fabricated using shadow mask evaporation, and are measured at sub Kelvin temperatures using a dilution refrigerator. We use radio frequency reflectometry to measure quantum capacitance, which is dependent on the quantum state of the device.

We measure the quantum capacitance as a function of gate voltage, and observe capacitance maxima corresponding to the Josephson coupling between even parity states. We also perform charge sensing and detect odd parity states. These measurements support the theoretical model of the energy landscape of the SDD.

By measuring the quantum capacitance in the time domain, we observe random switching of capacitance between two levels. We determine this to be the stochastic breaking and recombination of single Cooper pairs. By carrying out spectroscopy of the bath responsible for the pair breaking we attribute it to black-body radiation in the cryogenic environment. We also drive the breaking process with a continuous microwave signal, and find that the rate is linearly proportional to incident power. This suggests that a single photon process is responsible, and demonstrates the potential of the SDD as a single photon microwave detector. We investigate this mechanism further, and design an experiment in which the breaking rate is enhanced when the SDD is in the antisymmetric state rather than the symmetric state.

We also measure the quantum capacitance of a charge isolated double dot. We observe $2e$ periodicity, indicating the tunnelling of Cooper pairs and the lack of occupation of quasiparticle states.

This work is relevant to the range of experiments investigating the effect of non-equilibrium quasiparticles on the operation of superconducting qubits and other superconducting devices.

CONTENTS

INTRODUCTION

Superconducting circuits have major applications in nanoelectronics; examples include amplifiers for microwave and radio-frequency signals [4, 5], ultra-sensitive magnetic field detectors [6], photon detectors for astronomy [7], and solid-state electronic refrigeration [8]. Recently, superconducting devices have become promising candidates for scalable quantum information processing [9], one of the latest developments being from IBM, whose "IBM Quantum Experience" is a cloud-based universal quantum computing platform where users can remotely perform experiments and algorithms on a 5 superconducting transmon qubit quantum processor [10].

The attraction of superconducting devices mainly stems from the supercurrent: conduction electrons pair up into *Cooper pairs*, a quantum entangled state which is immune to scattering by low energy vibrations or radiation. Cooper pairs can be broken by phonons or photons with energies greater than or equal to twice an energy gap (known as the superconducting gap) into single particle excitations known as *Bogoliubov quasiparticles* [11]. Operating these devices at millikelvin temperatures, with the use of a dilution refrigerator, suppresses these excitations at thermal equilibrium [12]. However, stray radiation may break Cooper pairs, generating non-equilibrium quasiparticle excitations [13]. As quasiparticle recombination is thermally suppressed, these non-equilibrium quasiparticles have a long lifetime. These are generally a nuisance for superconducting devices, causing decoherence in qubits

[14, 15] and limiting the performance of microwave resonators [16] and solid-state refrigerators [17]. On the other hand, the ability to generate non-thermal quasiparticles has shown benefits for single photon detection [18] and Cooper pair splitting [19, 20].

The work presented in this thesis is related to the *superconducting double dot* (SDD), a device designed as a Cooper pair splitter which retains the quasiparticles. The pair breaking and recombination processes are observed by recording the impedance of the device in real time, The results contribute to our understanding of quasiparticle dynamics in superconducting nanostructures, and therefore build on the work of these applications, whether the goal is to encourage or suppress the generation of non-equilibrium quasiparticles.

In this introduction, I briefly discuss the key aspects of superconductivity and nanodevices, and review the literature on quasiparticles in superconducting devices. I give the motivation to the project and my thesis outline at the end of the chapter.

1.1 Summary of Superconductivity

Superconductivity was discovered in 1911 by H. Kamerlingh Onnes [21]. Onnes found that when a sample of mercury is cooled below 4.2 K (by being immersed in liquid helium), the electrical resistance vanishes and a resulting dissipationless *supercurrent* flows though the sample. Onnes later observed the same phenomenon in tin and lead, although at different transition temperatures of 6 K and 4 K respectively. This *perfect conductivity* is one of the key properties of superconductors, and is the prerequisite for most applications, such as high-current transmission lines and high-field magnets [11, 21].

In 1933, Meissner and Ochsenfield discovered another key property of superconductors - *perfect diamagnetism*. Meissner and Ochsenfield found that magnetic fields (up to a critical field strength) are excluded from entering a superconductor, and are expelled when the metal is cooled through its transition temperature, also known as the superconducting critical temperature T_c. This is known as the "Meissner effect" [22].

These two phenomena could not be explained until a macroscopic theory was presented by Ginzburg and Landau in 1950, which treated the superconducting transition as a second-order phase transition. In 1957, Abrikosov used this theory

to predict Type II superconductors, which, instead of completely expelling magnetic field, can trap magnetic flux in quantised vortices.

Also in 1957, Bardeen, Cooper and Schrieffer (BCS) laid out the theory of the microscopic nature of conventional superconductors[a][23, 24]. The BCS theory of superconductivity states that when a metal is cooled below T_c, an effective attraction between electrons overcomes the Coulomb repulsive force, causing the electrons to pair up into Cooper pairs. These pairs form a bosonic-like condensate in the ground state of the superconductor. All of the pairs are phase coherent with each other, meaning that they can be described by a single macroscopic wavefunction. For conduction electrons to exist without a pair, they have to overcome an energy barrier known as the superconducting gap, Δ. Breaking a single pair results in the creation of two quasiparticles, both of which are superpositions of electrons and holes [11]. The nature of these Cooper pairs and quasiparticles is discussed in more detail in Chapter 2, section 2.1.

1.2   Josephson junctions and applications

In 1962, Brian Josephson [25] predicted that two superconductors separated by a thin insulating barrier carry a zero-voltage supercurrent. Josephson presented two equations which describe how the difference in phase of the order parameter between the two superconductors varies with an applied current or voltage [26]. These Josephson effects are discussed in detail in Chapter 2, section 2.3.2.

One of the most notable applications of Josephson junctions is as components of SQUIDs (superconducting quantum inference devices), which are most commonly used as magnometers (highly sensitive detectors of magnetic fields, with typical field sensitivities of 3 - 5 fT Hz$^{-1/2}$ [6, 27]) in several commercial applications. The most widely available commercial system is the Magnetic Property Measurement System (MPMS) by Quantum Design, which uses a SQUID array gradiometer to measure the magnetic properties of a sample, such as its intrinsic magnetic moment and magnetic susceptibility. The temperature of the sample can be varied between 2 and 400 K, and the magnetic field from zero to ± 7 T. The MPMS has found applications throughout the breadth of the natural sciences; in physics (e.g. high-T_c

---

[a]In this thesis, we will only consider the theory of BCS s-wave superconductors (e.g. aluminium).

superconductors), chemistry (fullerenes), material science (ceramics), geology (sea-bed lava) and biology (iron concentrations in chlorophyll) [27]. SQUID arrays are also used in medicine for magnetoencephalography (for detection of neural activity in the brain) [28] and magnetocardiography (for detecting magnetic fields produced by the heart) [29]. Other applications of SQUIDs include their use as biosensors for magnetically marked antigens [30], components of radio frequency amplifiers [5], and microtesla resolution nuclear magnetic resonance (NMR) [31] and magnetic resonance imaging (MRI) [32].

Josephson junctions also play an important role in metrology. When a Josephson junction is driven by an AC current with frequency f, then the current-voltage curve of the junction develops constant voltage steps at values of $nhf/2e$, where n is an integer, h is Planck's constant and e is the elementary charge. Hence, the output voltage of the junction only depends on the driving frequency (which is usually stable to 1 part in 10^{12}) and fundamental constants. This application of the AC Josephson effect has led to the development of the Josephson voltage standard, a system consisting of a large array of Josephson junctions (up to 20,000) which provides the basis for voltage standards in modern science. These devices provide a stable DC voltage reference of ±10 V with an accuracy of 1 part in 10^9 or better, and are used for calibration in over 50 national, industrial and military laboratories around the world [33, 34, 35].

1.3 Superconducting devices involving quasiparticle generation

There have been developments in novel applications of Josephson devices, including qubits, single photon detectors, solid-state refrigeration, and the production of quantum-entangled electrons. All of these devices involve the generation of non-equilibrium quasiparticle excitations. In some cases, these quasiparticles adversely affect the performance of the device, but in other cases are key to their operation. This section goes through each of these examples in detail.
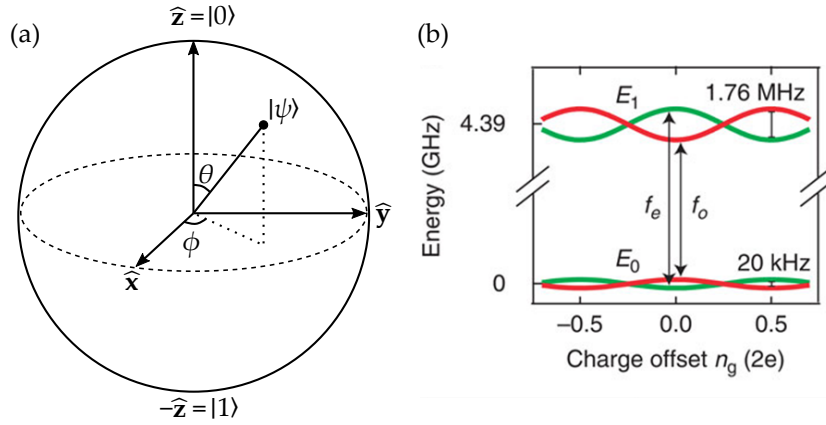
Figure 1.1: (a) The Bloch sphere representation of a qubit state $|\psi\rangle$. The north and south poles of the sphere correspond to the qubit basis vectors $|0\rangle$ and $|1\rangle$. States along the equator are superpositions of $|0\rangle$ and $|1\rangle$ with equal weight ($\theta = \pi/2$) with a phase difference between them parametrised by the azimuthal angle ϕ. (b) The energies of a transmon qubit as a function of gate charge for an even (green) and odd (red). When a quasiparticle tunnels onto or off the island of the transmon, the qubit transition frequency changes between f_e and f_o. The random shifts between these two frequencies cause the loss of the phase information of the qubit, i.e. the qubit decoheres. Diagram from Riste et al. [36]

1.3.1 Superconducting qubits and decoherence

1.3.1.1 Introduction to the qubit

Quantum computation exploits the superposition of quantum states to process tasks in parallel. Certain computational tasks, such as the prime factorisation of many-digit numbers, would not be possible to perform within a reasonable timescale on a conventional computer; but would take only seconds on a quantum computer [37]. The building blocks of such a computer are quantum bits, or *qubits*. Qubits are two level systems which can be in a linear superposition of their logical states $|0\rangle$ and $|1\rangle$. Their state can be written as

$$|\psi\rangle = \cos\left(\frac{\theta}{2}\right)|0\rangle + e^{i\phi}\sin\left(\frac{\theta}{2}\right)|1\rangle, \tag{1.1}$$

which is represented geometrically on the Bloch sphere (Fig. 1.1(a)). In a system of N qubits, the overall wavefunction is a superposition of 2^N logical states. Quantum algorithms are used to run computation on all 2^N classical inputs. This demonstrates *quantum parallelism* and is the key reason for the computational power of a quantum computer [38].

However, qubits are easily disturbed by interactions with the environment and can rapidly collapse from a phase-coherent superposition to a mixed state. This is known as *decoherence*, and is caused by two mechanisms: energy exchange between the qubit and enviroment (relaxation) and fluctuations in the qubit transition frequency due to the qubit-environment coupling (dephasing) [39, 40].

The relaxation of the qubit to its ground state (i.e. the decay of co-ordinate θ) represents the corruption of classical information and is characterised by the relaxation time T_1. The decoherence of the qubit (i.e. the loss of a coherent phase ϕ) represents the corruption of quantum information and is characterised by the coherence time T_2 [41]. T_1 and T_2 are fundamentally linked by the equation

$$\frac{1}{T_2} = \frac{1}{2T_1} + \Gamma_\phi,\qquad(1.2)$$

where Γ_ϕ is known as the pure dephasing rate [42]. T_1 imposes an upper bound on the coherence time $T_2 \leq 2T_1$ [40].

There have been numerous implementations of qubits, including (but not limited to) the superconducting circuits [43], charges and spins in semiconductors [44, 45] and trapped ions [46]. Building a quantum computer using superconducting circuits for qubits has significant potential to be successful, due to the ability to create a scalable architecture with multiple superconducting qubits that can be entangled [47, 48].

1.3.1.2 Superconducting charge qubits

In 1997, Nakamura et al. [49] demonstrated the first superconducting charge qubit (known as a *Cooper pair box*), showing spectroscopically the superposition of Cooper pair states $|n\rangle$ and $|n + 1\rangle$, where the integer n is the quantum number specifying the number of Cooper pairs [50]. The operation of the Cooper pair box qubit is discussed in detail in Chapter 2, section 2.3.3.

Cooper pair box qubits are susceptible to low-frequency charge noise. This causes random shifts in qubit resonant frequency, scrambling the phase of the qubit and leading to dephasing. More advanced charge qubits have been recently developed, such as the transmon [51, 52], quantronium [53] and gatemon [54], which are designed to be less sensitive to charge noise, and show an improvement in T_2 as a result [39].

Scalable quantum computing requires entangled quantum states, which requires the qubits to be coupled to each other via some intermediate interaction. This has been

demonstrated using cavity quantum electrodynamics (cQED), with transmon qubits embedded into superconducting coplanar waveguide resonators [55]. In these systems, there has been groundbreaking progress in microwave qubit control [56], qubit-photon entanglement [57], dispersive readout [58], multi-qubit entanglement [59, 60] and universal two-qubit gate operations [61]. There has also been intense development in improving the coherence times in such systems, in particular the invention of a transmon embedded in a 3D-cavity has led to coherence times increasing towards 0.1 ms [62, 63].

1.3.1.3 Quasiparticle poisoning

The generation of non-equilibrium quasiparticles in superconducting qubits induces decoherence via both relaxation and dephasing. This is caused by *quasiparticle poisoning*, where a single quasiparticle randomly hops on and off the qubit island [64, 65, 66, 67]. Relaxation is mediated by energy exchange between the qubit and the environment via quasiparticle tunnelling [68]. Dephasing is caused by the stochastic shifting of the energy bandstructure by the charge of one electron, e, causing the transition energy of the two level system to fluctuate [40].

There have been many studies of quasiparticle poisoning of Cooper pair box qubits [69, 70, 71], superconducting single electron transistors [72, 73, 74], and transmon qubits [62, 36, 15, 75]. The role of quasiparticles in these devices is usually investigated by comparing the theoretical quasiparticle lifetime rates with the measured qubit relaxation and decoherence times. For example, Riste et al. [36] detect quasiparticle tunnelling in their transmon qubit by measuring the shift of qubit frequency due to parity switching (Fig. 1.1(b)). They find that the relaxation time does not decrease with temperature below 150 mK, indicating a non-equilibrium quasiparticle density similar to that measured in other superconducting devices. The authors comment that quasiparticle generation can be suppressed with additional shielding from background radiation [13].

Quasiparticle poisoning can be reduced by implementing normal metal traps where quasiparticles tunnel to and relax their energy [74, 76]. This is not always successful, however; Sun et al. find that traps do not significantly improve the lifetimes of their transmons qubits [15]. Recently, superconducting vortices have been shown to trap quasiparticles in transmon qubits; Wang et al. [77] demonstrate that by having device

electrodes of larger area, more vortices form to trap quasiparticles, which leads to improvements in coherence times.

As a further example, Gustavsson et al. [78] use control pulses to reduce quasiparticle population in a flux qubit. This involves repeatedly forcing qubit relaxation to excite quasiparticles into states with a larger group velocity. This causes the diffusion rate of the quasiparticles to increase, resulting in them rapidly leaving the qubit junction. The authors demonstrate a reduction in quasiparticle population by 70% and an improvement in relaxation times by a factor of three.

1.3.2 Noise in superconducting resonators
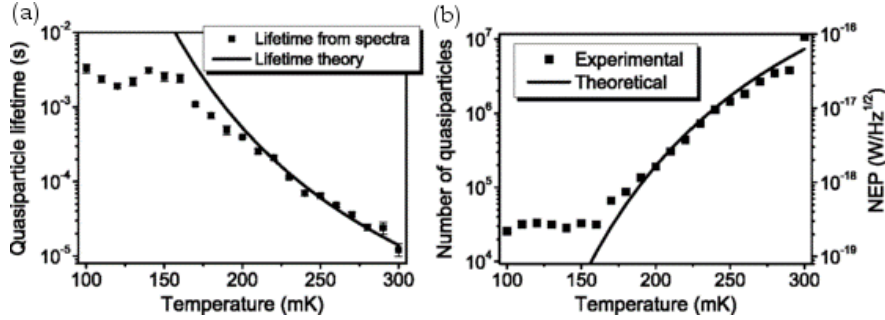
Figure 1.2: (a) Quasiparticle lifetime as a function of temperature and (b) Quasiparticle population (and NEP) as a function of temperature. These graphs from [16] demonstrate the effect of remnant quasiparticles on the noise floor of superconducting resonators.

A key application for microwave resonators is microwave photon detection (as kinetic inductance detectors or KIDs) for radio astronomy [79]. The quasiparticle density, which is proportional to the number of incident photons, is measured via the surface impedance of the device. Random quasiparticle generation and recombination, induced by stray radiation, cause a noise which limits the energy resolution (sensitivity) of the detector [80]. De Visser et al. [81, 16, 82] have extensively investigated ways to improve this senstivity. The authors find that a minimum population of non-equilibrium quasiparticles remain in the resonator below 160 mK (Fig. 1.2), which limits the noise equivalent power to 1.5×10^{-19}W/Hz$^{1/2}$. Despite this, the authors comment that the resonators would be suitable for spectroscopy in radio astronomy [16].

1.3.3 Limiting the cooling power of on-chip electronic refrigerators
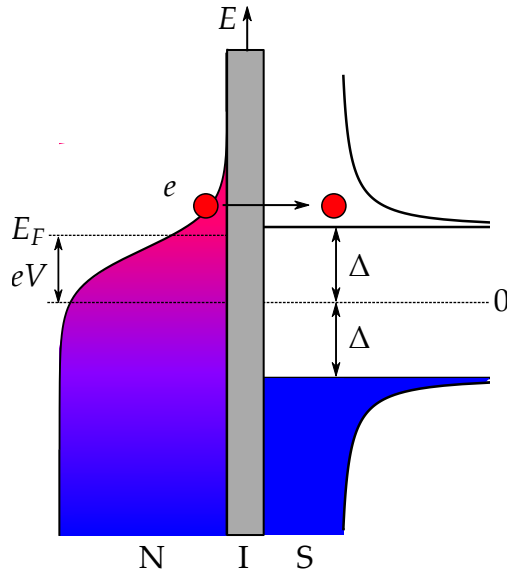
Figure 1.3: Sketch of the energy-band diagram of a voltage-biased NIS junction. When a voltage bias is applied across the structure, the most energetic electrons (above the Fermi energy E_F) can tunnel into the superconductor. As a result, the electron gas in the normal metal is cooled [83].

On-chip electronic refrigerators are designed to cool nanodevices to a lower temperature than that of the surrounding bath. They are usually based on either normal-insulator-superconductor (NIS) or superconductor-insulator-superconductor (SIS) junctions [8]. A schematic diagram of the cooling mechanism is shown in Fig. 1.3. When an optimal bias is applied (such that the magnitude of the bias, eV, is just over the gap energy of the superconductor) across an NIS junction, the "hot" electrons above the Fermi level tunnel out of the metal, resulting in the cooling of the metal [17]. Such devices have been used to cool astronomical detectors [83], and remove non-equilibrium quasiparticles from superconducting qubits [8, 84]. However, non-equilibrium quasiparticles generated in the superconducting electrodes limit the cooling power. Quasiparticle traps have been shown to improve cooling efficiency in SINIS junctions by removing the remnant quasiparticles from the electrodes [76]. The most impressive electronic cooling with such devices has been demonstrated by Nguyen et al. [85]. Their best device demonstrates on-chip cooling from 150 mK down

to about 30 mK, a factor of 5 in temperature at a cooling power of 40 pW.

1.3.4   Single photon detection
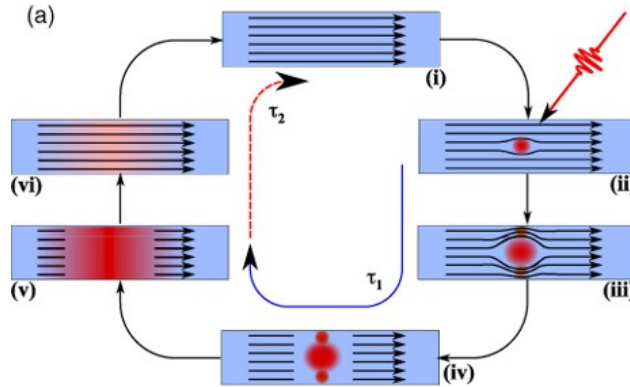
Figure 1.4: A diagram showing the process of quasiparticle generation in single nanowire single photon detectors. Diagram from [18].

Other than KIDs, various superconducting devices have been used to detect photons, but the first to demonstrate this at the single photon limit was the superconducting tunnel junction (STJ) [7]. A photon is detected when a quasiparticle current is measured. These devices are usually used in radio astronomy for frequencies in the range 30 - 1500 GHz [86].

For applications in quantum information, the ability to detect single photons is essential for quantum key distribution (QKD). Such a system transmits and receives cryptographic keys encoded in the polarisation or phase of photons. An eavesdropper intercepting these photons will dephase the qubits and the sabotage attempt is revealed. Single photon detectors for this application need a high quantum efficiency - the probability of detecting an incident photon. In terms of quasiparticle dynamics, fast recombination times would allow short reset times (i.e. the time taken for detector to go back to its detection state after it has registered a count), which would increase this efficiency. Minimising generation-recombination noise would also minimise the dark count (number of false readings) and hence improve measurement fidelity [87].

Recent advances in optical and infrared photon detection involve the superconducting nanowire single photon detector (SNSPD), as shown in Fig. 1.4. Photons incident on the nanowire generate a "hot-spot" of quasiparticles. This hot-

spot region is in the normal state, and constricts the supercurrent in the nanowire to the edge. As the current density exceeds the critical current density, the wire becomes resistive and the current drops. The quasiparticles relax via phonon interactions and the nanowire goes back to its superconducting state [18]. These devices have been successful in QKD experiments over distances of 200 km [88].

1.3.5 Cooper pair splitter as a source of entangled spin pairs
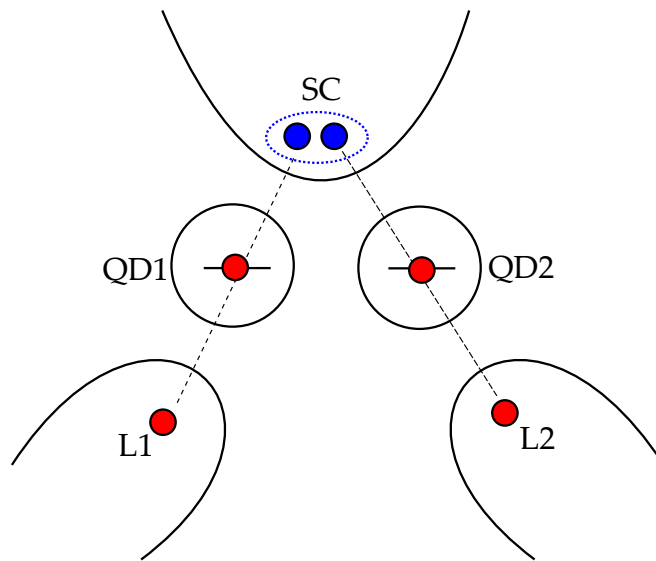
Figure 1.5: Conceptual diagram of the Andreev entangler. A Cooper pair tunnels out of the superconductor (SC). If the quantum dots (QD1, QD2) are tuned to be in the Coulomb blockade regime, the charging energy will be greater than the superconducting gap and so the Cooper pair will split. One quasiparticle tunnels onto QD1 and the other onto QD2. They then tunnel onto their neighbouring normal leads (L1, L2) [89].

Cooper pairs in conventional s-wave superconductors have singlet spin-wavefunctions

$$|\psi\rangle = \frac{1}{\sqrt{2}} \left(|\uparrow\downarrow\rangle - |\downarrow\uparrow\rangle \right), \tag{1.3}$$

and can therefore act as a natural source of spin-entangled electrons. The energy cost associated into splitting these Cooper pairs into their constituent quasiparticle states is 2Δ. In devices known as *Andreev entanglers*, Cooper pairs split into two spin-entangled quasiparticles, and each quasiparticle coherently tunnels onto separate tunable quantum dots (Fig. 1.5) [89]. This makes it possible in order to perform Bell-

state like measurements and to demonstrate the non-locality of quantum mechanical phenomena [90]. Such devices have been realised using InAs nanowires [19, 20] and carbon nanotubes [91], with a 90% splitting efficiency having been demonstrated in the latter [92].

1.4 Motivations

In summary, there are two principal processes in which non-equilibrium quasiparticles are generated in superconducting devices: quasiparticles tunnelling into the system, and Cooper pairs breaking into quasiparticles. Consequently, non-equilibrium quasiparticles are reduced either by quasiparticles tunnelling out of the system (usually onto quasiparticle traps), or by quasiparticles recombining to form Cooper pairs.

Quasiparticle tunnelling in superconducting structures have been studied extensively, particularly in structures which involve quasiparticle poisoning of superconducting charge qubits (Section 1.3.1.3). Quasiparticle tunnelling rates are inferred via the parity switching rate of the device; for example, in Cooper pair box qubits and superconducting SETs, the capacitance of the device is dependent on its parity. This means that as quasiparticles tunnel on and off the island of the device, the capacitance of the device changes stochastically in real time. The resulting random telegraph signals (RTSs) are analysed to determine the rates of switching between the poisoned and unpoisoned states (i.e. the rates of quasiparticle tunnelling from lead to island, and island to lead) [93]. Observations of individual quasiparticle tunnelling events has allowed a deep theoretical understanding of how quasiparticles behave in these structures under different conditions, such as changes in temperature or magnetic field [70].

However, the dynamics of quasiparticles due to pair breaking are less understood. Quasiparticles generated via pair breaking are common in KIDs, where average quasiparticle numbers are typically over 1000 [79, 16]. In such systems, only the average quasiparticle lifetimes (i.e. the reciprocal of the average recombination rate) are considered. Maisi et al. [94] have observed and studied pair breaking and recombination events in their devices, consisting of a superconducting island connected to normal leads. The authors observe pair breaking when injecting quasiparticles into the island, and infer the rates for these processes from the magnitude

of the quasiparticle tunnelling current. However, individual pair breaking events are not observed.

In this thesis, I present results in superconducting double dot devices, where single pair breaking and recombination events have been observed in real time by measuring the capacitance of the device embedded in an *LC* circuit. The analyses of pair breaking and recombination rates build on our understanding of quasiparticle dynamics in superconducting devices.

A further motivation is to study the dynamics of quasiparticle spins. The SDD is a similar device to the semiconductor double quantum dot (DQD) in that both systems have states in which a single spin is occupied in each dot. There have been numerous investigations of spin dynamics in DQDs [95, 96, 97, 44], and it has been predicted that by using similar techniques, it may also be possible to measure spin lifetimes and coherence times of quasiparticles in the SDD [98]. This is discussed further in Chapter 8, Section 8.2.2.

1.5 Thesis Outline

In Chapter 2 of this thesis, I discuss the background theory and observations leading up to the superconducting double dot. In Chapter 3, I present the superconducting double dot and experimental evidence of its energy landscape. In Chapter 4, I discuss the fabrication and measurement techniques. In Chapter 5, I present observations of Cooper pair breaking in the SDD and describe how the SDD has potential as a photon click detector. This is continued in Chapter 6, where the pair breaking rate is made to be dependent on the initial Cooper pair state. In Chapter 7, I present results for a galvanically isolated SDD. In Chapter 8, I draw together my conclusions from each chapter and discuss the further work for the SDD to reach its full potential.

HAPTER

<div align="right">

CHAPTER **2**

</div>

<div align="center">

T**HEORETICAL BACKGROUND**

</div>

The superconducting double dot can be thought of as a hybrid of a superconducting charge qubit and a double quantum dot. In this Chapter, I describe the theory behind these two subjects. I first outline the origin of Cooper pairs and quasiparticles in superconductors, including how quasiparticles are generated. I then discuss the physics of single charge devices, such as the single electron transistor and double dot systems. This is extended to the superconducting case, where we see a difference in energy between states with an even and odd number of electrons. I introduce the Josephson energy, leading onto the derivation of the energy states of a superconducting qubit. In the last section, I discuss quantum capacitance, a quantity proportional to the curvature of the energy states with respect to the gate voltages. This allows the states of a superconducting qubit to be read out without a charge sensor.

2.1 Electronic behaviour in superconductors

2.1.1 Cooper pairing of electrons

In metals, electrons can interact with the lattice and each other via virtual phonons. For electrons with energies $E_F - \hbar\omega_D < E < E_F + \hbar\omega_D$, where ω_D is the Debye phonon frequency, this interaction is an effective *attractive* electron-electron interaction. In superconductors, the material parameters are such that this attractive force overcomes

the repulsive Coulomb interaction. This effect is strongest for electrons with opposite momentum $(k, -k)$ and spin $(\sigma = \uparrow, \downarrow)$ and these electrons pair up with each other[24]. These correlated pairs of electrons are known as *Cooper pairs*.

Bardeen et al. [23] describes the ground state of a superconductor as a many-body phase-coherent (BCS) wavefunction

$$|\Psi_{BCS}\rangle = \prod_k \left(u_k + v_k c^{\dagger}_{k,\uparrow} c^{\dagger}_{-k,\downarrow} \right) |0\rangle . \tag{2.1}$$

The operator $c^{\dagger}_{k,\sigma}$ is the creation operator, which creates an electron with momentum k and spin σ. There exists a corresponding annihilation operator $c_{k,\sigma}$, which is the Hermitian conjugate of the creation operator. This form of the BCS wavefunction implies that the probability of the paired state $(k \uparrow, -k \downarrow)$ being occupied is $|v_k|^2$, whereas the probability that it is unoccupied is $|u_k|^2 = 1 - |v_k|^2$. This wavefunction does not have a well defined number of electrons, but is a coherent superposition of configurations with different even numbers of additional electrons compared to the vacuum state $|0\rangle$ [11].

2.1.2 BCS Hamiltonian

The Hamiltonian for this pairing mechanism is

$$H = \sum_{k,\sigma} \epsilon_k n_{k,\sigma} - \sum_{k,k'} V_{k,k'} c^{\dagger}_{k,\uparrow} c^{\dagger}_{-k,\downarrow} c_{-k',\downarrow} c_{k',\uparrow} \tag{2.2}$$

where $n_{k,\sigma} = c^{\dagger}_{k,\sigma} c_{k,\sigma}$ is the number operator. The first term describes the kinetic energy of an electron with energy relative to the Fermi energy $\epsilon_k = \hbar^2 k^2 / 2m - E_F$. The second term describes the pairing, where $V_{k,k'}$ is the energy required to break a pair with $(k' \uparrow, -k' \downarrow)$ and form a pair with $(k \uparrow, -k \downarrow)$.

Originally, Bardeen et al. determined the coefficients u_k and v_k by using a Hartree-like variational method [23]. In this thesis, I will outline an approach using a canonical transformation (from Introduction to Superconductivity by M. Tinkham[11]) to find these coefficients. This will satisfy our understanding of *Bogoliubov quasiparticles* (or quasiparticles, as I shall call them from now on) as excitations in a superconductor.

2.1.3 Solution using canonical transformation

The uncertainty of the number state in the coherent state $|\Psi_{BCS}\rangle$ leads to fluctuations around the mean number of electrons. This means that the pair creation and

annihilation operators can have non-zero expectation values

$$\left\langle c_{k,\uparrow}^{\dagger} c_{-k,\downarrow}^{\dagger} \right\rangle = b_k^*, \quad \left\langle c_{-k,\downarrow} c_{k,\uparrow} \right\rangle = b_k. \tag{2.3}$$

Here, b_k are the fluctuations in the field operators $\left(c_{k,\uparrow}^{\dagger} c_{-k,\downarrow}^{\dagger}, c_{-k,\downarrow} c_{k,\uparrow} \right)$.

We consider these fluctuations to first order by writing the pair operators in the form

$$c_{-k,\downarrow} c_{k,\uparrow} = b_k + (c_{-k,\downarrow} c_{k,\uparrow} - b_k). \tag{2.4}$$

We also define

$$\Delta_k = -\sum_{k'} V_{k,k'} b_{k'}. \tag{2.5}$$

Subsituting Eqns. 2.4 and 2.5 into 2.2, we get

$$H = \sum_{k,\sigma} \epsilon_k c_{k,\sigma}^{\dagger} c_{k,\sigma} + \sum_k \left(\Delta_k c_{k,\uparrow}^{\dagger} c_{-k,\downarrow}^{\dagger} + \Delta_k^* c_{-k,\downarrow} c_{k,\uparrow} - \Delta_k b_k^* \right). \tag{2.6}$$

This Hamiltonian can be diagonalised via the Bogoliubov transformation

$$c_{k,\uparrow} = u_k^* \gamma_{k0} + v_k \gamma_{k1}^{\dagger} \tag{2.7a}$$

$$c_{-k,\downarrow}^{\dagger} = -v_k^* \gamma_{k0} + u_k \gamma_{k1}^{\dagger} \tag{2.7b}$$

where $\gamma_k^{(\dagger)}$ is an operator which annihilates (creates) quasiparticle excitations from the superconducting ground state. The subscripts in this representation, u_k and v_k, can be chosen so that the products $\gamma_{k1} \gamma_{k0}$ and $\gamma_{k0}^{\dagger} \gamma_{k1}^{\dagger}$ are zero. The resulting equations are

$$\begin{pmatrix} \epsilon_k & \Delta_k \\ \Delta_k^* & -\epsilon_k \end{pmatrix} \begin{pmatrix} u_k \\ v_k \end{pmatrix} = E_k \begin{pmatrix} u_k \\ v_k \end{pmatrix}. \tag{2.8}$$

Solving this equation gives the eigenenergies

$$E_k = \pm \sqrt{\epsilon_k^2 + |\Delta_0|^2}, \tag{2.9}$$

and the normalisation coefficients

$$|v_k|^2 = 1 - |u_k|^2 = \frac{1}{2}\left(1 - \frac{\epsilon_k}{E_k}\right). \tag{2.10}$$

Δ_k is the energy gap between the ground and excited states of a superconductor. In the BCS approximation, this gap does not depend on k, so $\Delta_k \equiv \Delta$ [99].
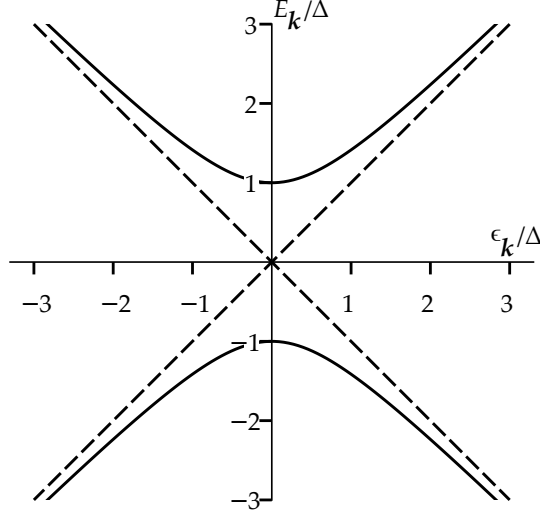
Figure 2.1: The energies for elementary excitations in the normal (dashed line) and superconducting (solid line) as functions of $\epsilon_k = \hbar^2|\boldsymbol{k}|^2/2m - E_F$, the independent kinetic energy relative to the Fermi energy [11].

2.1.4 Quasiparticles in a superconductor

Cooper pairs exist in a bosonic-like[a] condensate at the ground state (Fermi) energy, E_F. Quasiparticles, however, are fermions and their energy states exist in an energy band starting Δ above the Fermi energy.

The eigenenergies of the BCS Hamiltonian in Eqn. 2.9 are plotted with ϵ_k in Fig. 2.1. The presence of the superconducting gap makes little difference to the nature of quasiparticles, except near the Fermi energy ($\epsilon_k = 0$). For $\epsilon_k \gg 0$, the quasiparticle is essentially an electron, much like in the normal state, and for $\epsilon_k \ll 0$, it is essentially a hole. However, near $\epsilon_k = 0$, the quasiparticle is a superposition of an electron and hole. This can be seen from the quasiparticle creation operators

$$\gamma_{k0}^\dagger = u_k^* c_{k,\uparrow}^\dagger - v_k^* c_{-k,\downarrow}, \tag{2.11a}$$

$$\gamma_{k1}^\dagger = u_k^* c_{-k,\downarrow}^\dagger + v_k^* c_{k,\uparrow}, \tag{2.11b}$$

which we can get by inverting Eqns. 2.7.

For $\epsilon_k \gg 0$, $u_k \approx 1$ and the quasiparticle creation operators are equivalent to electron creation operators. For $\epsilon_k \ll 0$, $v_k \approx 1$, the operators are equivalent to hole

---

[a]The creation/annihilation operators $[c_{-k,\downarrow} c_{k,\uparrow}]^{(\dagger)}$ of Cooper pairs do not obey the commutation relations for bosons.

18

creation operators. At $\epsilon_k = 0$, the operators are an equal superposition of the electron and hole creation operators. The same applies for the quasiparticle annihilation operators, γ_{k0}.

In metals, a single particle excitation is obtained by occupying a state E_1 above the Fermi level, leaving a vacancy E_2 below the Fermi level [24]. The energy of this excitation is

$$E_1 - E_2 = \epsilon_1 - \epsilon_2 = |\epsilon_1| + |\epsilon_2| . \tag{2.12}$$

Quasiparticle excitations in superconductors are created in the same way, except that the energy of the excitation is now

$$\begin{aligned} E_1 - E_2 &= \sqrt{\epsilon_1^2 + \Delta^2} + \sqrt{\epsilon_2^2 + \Delta^2} \\ &\geq 2\Delta. \end{aligned} \tag{2.13}$$

Hence the spectroscopic superconducting gap is 2Δ, rather than Δ [11].

Unlike excitations in metals, however, quasiparticle excitations are charge neutral at $\epsilon_k = 0$. In the case of a single electron from a metal being injected to a superconductor, the resulting quasiparticle carries spin of 1/2 but no charge - a consequence of the perfect screening of charge and of the Meissner effect. The extra e of charge resides in the distortion of the number of Cooper pairs [100].

2.1.4.1 Temperature dependence of Δ

The temperature dependence of Δ is given by

$$\Delta(T) = D(E_F)V\Delta(T) \int_0^{\hbar\omega_D} E^{-1} \tanh\left(\frac{E}{2k_BT}\right) d\epsilon. \tag{2.14}$$

This expression can be solved numerically. For weak-coupling superconductors ($\hbar\omega_D/k_BT \gg 1$), $\Delta(T)/\Delta(0)$ is a universal function of T, which decreases monotonically from 1 at $T = 0$ to zero at the superconducting critical temperature, T_c. For aluminium, $T_c = 1.2$K. Near $T = 0$, the temperature variation is exponentially slow since $e^{-\Delta/k_BT} \approx 0$, so the hyperbolic tangent is very nearly unity and insensitive to T. Physically, Δ is nearly constant until a significant number of quasiparticles are thermally excited. Near T_c, $\Delta(T)$ drops to zero with a vertical tangent, approximately as

$$\frac{\Delta(T)}{\Delta(T = 0)} \approx 1.74 \times \sqrt{1 - \frac{T}{T_c}}. \tag{2.15}$$

The solution for Eqn. 2.14 at T = 0 gives

$$\Delta(T = 0) = 1.76 k_B T_c, \tag{2.16}$$

which has been tested for many experiments with conventional superconductors and found to be reasonable [11]. For bulk aluminium, $\Delta(T = 0) \approx 182\,\mu\text{eV}$.

2.1.4.2 Magnetic field dependence of Δ

The magnetic field dependence of Δ is given by

$$\frac{\Delta(B)}{\Delta_0} = \sqrt{1 - \frac{B^2}{B_c^2}}, \tag{2.17}$$

where B_c is the critical magnetic field, and Δ_0 is the energy gap at $B = 0$. For bulk aluminium, $B \approx 10$ mT [101].

For thin film aluminium (thickness $d < 200$nm), the critical in-plane field strength increases with decreasing thickness as $B_c \sim d^{-3/2}$ [102]. Δ_0 also increases with decreasing film thickness [103].

2.1.5 BCS density of states

The quasiparticle spectrum is described by the BCS density of states (DOS), which is

$$D_S(E) = \begin{cases} D(E_F)\frac{E}{\sqrt{E^2 - \Delta^2}} & (|E| > \Delta) \\ 0 & (|E| < \Delta), \end{cases} \tag{2.18}$$

where $D(E_F)$ is the single-spin normal-state density of states at the Fermi energy. This is a constant depending on the material and for aluminium $D(E_F) = 1.72 \times 10^{10} \mu\text{m}^{-3}\,\text{eV}^{-1}$ [16]. A plot of $D_S(E)$ against energy, E is plotted in Fig. 2.2, denoting the occupation of the states at $T = 0$.

The BCS DOS has singularity at $E = \Delta$ and no states between $-\Delta < E < \Delta$. In practice, strong coupling between electrons and phonons leads to a finite lifetime of quasiparticles, which broadens the DOS near $E = \Delta$. This lifetime smearing was first measured by Dynes et al. [104] in PbBi, where the effect is prominent due to the strong electron-phonon interaction. The adjusted "Dynes" density of states is

$$D_S^D(E) = \left| \Re\left(\frac{E/\Delta + i\gamma}{\sqrt{(E/\Delta + i\gamma)^2 - 1}} \right) \right|, \tag{2.19}$$
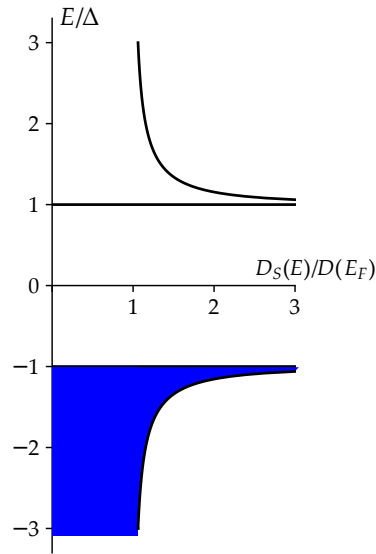
Figure 2.2: The BCS density of states of quasiparticles in a superconductor. The Fermi Energy, E_F is at $E = 0$. States above the Fermi energy are electron-like and states below are hole-like. At T = 0, all hole-like states are occupied (denoted in blue) and all electron-like states are unoccupied [11].

where γ is the Dynes broadening parameter. This introduces states within the gap region $|E| < \Delta$.

2.1.5.1 Thermal occupation

The number of quasiparticles in a superconductor of volume V in thermal equilibrium can be calculated by integrating the product of the BCS DOS and the occupation probability of the quasiparticle states, the Fermi-Dirac distribution $f(E) = (\exp(E/k_B T) + 1)^{-1}$, over all energies:

$$N_{qp} = 2V \int_{\Delta}^{\infty} f(E) D_S(E) dE. \tag{2.20}$$

The factor of 2 comes from the fact that we should also integrate over the negative energies (hole-like quasiparticles) [17]. This expression can be simplified for very low temperatures where $\Delta/(k_B T) \gg 1$. In this approximation

21

$$N_{qp} \approx 2\sqrt{2\pi\Delta k_B T} V D(E_F) \exp\left(\frac{-\Delta}{k_B T}\right),$$

$$\equiv N_{eff} \exp\left(\frac{-\Delta}{k_B T}\right). \tag{2.21}$$

This expression describes the number occupancy of a state with a Boltzmann probability $e^{\frac{-E}{kT}}$, energy $E = \Delta$, and a degeneracy $N_{eff} = 2\sqrt{2\pi\Delta k_B T} V D(E_F)$. We call N_{eff} the number of quasiparticle states available for thermal excitation. This approximation is valid in the low temperature regime as all excitations are low in energy (i.e. near the quasiparticle band edge). For mesoscopic islands $V \approx 1\mu m$, typically $N_{eff} \approx 10^4$. We will come back to this quantity during the discussion on the parity effect.

This result was first approximated by Tuominen et al. [64], and calculated exactly by Shaw et al. [70]. For completeness, a derivation is included in Appendix A.

2.1.5.2 Generation and recombination

Quasiparticles are generated by phonons or photons with energy $E \geq 2\Delta$ breaking Cooper pairs. Quasiparticles with opposite momentum and spin may also recombine to form a Cooper pair, emitting a phonon in the process. These process are stochastic, meaning that individual generation or recombination events occur at random intervals. In thermal equilibrium, the (average) generation and recombination rates are equal. The instantaneous number of quasiparticles, N_{qp} fluctuates in time about a steady-state average $\bar{N}_{qp}$ with a standard deviation of $\sqrt{\bar{N}_{qp}}$. [105].

The rate of change of quasiparticles are given by the first Rothwarf-Taylor equation

$$\frac{dN_{qp}}{dt} = 2\left(\frac{P}{2\Delta} + \Gamma_B N_\omega - \frac{1}{2}\frac{R}{V}N_{qp}^2\right). \tag{2.22}$$

The first term in this equation is the probability per unit time of quasiparticles generated via photons with $hf > 2\Delta$. P is the power of radiation absorbed by the electrode. The second term is the probability per unit time of thermal quasiparticle generation. Γ_B is the rate at which phonons break pairs and generate quasiparticles[b]. The final term is the probability per unit time of quasiparticle recombination. R is the recombination constant - a constant of proportionality between the rate and the number

---

[b]This rate is proportional to the number of Cooper pairs in the superconductor, but this number is much larger than the number of generated quasiparticles so we can approximate it as a constant.

of ways to combine N quasiparticles, which is $N^2/2$. For a pair of quasiparticles at the band edge ($E = \Delta$)

$$R = \frac{2\Delta^2}{\tau_0 D(E_F)(k_B T_c)^3},$$ (2.23)

where τ_0 is the material dependent electron-phonon coupling constant. N_ω is the number of phonons in the electrode, which also changes with time according to the second Rothwarf-Taylor equation

$$\frac{dN_\omega}{dt} = -\Gamma_B N_\omega + \frac{1}{2}\Gamma_R N_{qp} - \Gamma_{es}(N_\omega - \bar{N}_\omega),$$ (2.24)

where $\bar{N}_\omega$ is the mean number of phonons. In the case of no photons, N_{qp} is the thermal equilibrium value given in Eqn. 2.21. Under strong loading, when the light-induced density exceeds the thermal background, and the number of non-equilibrium quasiparticles scales as $N_{qp} \propto \sqrt{P/\Delta}$ [13].

2.2 Single charge tunnelling

In this section, we will look at single charge tunnelling phenomena in mesoscopic devices with tunnel junctions. When the Coulomb energy exceeds the thermal and quantum fluctuations in the device, we can observe and control single charges tunnelling through tunnel junctions. This not only occurs in normal metal and semiconductor systems in which the individual charge carriers are electrons and holes, but also in superconducting systems in which the charge carriers are Cooper pairs.

This section starts with charge tunneling onto a single normal-state island, introducing the concepts of the charging energy and Coulomb blockade. We will then describe tunnelling through double dot systems, including discussions on charging stability diagrams in different capacitance regimes.

2.2.1 Conditions for single charge tunnelling

A tunnel junction is two electrodes separated by an insulating gap. Similar to a parallel plate capacitor, each junction has an associated capacitance (C_J). Electrons are transferred through the insulating gap via quantum tunnelling, and so each junction has an associated resistance (R_J).

Consider a small metallic island connected a to metallic lead via a tunnel junction. In order to observe single charge tunneling, two conditions need to be met. The first

condition is that the electrostatic energy cost of adding a charge to this island far exceeds the available energy of thermal fluctuations, i.e.

$$E_C = \frac{e^2}{2C_J} \gg k_B T. \tag{2.25}$$

E_C is known as the charging energy of the island. The second condition is that the charging energy must also be greater than the energy uncertainty associated with the lifetime due to tunnelling $\hbar\tau_r = \hbar R_J C_J$. This leads to

$$R_J \gtrsim \frac{\hbar}{e^2} \equiv R_Q, \tag{2.26}$$

i.e. the resistance of the tunnel junction should be greater than the resistance quantum, $R_Q \simeq 25.8 \text{ k}\Omega$. This ensures that the electron wavefunction is localised on the island. When these two conditions are met, the number of electrons on the island remains fixed in time, and takes integer values n [106].

2.2.2 Single electron box
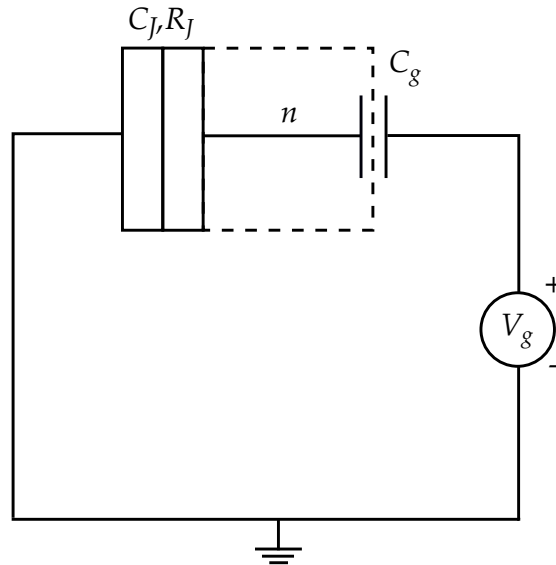
Figure 2.3: Schematic diagram of a single electron box (SEB) [106].

The most simple device in which single charge tunnelling has been measured is the single electron box (SEB, shown in Fig. 2.3). The SEB consists of a small metallic island connected via a tunnel junction with capacitance C_J and resistance R_J to an

electron reservoir and via a capacitance C_g to a gate voltage V_g, which tunes the electrochemical potential of the island [107]. We assume that the conditions for single charge tunnelling ($E_C \gg k_B T$ and $R_J \gtrsim R_Q$) apply. The charging energy in this system is defined as

$$E_C = \frac{e^2}{2C_\Sigma},$$ (2.27)

where $C_\Sigma = C_J + C_g$ is the sum of all capacitances in the system.
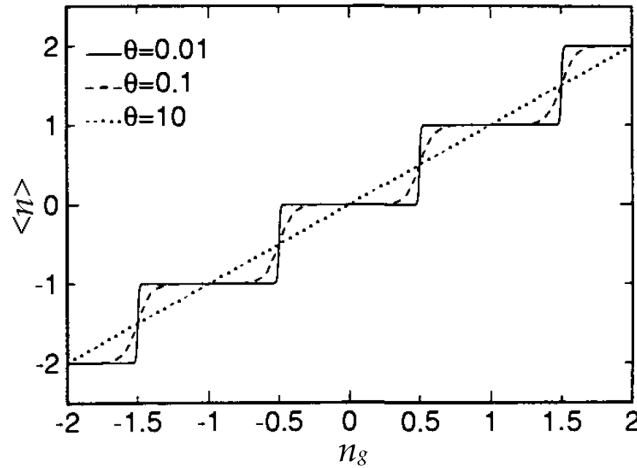
Figure 2.4: Coulomb staircase observed in the SEB, showing the average island charge, $\langle n \rangle$, versus gate charge for normalised thermal energies $\theta = k_B T C_\Sigma / e^2 = 0.01, 0.1$ and 10. Diagram from [107].

The average charge occupation of the island of the SEB, $\langle n \rangle$, is observed using an electrometer. As a function of the applied gate voltage, $\langle n \rangle$ varies as a periodic step function with a charge periodicity of e [107]. These steps are known as a Coulomb staircase and are shown in Fig. 2.4. Note how for temperatures in which $k_B T \gg E_C$ this single charging effect disappears.

The total energy of the single electron box is given by

$$E = \frac{Q^2}{2C_\Sigma} = \frac{(ne - C_g V_g)^2}{2C_\Sigma} + \text{terms independent of } n.$$ (2.28)

This energy is periodic in n (or charge) and is shown as a function of the normalised gate charge, $n_g = C_g V_g / e$, in Fig. 2.5. The energy in terms of n and n_g is

$$E = E_c(n - n_g)^2 + \text{terms independent of } n.$$ (2.29)

The energy of the system is minimised where $n = n_g$. The points at which neighbouring parabolas intersect, at half integer values of n_g, correspond to a
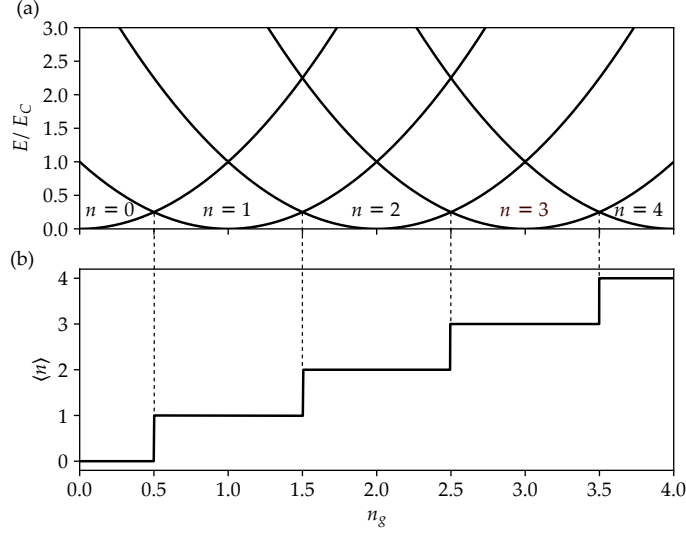
Figure 2.5: (a) The free energy and (b) corresponding Coulomb staircase of the single electron box as a function of gate charge. The degeneracy points in the energy bands correspond to electron tunnelling [108].

degeneracy between the n and $n + 1$ charge states. At these points, there is no energy cost for an electron to tunnel on ($n \rightarrow n + 1$) or off ($n + 1 \rightarrow n$) the island [106, 109].

2.2.3 Single electron transistor and Coulomb blockade

An extension to the SEB is a single island device with two tunnel junctions, such that a current may flow through it. This is the single electron transistor (SET), and a circuit diagram of it is shown in Fig. 2.6. The current is driven by a bias voltage $V_L - V_R$, and the electrochemical potential of the island is controlled by the gate voltage V_g. In the case of $V_{L,R} = 0$, the SET is equivalent to the SEB, and if the necessary conditions are met the same single charging effect can be observed with an electrometer.

Consider the case where we apply a small positive bias ($V_L > V_R$). The electrochemical potential of the left (right) lead is $\mu_{L(R)} = eV_{L(R)}$. The free energy of the island with n electrons is the same form as the SEB $E(n, n_g) = E_C(n - n_g)^2$. The electrochemical potential of the island $\mu_I(n, n_g)$ is defined as

$$\mu_I(n, n_g) = E(n, n_g) - E(n - 1, n_g) = E_C(2n - 1 - 2n_g), \qquad (2.30)$$

i.e. the energy needed to add the nth electron to the island.

26
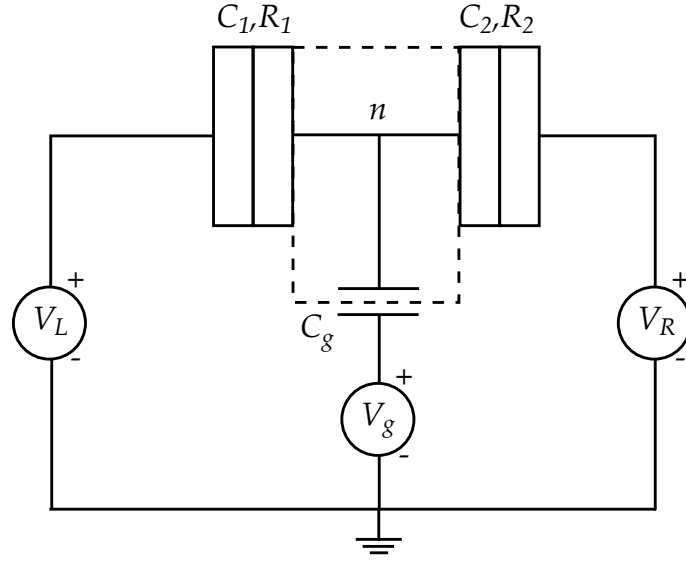
Figure 2.6: Schematic diagram of a single electron transistor (SET).

If $\mu_I(n + 1, n_g)$ is higher than μ_L, electrons are energetically forbidden to enter the island from the left electrode. In addition, if $\mu_I(n, n_g)$ is lower than μ_R, the electron on the island is energetically forbidden to escape through the right electrode. This is where we have *Coulomb blockade*, in which current cannot flow through the transistor due to the single charging effects of the island, and the number of electrons on the island is constant. (Fig. 2.7(a)).

Coulomb blockade is lifted if the electrochemical potential of the island falls within the bias window, i.e.

$$eV_L > \mu_I(n + 1) > eV_R, \tag{2.31}$$

so that electrons can tunnel sequentially from the left electrode, onto the island, and onto the right electrode (see Fig. 2.7(b)).

At a fixed voltage bias, the conduction through the junction can be switched "on" by tuning the the gate voltage to change the electrochemical potential of the island such that Eqn. 2.31 holds. This results in a series of conduction peaks with varying gate voltage. These peaks are known as *Coulomb oscillations* [111].

In the case of finite temperature ($E_C > k_B T > 0$), we need to consider the distribution of electrons over the energy states in the electrode, which is given by the Fermi-Dirac distribution

$$f(E, V) = \frac{1}{\exp \frac{E - e(V_L - V_R)}{k_B T} + 1}. \tag{2.32}$$

27
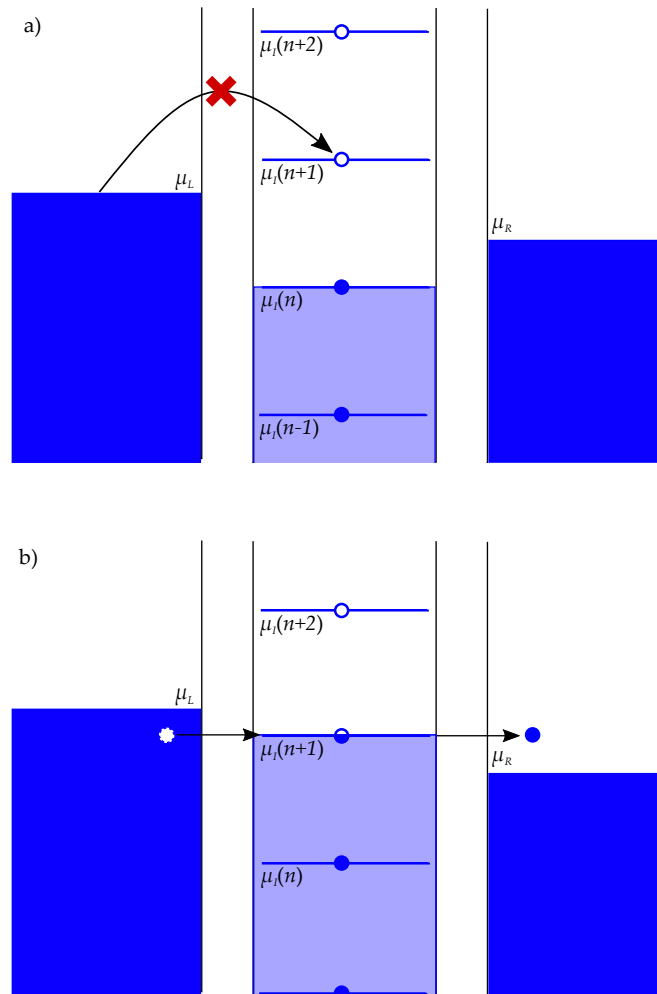
Figure 2.7: (a) Coulomb blockade in a single electron transistor (SET). Current cannot flow as the electrons cannot tunnel to a state with a higher electrochemical potential. (b) When the electrochemical potential of the island falls within the bias window, then electrons can always tunnel to a state with a lower electrochemical potential, and hence a current flows [110].

Therefore, even in the situation of Coulomb blockade, there may be a finite occupation of electrons that have energies above $E(n+1, n_g)$ which can tunnel onto the island. The result of this is that the width of the conductance peaks are proportional to the thermal energy $k_B T$ [111]. The conductance peaks have the form

$$G \propto \sum_n \cosh^{-2}\left(\frac{E_C\left(n + n_g + 1/2\right)}{2.5 k_B T}\right), \tag{2.33}$$

and are shown for varying temperature in Fig. 2.8.

28
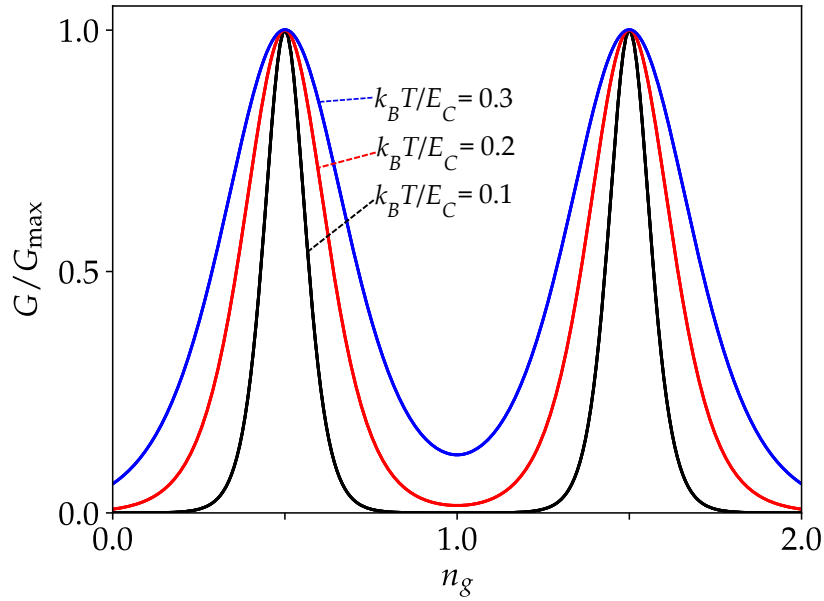
Figure 2.8: Calculated normalised conductance through a single electron transistor, using Eqn. 2.33, with $k_B T/E_C = 0.1$ (black), 0.2 (red) and 0.3 (blue). The conductance is maximal at the degeneracy points $n_g = n + 1/2$ [111].

2.2.3.1 Addition energy

The change in electrochemical potential if, at fixed n_g, n is changed by 1,

$$\Delta\mu = \mu_I(n + 1) - \mu_I(n) = e^2/C_\Sigma, \tag{2.34}$$

is called the *addition energy of the SET*.

2.2.4 Quantum dots

Coulomb blockade is a classical effect due to the electrostatic repulsion of the electrons on the island. If there is a confinement potential in all three spatial directions, there is another additional energy term due to the discrete energy spectrum, resembling that of an atom. The addition energy of the quantum dot is now

$$\Delta\mu = \mu_{QD}(n + 1) - \mu_{QD}(n) = \frac{e^2}{C_\Sigma} + E_{n+1} - E_n, \tag{2.35}$$

29
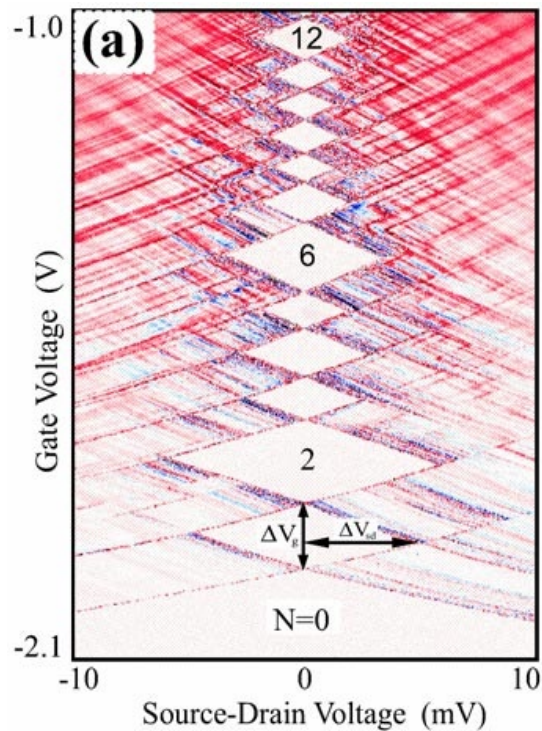
Figure 2.9: A measurement of differential conductance ($\partial I/\partial V$) of a InGaAs quantum dot, measured by Kouwenhoven et al. [112]. The white regions are *Coulomb diamonds* and correspond to $\partial I/\partial V \approx 0$.

where E_n is the highest occupied quantum state for an *n*-filled quantum dot[c]. The effect of this extra quantum term can be observed in the *Coulomb diamond* structure (a 2D intensity plot of the differential conductance vs the source and gate voltages). In Fig. 2.9 is an example of this with a InGaAs quantum dot SET from Kouwenhoven et al. [112]. Inside the diamonds the SET is Coulomb blockaded. The size of the diamonds are proportional to the addition energy. The anomalously large diamonds correspond to filled electron shells which, like in atoms, are particularly stable.

2.2.5 Double dots

Since quantum dots act like artificial atoms, one can think of coupling two quantum dots together to make an artificial molecule. These are known as double quantum dots. These structures are discussed at length in reviews by van der Wiel et al. [113] and Hanson et al. [114]. In this thesis, we shall only discuss the electrostatic energy

---

[c]In the semiconductor physics literature, the term e^2/C_Σ is usually called the charging energy, which is a factor of 2 larger than the charging energy defined for metallic or superconducting boxes.
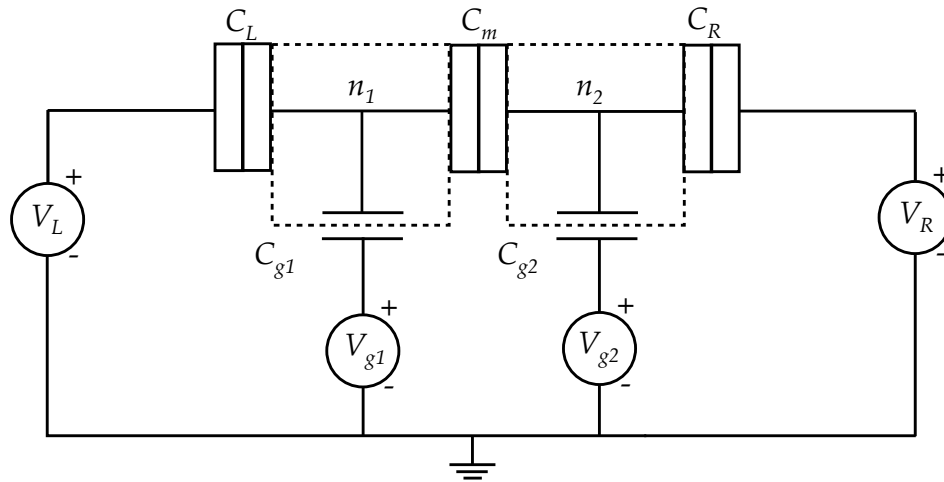
Figure 2.10: A circuit diagram of a double dot.

of the double dot system, the charge stability diagram and the addition energy terms. Furthermore we shall only consider the classical regime, i.e. no quantum confinement nor quantised energy levels, and therefore the physics also applies to metallic double-island structures. Throughout this section, I strictly follow the methods and definitions laid out in van der Wiel et al. [113].

2.2.5.1 Device overview

The double dot consists of two islands, or "dots", labelled as dot 1 and dot 2 (Fig. 2.10). The number of electrons on dot 1 (2) is $n_{1(2)}$. Dot 1 (2) is connected to the source (drain) lead via a tunnel junction with resistance R_L (R_R) and capacitance C_L (C_R). The dots are coupled to each other via a middle tunnel junction with resistance R_m and capacitance C_m. Dot 1 (2) is also capacitively coupled to a gate voltage $V_{g1(2)}$ through a capacitance $C_{g1(2)}$. In practice, there may be a non-zero cross-capacitance between gate 1 (2) and dot 2 (1), $C_{g12(21)}$.

2.2.5.2 Electrostatic energy of double dots

To derive the electrostatic energy of the double dot, U, the double dot is modelled as a network of capacitors and voltage nodes. The charge on node j, Q_j is the sum of the charges of all of the capacitors connected to node j, i.e.

$$Q_j = \sum_k q_{jk} = \sum_k c_{jk}(V_j - V_k), \qquad (2.36)$$

31

where c_{jk} is the capacitance between nodes j and k and V_j is the electrostatic potential of node j. The charges on the nodes are linear functions of the potentials of the nodes, so this can be conveniently expressed in matrix form,

$$\boldsymbol{Q} = C\boldsymbol{V}, \tag{2.37}$$

where C is the capacitance matrix. A diagonal element of the capacitance matrix C_{jj} is the total capacitance of node j,

$$C_{jj} = \sum_{k \neq j} c_{jk}. \tag{2.38}$$

An off-diagonal component of the capacitance matrix is minus the capacitance between node j and node k, $C_{jk} = C_{kj} = -c_{jk}$. The electrostatic energy in this system is the sum of electrostatic energies of all of the capacitors and is

$$U = \frac{1}{2}\boldsymbol{V} \cdot \boldsymbol{Q} = \frac{1}{2}\boldsymbol{V} \cdot C\boldsymbol{V}. \tag{2.39}$$

The electrostatic energy term for the superconducting double dot is derived in this way for the remainder of this thesis.

#### 2.2.5.3 Charge stability diagrams
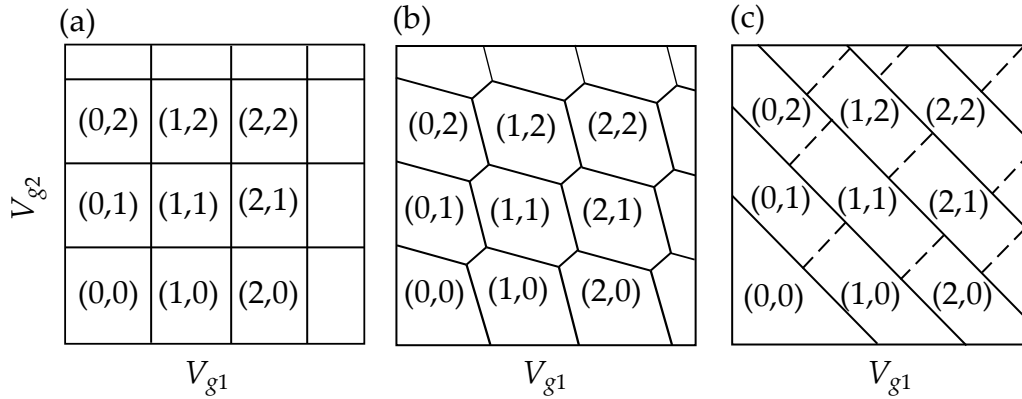
Figure 2.11: A schematic charge stability diagram for a double quantum dot with (a) weak coupling $C_m = 0$, (b) intermediate coupling and (c) strong coupling $C_m/C_{1(2)} \rightarrow 1$ [113].

At zero source-drain bias, the number of individual charges on each dot can be changed by adjusting the applied gate voltage on each gate. This is the same principle

as the Coulomb staircase for the SEB, but as there are now two gate voltages, it is possible to construct a two dimensional plot of the charge occupation number for each dot as a function of both gate voltages. This is known as the *charge stability diagram.* This diagram shows which charge state (n_1, n_2) has the lowest electrostatic energy $U \equiv U(n_1, n_2)$, and therefore the occupied state at equilibrium.

A schematic of a charge stability diagram for a double quantum dot with $C_m > 0$ is shown in Fig. 2.11. The regions of stable charge are the hexagons within the solid lines. A current can only flow through the double dot system at the points at which three honeycombs meet. These points are known as the *triple points.*

2.2.5.4   Addition energies of double dots

We consider the linear transport regime i.e. where the source-drain bias $V_L - V_R \approx 0$ and a classical system i.e. there are no discrete quantum states. In a similar case to the SET, an electron can tunnel through the system if the electrochemical potentials of the dots, source and drain, line up so that the electron can flow from a high to a low electrochemical potential. The electrochemical potential of the left dot (dot 1) is defined as the energy needed to transfer the n_1^{th} electron onto dot 1, while having n_2 on the right dot (dot 2), i.e.

$$\mu_1(n_1, n_2) \equiv U(n_1, n_2) - U(n_1 - 1, n_2).\tag{2.40}$$

The change in μ_1 when n_1 is changed by 1 at fixed gate voltages is

$$\mu_1(n_1 + 1, n_2) - \mu_1(n_1, n_2) \equiv E_{C1}.\tag{2.41}$$

This is known as the addition energy of dot 1. By symmetry, equivalent equations can be found for μ_2 and E_{C2}. In addition, there is a coupling energy

$$E_{Cm} \equiv \mu_1(n_1, n_2 + 1) - \mu_1(n_1, n_2) = \mu_2(n_1 + 1, n_2) - \mu_2(n_1, n_2),\tag{2.42}$$

which is the change in energy of one dot when an electron is added to the other dot. These energies are derived from the electrostatic energy of the double dot system by van der Wiel et al. [113]. In terms of the device capacitances, these are

$$E_{C1} = \frac{e^2}{C_1} \left(\frac{1}{1 - \frac{C_m^2}{C_1 C_2}} \right),\tag{2.43}$$

$$E_{C2} = \frac{e^2}{C_2} \left(\frac{1}{1 - \frac{C_m^2}{C_1 C_2}} \right), \tag{2.44}$$

$$E_{Cm} = \frac{e^2}{C_m} \left(\frac{1}{\frac{C_1 C_2}{C_m^2} - 1} \right), \tag{2.45}$$

where $C_{1(2)}$ is the sum of the capacitances attached to dot 1(2), including C_m and cross-capacitance terms:

$$\begin{aligned} C_1 &= C_L + C_{g1} + C_m + C_{g12}, \\ C_2 &= C_R + C_{g2} + C_m + C_{g21}. \end{aligned} \tag{2.46}$$

Van der Wiel et al. refer to E_{C1} and E_{C2} as the *charging energies* of dot 1 and dot 2, respectively [113]. We use these energy expressions for the superconducting double dot, and do so for the remainder of this thesis [d].

2.2.5.5 Determining the double dot capacitances
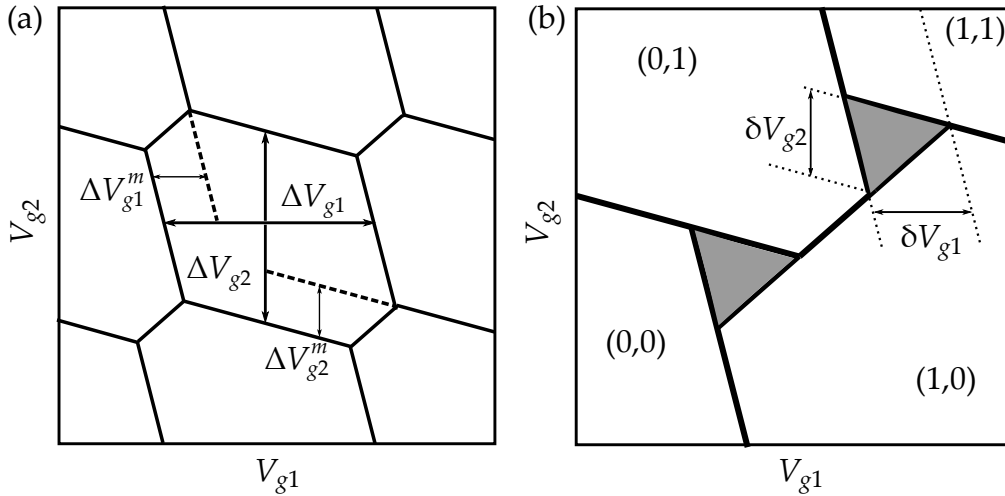
Figure 2.12: (a) Schematic stability diagram showing the Coulomb peak spacing given in Eqns. 2.47 and 2.48. These spacings can be determined experimentally by connecting the triple points. (b) Schematic diagram of region near a charge boundary of the charge stability diagram, at finite bias voltage. The solid lines separate the charge domains. Regions where current flows are given by the gray triangles. The dimensions of the triangles are given in Eqn. 2.49.

---

[d]In other publications, charging energies E_{C1} and E_{C2} may be defined differently for similar structures, such as coupled Cooper pair boxes [115]

The capacitances of the double dot system are found from the charge stability diagram, as shown in Fig. 2.12(a). Derived in van der Wiel et al. [113], the dimensions of the honeycomb cell are

$$\Delta V_{g1(2)} = \frac{|e|}{C_{g1(2)}}, \tag{2.47}$$

and

$$\Delta V_{g1(2)}^m = \frac{|e| \, C_m}{C_{g1(2)}C_{2(1)}} = \Delta V_{g1(2)} \frac{C_m}{C_{2(1)}}. \tag{2.48}$$

This gives the gate capacitances, C_{g1} and C_{g2}. To find C_1, C_2 and C_m, it is necessary to apply a voltage bias across the double dot system. The conductance regions at finite bias change from triple points to triangular shaped regions known as bias triangles, shown in Fig. 2.12(b). The voltage bias dimensions of the bias triangles by the following equations:

$$|V_{\text{bias}}| = \frac{C_{g1(2)}}{C_{1(2)}} \delta V_{g1(2)} \tag{2.49}$$

Combining Eqs. 2.47, 2.48 and 2.49, we can calculate the values of the total capacitances $C_{1,2}$ and mutual capacitance C_m, and hence we can also calculate the double dot energies E_{C1}, E_{C2} and E_{Cm}.

2.2.6 Double quantum dots

We now briefly consider the double dot system in the quantum regime, i.e. with quantised energy levels. As discussed in section 2.2.4, a quantum dot is considered to be an artificial atom due to its quantized energy levels. When electrons can coherently tunnel from one quantum dot to another, the wavefunctions become delocalised and extend over the two quantum dots. Such a double quantum dot system is therefore considered to be an artificial molecule, where the highest occupied states of each quantum dot (E_1, E_2) hybridise to form two new eigenstates - a bonding state, with energy E_B, and an anti-bonding state, with energy E_A, which are

$$E_{B,A} = E_M \mp \sqrt{\frac{1}{4}(\Delta E)^2 + t_c^2}, \tag{2.50}$$

where $E_M = \frac{1}{2}(E_1 + E_2)$ and $\Delta E = E_1 - E_2$. The tunnel coupling is characterised by an energy t_c. In Fig. 2.13, we show the eigenenergies of a double quantum dot system as a function of ΔE. For vanishing coupling $t_c \approx 0$, the levels cross at the origin. For non-zero coupling, an anticrossing occurs and there is a minimum energy separation of $2t_c$ [113].
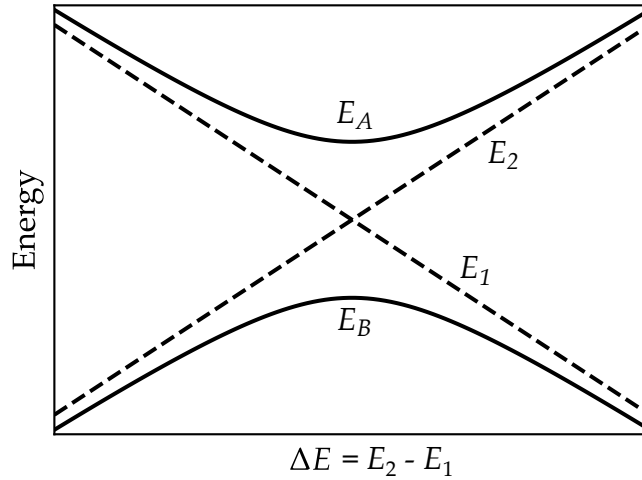
Figure 2.13: Schematic diagram of the energies of a double quantum dot system. Unperturbed energy levels E_1 and E_2 (dashed lines) and energy levels belonging to the bonding state, E_B, and the antibonding state, E_A (solid lines) versus the energy difference $\Delta E = E_1 - E_2$ [113].

The eigenenergies of the double quantum dot are essentially the same form as the Cooper pair box. In this case, the tunnel coupling energy is the Josephson energy. This is derived in full and discussed further in section 2.3.3.

Semiconductor double quantum dots have shown to be suitable candidates as qubits, where coherent control of the charge [116] and spin [96] occupation has been demonstrated.

2.3 Superconducting charge devices

Single charge devices in which the island or electrodes are superconducting have additional properties to their metallic counterparts. In Section 2.3.1, we start with a superconducting island with a normal lead and study the effects of Cooper pairing and quasiparticles. In section 2.3.2, we change the lead to a superconductor. The tunnel junction between the two superconductors is known as a Josephson junction, which acts as a non-linear inductor which stores a minimum energy. This Josephson energy hybridises the charge states at the degeneracy points, much like the double quantum dot. This leads to the Cooper pair box qubit, discussed in section 2.3.3.

(a)

Normal junction

Normal-insulator

-superconductor (NIS) junction

Superconducting

(Josephson) junction

(b)

C,R

C_g

n

V_g

NS box

(c)

C,R,L_J

C_g

n

$-Q_J$ $+Q_J$ $-Q_g$ $+Q_g$

V_g

Cooper pair box

(d)

C_1,R_1,L_{J1} C_2,R_2,L_{J2}

n

V_L C_g V_R

V_g

Superconducting SET
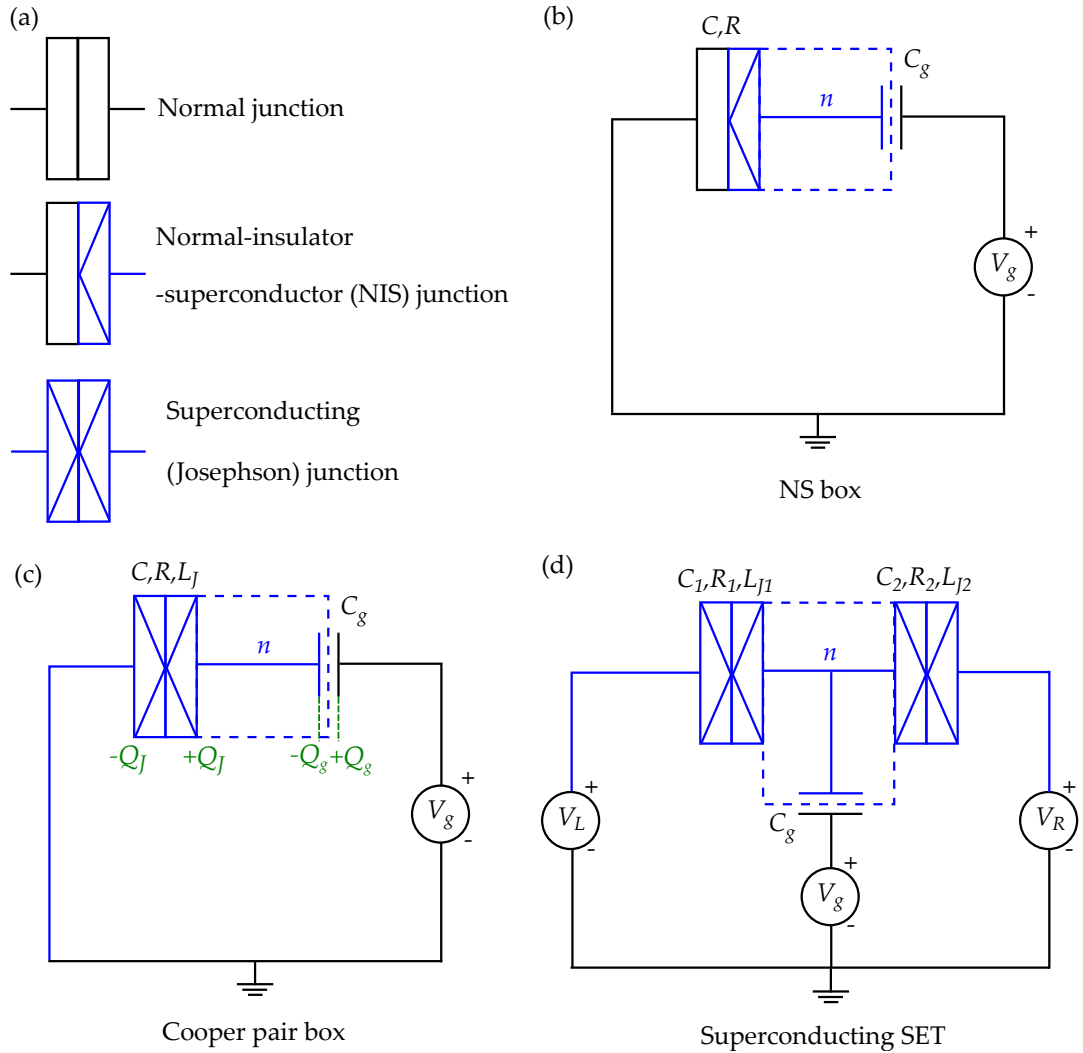
Figure 2.14: (a) The symbols used in this thesis for normal, normal-superconducting and superconducting tunnel junctions. Superconducting elements are coloured in blue. (b) A circuit diagram of a normal-superconducting (NS) box. (c) A circuit diagram of a Cooper pair box. (d) A circuit diagram of a superconducting SET (SSET). Superconducting components are coloured in blue.

2.3.1 Parity effect

In an island of the superconducting device, the conduction electrons[e] pair up into Cooper pairs. But if there is an odd number of conduction electrons, one unpaired quasiparticle will remain and will occupy the lowest quasiparticle state with energy

---

[e]Specifically, electrons which are within $\pm\hbar\omega_D$ of the Fermi energy, where ω_D is the Debye phonon frequency.

Δ. Therefore, the free energy of the system depends on whether there is an even or odd number of elementary charges (*e*) on the island. This is known as the *parity effect*, and was first discovered in measurements of current through a superconducting SET (Fig. 2.14(d)) by Tuominen et al. [64] and charge on a superconducting island by Lafarge et al. [108, 66].

Consider a superconducting island connected to a normal lead (known as an NS box, Fig. 2.14(b)). To calculate the this additional energy for states in which *n* is odd, we can write down the internal energy of the system as

$$U = E_c(n - n_g)^2 + (n \bmod 2)\Delta + \text{terms independent of } n. \tag{2.51}$$

However, the unpaired quasiparticle has a momentum degree of freedom, and so the states available to the quasiparticles form a continuous band. We must therefore consider the *free energy* of the system, $F = U - TS$, which takes into account the entropy of the quasiparticle occupying the band. The entropy of the quasiparticle is given by the Boltzmann entropy $\Delta S = k_B \ln W$, where $W = G!/N!(G - N)!$ is the number of ways to store N quasiparticles in G microstates. In the single quasiparticle limit, this reduces to $S = k_B \ln G$.

Recalling that in the low temperature limit $\Delta/k_B T \gg 1$, the number of microstates is N_{eff}, as given in Eqn. 2.21. We then get the free energy of the system as

$$F = E_C(n - n_g)^2 + (n \bmod 2)\tilde{\Delta} + \text{terms independent of } n, \tag{2.52}$$

where

$$\tilde{\Delta} = \Delta - k_B T \ln N_{eff} \tag{2.53}$$

is the free energy difference between the even and odd parities [108]. This expression for free energy can also be derived using the canonical partition function, as is done by Tuominen et al. [64] and Lafarge et al. [66].

The average number of electrons on the island $\langle n \rangle$ depends on the relative magnitudes of the charging energy, E_C, and $\tilde{\Delta}$. $\tilde{\Delta}$ opposes the creation of quasiparticles and E_C tries to make the charge on the island match the charge on the gate n_g. The three different charging regimes are discussed below and are illustrated in Fig. 2.15.

Case 1: $E_C < \tilde{\Delta}$

The minima of the odd *n* parabola are above the point at which the even parabola cross. $\langle n \rangle$ increases in steps of 2 every gate period of 2*e*. In this regime, transfer of charge
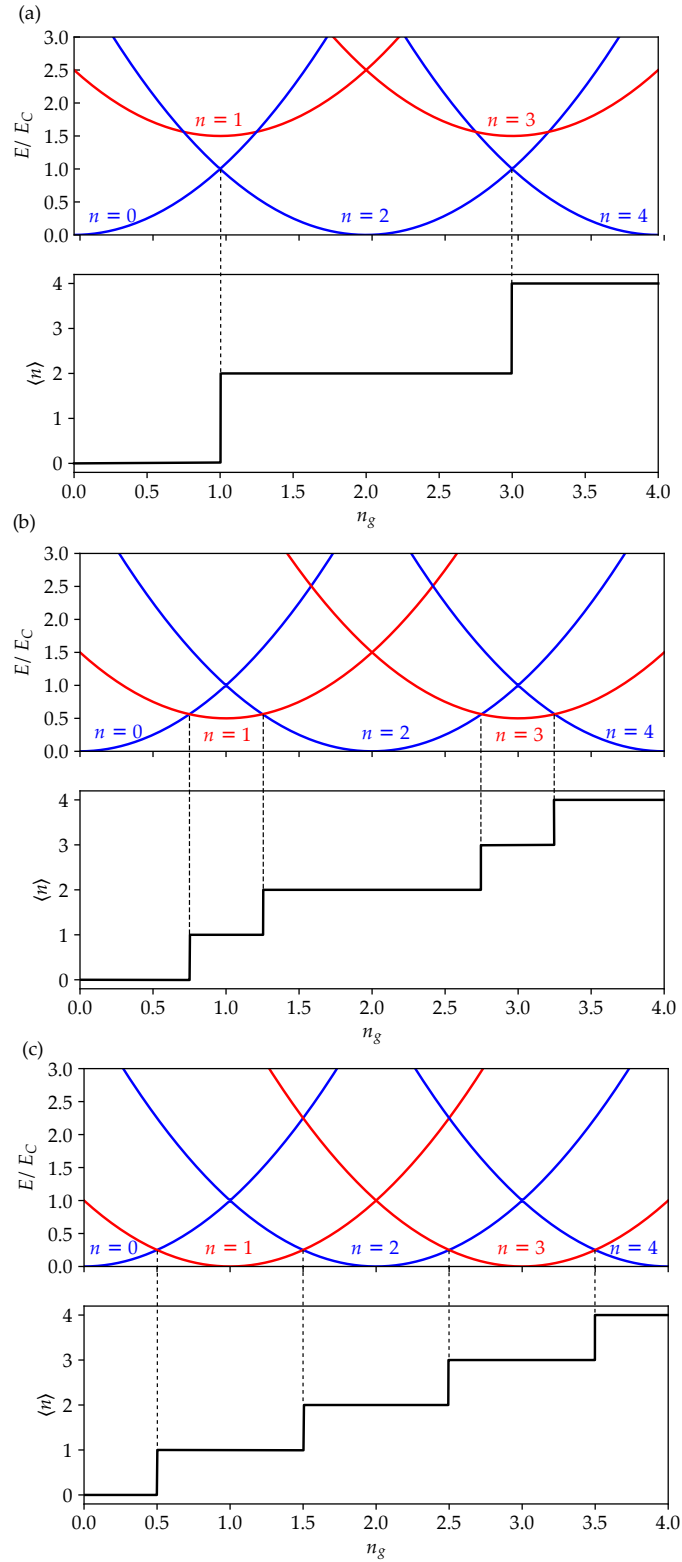
Figure 2.15: Free energy, E, and average charge (in units of e), $\langle n \rangle$, of the NS box with respect to n_g when (a) $E_C < \tilde{\Delta}$, (b) $E_C > \tilde{\Delta} > 0$ and (c) $\tilde{\Delta} = 0$ [108].

happens via the tunnelling of Cooper pairs.

Case 2: $E_C > \tilde{\Delta} > 0$

The minima of the odd n parabola are now below the Cooper pair tunnelling points. Single electron tunneling is now observed, but the system remains $2e$-periodic. $\langle n \rangle$ increases in a sequence of short (odd) and long (even) steps. The length ratio of the short and long steps equals $\tilde{\Delta}/E_C$.

Case 3: $\tilde{\Delta} = 0$

The island is now in the normal state with e periodicity; the device is equivalent to the SEB.

2.3.2 Josephson effect

In 1962, Brian Josepshon predicted that when two superconducting electrodes are separated by a thin insulating barrier (i.e. an SIS junction), a supercurrent should flow when no voltage is applied across the junction [11, 25]. This is known as the *dc-Josephson effect* and the supercurrent is

$$I_J = I_c \sin \phi, \tag{2.54}$$

where ϕ is the phase difference of the wavefunction across the junction. The critical current, I_c, is the maximum supercurrent which can flow across the junction whilst preserving the superconducting state. The phase difference across the junction varies in time with an applied voltage across the junction.

$$\frac{d\phi}{dt} = \frac{2eV}{\hbar}. \tag{2.55}$$

Solving this for constant voltage yields

$$\phi = \phi(0) + \frac{2eVt}{\hbar} \tag{2.56}$$

and

$$I_J = I_c \sin(\phi(0) + 2eVt/\hbar). \tag{2.57}$$

40

This is the ac-Josephson effect; a non-zero voltage bias produces an alternating current through the Josephson junction with amplitude I_c and frequency $\omega = 2eV/\hbar$. The energy change of a Cooper pair across the junction is equal to $\hbar\omega$.

The Josephson junction acts as an inductor, and the free energy stored in the junction is calculated by integrating the work done by a current source to change the phase

$$
\begin{aligned}
E = \int I_J V dt &= \int I_J \frac{\hbar}{2e} d\phi, \\
&= -E_J \cos\phi + C, \qquad \text{where } E_J = \frac{\hbar I_c}{2e}.
\end{aligned}
\tag{2.58}
$$

E_J is known as the Josephson energy, and is the minimum energy stored in the junction when the phase difference across the junction is zero. This shows that the critical current is a measure of how strongly the phases of the two superconducting electrodes are coupled. At low temperatures ($k_B T \ll \Delta$), the Ambegokar-Baratoff relation gives the critical current as

$$
I_c = \left(\frac{\pi\Delta}{2eR_n}\right) \tanh\left(\frac{\Delta}{2k_B T}\right) \approx \left(\frac{\pi\Delta}{2eR_n}\right),
\tag{2.59}
$$

where R_n is the resistance of the junction in the normal state. This gives

$$
E_J = \frac{\hbar I_c}{2e} = \frac{h\Delta}{8e^2 R_n}.
\tag{2.60}
$$

2.3.2.1 Josephson effect in the presence of a magnetic field

It is possible to control the Josephson coupling energy by using the principle of quantum interference of the BCS wavefunction. The phase difference across a superconducting junction can be controlled by applying an external flux.

In this thesis, we will consider a superconducting loop containing two Josephson junctions (a sketch of which is shown in Fig. 2.16). This system in known as a DC-SQUID (Superconducting QUantum Interference Device) [f].

A gauge-invariant way to treat the phase difference across a Josephson junction is to include the effect of the vector potential, A. The magnetic flux inside the ring, Φ, changes the vector potential along the path of the loop, giving rise to a phase gradient. The total gauge-invariant phase difference accumulated within one cycle around the SQUID loop is

$$
\phi = -\varphi_1 + \frac{2\pi}{\Phi_0}\int_1^2 A \cdot dl + \varphi_2 + \frac{2\pi}{\Phi_0}\int_2^1 A \cdot dl,
\tag{2.61}
$$

[f]This system is used in the galvanically isolated superconducting double dot in Chapter 7.
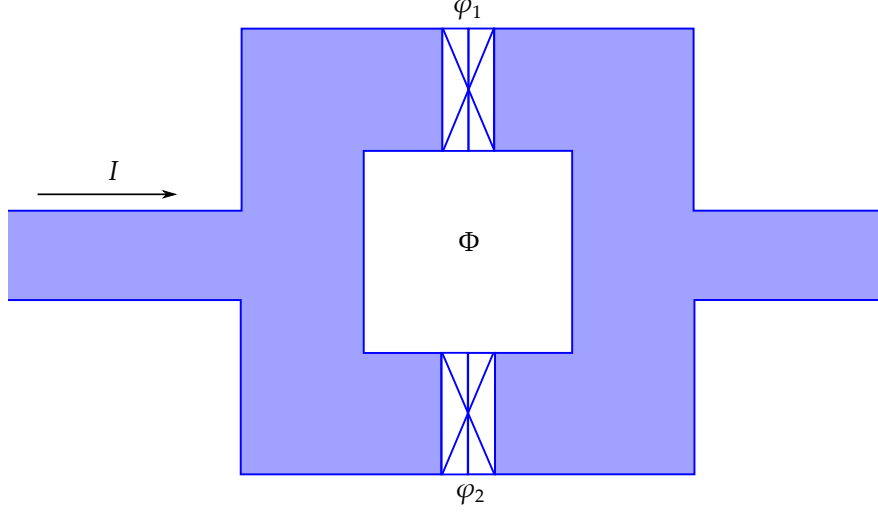
Figure 2.16: Sketch of a DC-SQUID loop, with two Josephson junctions with phase difference $\varphi_{1(2)}$ across the top (bottom) junction and magnetic flux Φ through the loop.

where $\varphi_{1(2)}$ is the phase difference across junction 1 (2), and $\Phi_0 = h/2e$ is the flux quantum. The first integral in this expression is taken around the right side of the loop, and the second around the left. Including the small effect of the vector potential on the junctions, we obtain

$$\phi_{\text{tot}} = \varphi_2 - \varphi_1 + \frac{2\pi}{\Phi_0} \oint \boldsymbol{A} \cdot d\boldsymbol{l} = \varphi_2 - \varphi_1 + \frac{2\pi\Phi}{\Phi_0}. \tag{2.62}$$

The phase at a given position should be single valued, i.e. the total phase difference around the loop should be $\phi_{\text{tot}} = 2n\pi$, where n is an integer. This means that

$$\phi_2 - \phi_1 = \frac{2\pi\Phi}{\Phi_0} \, (\text{mod} 2\pi). \tag{2.63}$$

The total current though the loop is

$$I = I_{c1} \sin(\varphi_1) + I_{c2} \sin\left(\varphi_1 - \frac{2\pi\Phi}{\Phi_0}\right), \tag{2.64}$$

where $I_{c1(c2)}$ is the critical current of junction 1 (2). In the symmetric case $I_{c1} = I_{c2} \equiv I_c$, for a given flux Φ, the maximum external current that can flow as a supercurrent though this system is

$$I = 2I_c \left|\cos\left(\frac{\pi\Phi}{\Phi_0}\right)\right|. \tag{2.65}$$

The critical current of the SQUID loop can be modulated with a flux [110]. From the Ambegokar-Baratoff relation in Eqn. 2.60, the Josephson energy is given by

$$E_J = E_{J,\text{max}} \left|\cos(\pi\Phi/\Phi_0)\right|. \tag{2.66}$$

At half-flux quanta intervals, the Cooper pair wavefunctions destructively interfere and the Josephson energy, E_J, is zero.

2.3.3 Superconducting qubits

One of the most simple superconducting devices consists of a superconducting island connected to a superconducting lead via a Josephson junction (Fig. 2.14(c)). There are two degrees of freedom, the excess number of Cooper pairs on the island $2n$, and the phase difference across the junction ϕ. These are quantum complementary variables, which obey the uncertainty relation $\Delta n \Delta \phi \geq 1$. This means that they cannot be independently be measured to an arbitary precision; only one of n or ϕ can be described as a "good quantum number" - a quantity whose expectation value is constant over time - and can be used to label the quantum states [117]. This leads to the superconducting qubit (as described in Chapter 1), where there is a two level system, either in n or ϕ.

Assuming for now that all electrons are paired up (i.e. no quasiparticles) the Hamiltonian of the system is the sum of the electrostatic and Josephson Hamiltonians, and can be written as

$$H = H_{el} + H_J = E_C(n - n_g)^2 - E_J \cos \phi, \tag{2.67}$$

where $n_g = C_g V_g / e$ is the gate charge normalised by the charge of an electron. In the regime $E_J \gg E_C$, the phase difference of the junction is a good quantum number and is used as the qubit states, either by manipulating the magnetic flux through a SQUID loop (flux qubit) or the driving current of a superconducting tunnel junction (phase qubit). Flux and phase qubits are not discussed in this thesis, but the reader is directed to Refs. [9], [39] and [43] for more information on these structures.

In the following sections, we remain in the regime $E_C \gtrsim E_J$ and derive the Hamiltonian of a superconducting charge qubit. We also remain in the single charging regime i.e. $E_C \gg k_B T$ and the junction resistance $R_j > R_Q$.

2.3.3.1 Charge qubit: Cooper pair box

When $E_C > \tilde{\Delta}$ single quasiparticles dominate and the ground state energy is the same as the NS-box in the same regime (Fig. 2.15(c)).

In the regime $\Delta > E_C > E_J > k_B T$, charge fluctuations in the island are suppressed. The excess number of (paired) electrons, n, is a good quantum number in which we

can label the charge states. In this representation, the variable n is an operator on the qubit basis. This is written as

$$\hat{n}\,|n\rangle = n\,|n\rangle,\tag{2.68}$$

where n is strictly an even number (as the odd number states are reserved for the excited quasiparticle states). The Josephson coupling term $\cos\phi = (e^{i\phi} + e^{-i\phi})/2$ is the sum of two terms in which raise or lower the number of Cooper pairs by one. In terms of the n-basis, this is

$$e^{\pm i\hat{\phi}}\,|n\rangle = |n\pm 2\rangle.\tag{2.69}$$

Thus, in the n-basis, the Hamiltonian of the system is

$$
\begin{aligned}
H &= \sum_{n\text{ even, }m\text{ even}} |n\rangle\,\langle n|\,H\,|m\rangle\,\langle m| \\
&= \sum_{n\text{ even}} E_C(n - n_g)^2\,|n\rangle\,\langle n| - \frac{1}{2}E_J\,(|n\rangle\,\langle n+2| + |n+2\rangle\,\langle n|).
\end{aligned}\tag{2.70}
$$

The resulting energy bandstructure looks like the NS-box (when $\tilde{\Delta} > E_C$) but the Josephson coupling term lifts the degeneracy at each intersection of the Coulomb parabola. This is due to the coherent tunneling of a single Cooper pair.

The energy of the system is periodic with respect to the addition of an extra Cooper pair. We can therefore keep the gate charge between $0 < n_g < 2$, and so the Hamiltonian is reduced to a two-dimensional Hilbert space, spanning only the two crossing charge states, $|0\rangle$ and $|2\rangle$.

In this basis, the Hamiltonian is a 2×2 matrix, and is

$$H = \frac{1}{2}\begin{bmatrix} E_0 - 4E_C(1 - n_g) & -E_J \\ -E_J & E_0 + 4E_C(1 - n_g) \end{bmatrix},\tag{2.71}$$

where the trace of this matrix $E_0 = E_C(2n_g^2 - 4n_g + 4)$ is an offset energy independent of the energy state. We choose $E_0 = 0$, and the resulting Hamiltonian has the same form as a spin-half particle in a magnetic field $\boldsymbol{B} = (E_J, 0, 4E_C(1 - n_g))$. The energy eigenvalues are

$$E_{G,E} = \pm\frac{1}{2}\sqrt{16E_C^2(1 - n_g)^2 + E_J^2} = \pm\frac{1}{2}\Delta E,\tag{2.72}$$

where we define $\Delta E \equiv \Delta E(n_g)$ as the difference with energy between the excited (E) and ground (G) states. The eigenstates are given by

$$|G\rangle = \begin{pmatrix} \sin(\eta/2) \\ \cos(\eta/2) \end{pmatrix}, \qquad |E\rangle = \begin{pmatrix} \cos(\eta/2) \\ -\sin(\eta/2) \end{pmatrix},\tag{2.73}$$
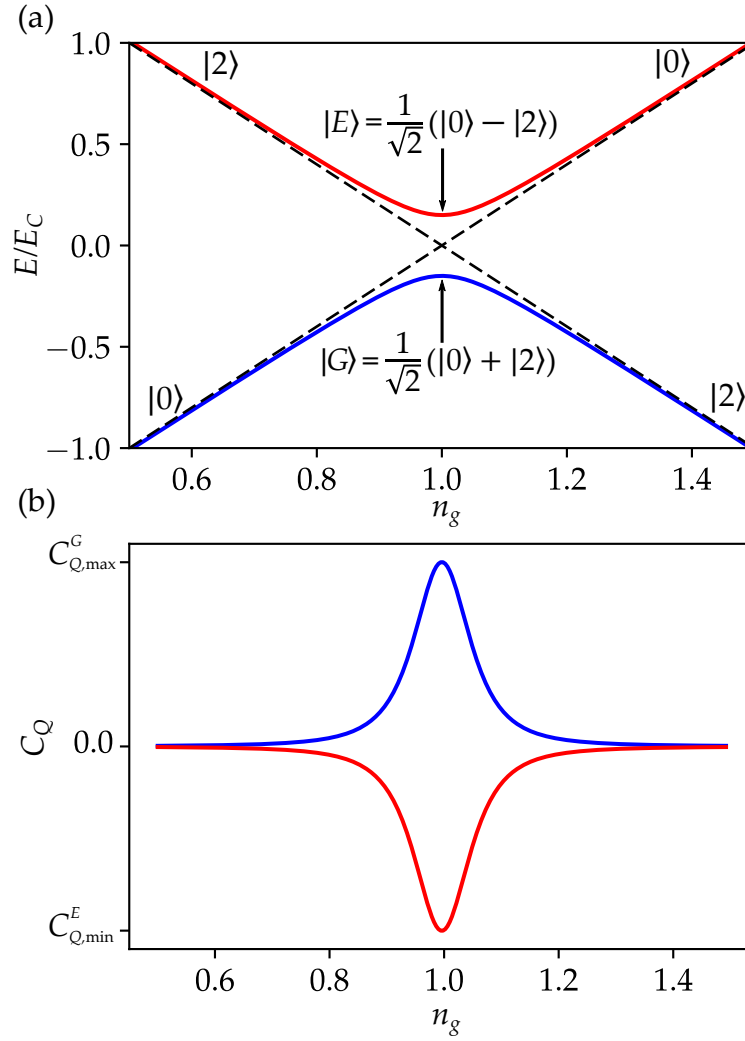
Figure 2.17: (a) Energy diagram of a Cooper-pair-box with respect to normalised gate voltage, $n_g = C_g V_g / e$, where $E_J = 0.3 E_C$, as given in Eqn. 2.72. Charge states are labelled. Diagram adapted from [118]. (b) Quantum capacitance of the ground (blue) and excited (red) states of the Cooper pair box.

where

$$\eta = \arccos\left(\frac{4E_C(1 - n_g)}{\Delta E}\right),\tag{2.74}$$

is the mixing angle, which varies with the normalised gate-induced charge on the island $n_g = C_g V_g / e$. In the limit $n_g \ll 1$, the ground state goes to $|0\rangle$ and the excited state goes to $|2\rangle$ and vice versa for $n_g \gg 1$. At the degeneracy point $n_g = 1$ the states are a superposition of charge states: $|G\rangle = 1/\sqrt{2}(|0\rangle + |2\rangle)$ and $|E\rangle = 1/\sqrt{2}(|0\rangle - |2\rangle)$.

This system is known as a (single) Cooper pair box (CPB), and has been

demonstrated as a a qubit which can be coherently controlled [50] and readout [119, 120]. Quantum entanglement in coupled Cooper pair boxes has also been demonstrated [115]. Fig. 2.17(a) shows the energy diagram of the CPB near $n_g = 1$.

2.4 State Readout: Quantum Capacitance

The charge state of the Cooper pair box may be measured by a suitable electrometer, such as a single electron transistor [121, 122] or quantum point contact [123, 124]. The electrometer is tuned such that its conductance changes when the nearby CPB changes charge state by one Cooper pair. The CPB has the longest decoherence times when operated at the degeneracy point $n_g = 1$ (often called the "sweet spot") as this is where the energy difference between the ground and excited state is, to first order, independent of gate charge, making it less vulnerable to charge noise. [53]. However, at this "sweet spot", the average charge is the same for both ground and excited states, so one must move away from this spot for readout schemes based upon charge measurement [50, 125].

Whilst the charge state of the two states are equal, the curvature of the energy bands are equal but have opposite sign. This difference in curvature is detected by measuring a quantity known as *quantum capacitance* - a contribution to the device capacitance dependent on the quantum state. There are different expressions for quantum capacitance documented [42, 120, 126]. In this thesis, we will use the form quoted in Duty et al. [127].

Quantum Capacitance (Duty et al.)

The contribution to the capacitance from the eigenstate of a qubit, k, is proportional to the second derivative of the eigenenergy with respect to the (normalised) gate charge (or gate voltage), i.e.

$$C_Q^k = -\frac{C_g^2}{e^2}\frac{\partial^2 E_k}{\partial n_g^2} = -\frac{\partial^2 E_k}{\partial V_g^2}. \tag{2.75}$$

Measuring quantum capacitance does not require an additional electrometer, thus simplifying device fabrication. The capacitance is usually connected to a resonant circuit and probed with an oscillating voltage via the gate or lead $V_g = V_{gdc} +$

$\delta V_g \sin(\omega_r t)$. This additional state-dependent capacitance loads the resonator leading to a dispersive shift in resonant frequency [128]. This is discussed in the Chapter 3, section 3.3.

To understand the origin of this state dependent capacitance, I derive the expression for quantum capacitance using a method inspired by Duty et al. [127]. For a Cooper pair box. I assume that the probing frequency, ω_r is faster than the rate of relaxation, so that there is no thermal repopulation on the timescale of the resonator [128].

2.4.1 Derivation

A circuit diagram of the Cooper pair box is shown in Fig. 2.14(c). The Josephson junction acts as a parallel plate capacitor with Q_J accumulating on the plates. The gate is similarly treated with Q_g accumulating on the plates. From electrostatics, these are calculated to be

$$Q_J = C_J V_I,$$
$$Q_g = C_g(V_g - V_I),$$
(2.76)

where V_I is the potential of the island. The net charge on the island is

$$Q_J - Q_g = -ne,$$
(2.77)

where n is the excess number of electrons on the island. This gives

$$V_I = \frac{C_g V_g - ne}{C_\Sigma},$$
(2.78)

where $C_\Sigma = C_J + C_g$.

We now define an effective capacitance as the first derivative of injected charge with respect to voltage

$$C_{\text{eff}} = \frac{\partial \langle Q_g \rangle}{\partial V_g},$$
(2.79)

where the angled brackets denote the expectation value. From Eqns. 2.76, 2.77 and 2.78, $\langle Q_g \rangle$ is

$$\langle Q_g \rangle = \frac{C_g C_J}{C_\Sigma} V_g + \frac{C_g e}{C_\Sigma} \langle n \rangle.$$
(2.80)

Using $dn_g = (C_g/e)dV_g$, we expand Eqn. 2.79 to

$$C_{\text{eff}} = \frac{C_g C_J}{C_\Sigma} + \frac{C_g^2}{C_\Sigma} \frac{\partial \langle n \rangle}{\partial n_g}.$$
(2.81)

47

The first term $C_{\text{geom}} = C_g C_J / C_\Sigma$ is the geometric capacitance. The second term is the quantum capacitance, C_Q^k, depends on the occupation of the ground and excited states. Recalling the eigenstates in Eqn. 2.73, the average occupations for the states $|G\rangle$ and $|E\rangle$ are

$$\langle n \rangle_G = \langle \psi_G | n | \psi_G \rangle = 2 \sin^2 \eta/2 = 1 - \cos \eta$$
$$\langle n \rangle_E = \langle \psi_E | n | \psi_E \rangle = 2 \cos^2 \eta/2 = 1 + \cos \eta \tag{2.82}$$

From $\cos \eta = \frac{4E_C(1-n_g)}{\Delta E}$, we get

$$\langle n \rangle_{G,E} = \left(1 \mp \frac{4E_C(1 - n_g)}{\Delta E} \right). \tag{2.83}$$

Differentiating Eqn. 2.72 with respect to n_g, we get

$$\frac{\partial E_{G,E}}{\partial n_g} = \pm \frac{8E_C^2(1 - n_g)}{\Delta E}. \tag{2.84}$$

Substituting Eqn. 2.84 with Eqn. 2.83, we get

$$\langle n \rangle_{G,E} = \left(1 - \frac{1}{2E_C} \frac{\partial E_{G,E}}{\partial n_g} \right), \tag{2.85}$$

where the factor of ∓ 1 is absorbed in the differential term. Differentiating both sides by n_g gives

$$\frac{\partial \langle n \rangle_{G,E}}{\partial n_g} = \frac{-1}{2E_C} \frac{\partial^2 E_{G,E}}{\partial n_g^2}, \tag{2.86}$$

and substituting this into Eqn. 2.81 gives us the final result

$$C_Q^k = -\frac{C_g^2}{e^2} \frac{\partial^2 E_k}{\partial n_g^2}. \tag{2.87}$$

By differentiating Eqn. 2.84 and substituting into Eqn. 2.87, we get the quantum capacitance in terms of n_g for states $|G\rangle$ and $|E\rangle$

$$C_Q^{G,E} = \pm \frac{C_g^2}{C_\Sigma} \frac{4E_C E_J^2}{\Delta E(n_g)^3}. \tag{2.88}$$

Note that C_Q is positive for the ground state and negative for the excited state. The maximum (minimum) value for the quantum capacitance is at the degeneracy point ($n_g = 1$), and is $C_Q^{G,E} = \pm 4C_g^2 E_C / C_\Sigma E_J$. Away from $n_g = 1$, C_Q vanishes and $C_{\text{eff}} \rightarrow C_{geom}$. The capacitance is plotted in Fig. 2.17(b).

2.5 Conclusions

The physics of the superconducting double dot involves the parity effect seen in superconducting charge devices, the charge stability diagram of the double quantum dot, and the quantum capacitance observed in Cooper pair boxes. In the Chapter 4, we will combine all of these phenomena to provide the model of the SDD and provide experimental results to support the model.

2.6 Summary

- In superconducting aluminium, electrons near the Fermi energy form a multi-particle phase coherent state known as Cooper pairs. These are electron pairs with equal and opposite momentum and spin momentum.

- An energy gap Δ forms between the Cooper pairs and a spectrum of excited single particle states, known as quasiparticles. Quasiparticles are generated by the breaking of Cooper pairs: the pairs are excited by a phonon or photon with energy greater than 2Δ.

- Single charging effects are observed in with a sufficiently large resistance and charging energy, leading to nanodevices such as the single electron transistor and quantum dots.

- The free energy of superconducting single charge devices depends on the parity of the number of electrons on the island.

- Superconducting tunnel junctions with thin barriers are known as Josephson junctions. These devices have supercurrent which flows at zero source-drain bias and is proportional to the stored energy E_J. The Josephson junction is the key component of the superconducting qubit.

- States with a varying energy curvature with gate voltage can be detected via their quantum capacitance. This includes the anticrossings of coupled charge states in Cooper pair boxes and semiconductor double quantum dots.

EXPERIMENTAL METHODS

To fabricate the superconducting double dot, we use nanofabrication techniques, such as electron beam lithography, to define nanometre scale islands and junctions. The SDD needs to be measured at temperatures well below 1 K, in order to be superconducting and to suppress quasiparticle excitations. We also need to apply an external magnetic field in order to control the superconducting gap, Δ.

The following chapter describes the methods used to fabricate and measure the superconducting nanostructures. Specific techniques for individual experiments are described in the corresponding chapters.

3.1   Device fabrication

The devices measured in this thesis were fabricated at the Microelectronics Research Centre, Cavendish Laboratory Cambridge and the Nanoscience Centre, University of Cambridge. To create superconducting devices with nano-scale overlapping features, we use *shadow mask evaporation* - metal is evaporated onto a substrate through a mask suspended from the substrate surface. By changing the angle of evaporation, the shadow image of the mask is laterally displaced. Two or three evaporations at selected angles give the designed device.

3.1.1   Substrate

In this thesis, the devices were fabricated on 0.5 mm thick undoped silicon wafer, with a high resistivity (> 5000 Ω cm) and naturally-grown thin layer of silicon oxide (5 - 15 nm). The wafer is sawn into 1 cm^2 chips. A 20 nm layer of aluminium oxide is applied via Atomic Layer Deposition (ALD) to isolate the device from the charge noise induced by fluctuating two-level systems in the silicon substrate [129].

### 3.1.2   Electron-beam lithography and development
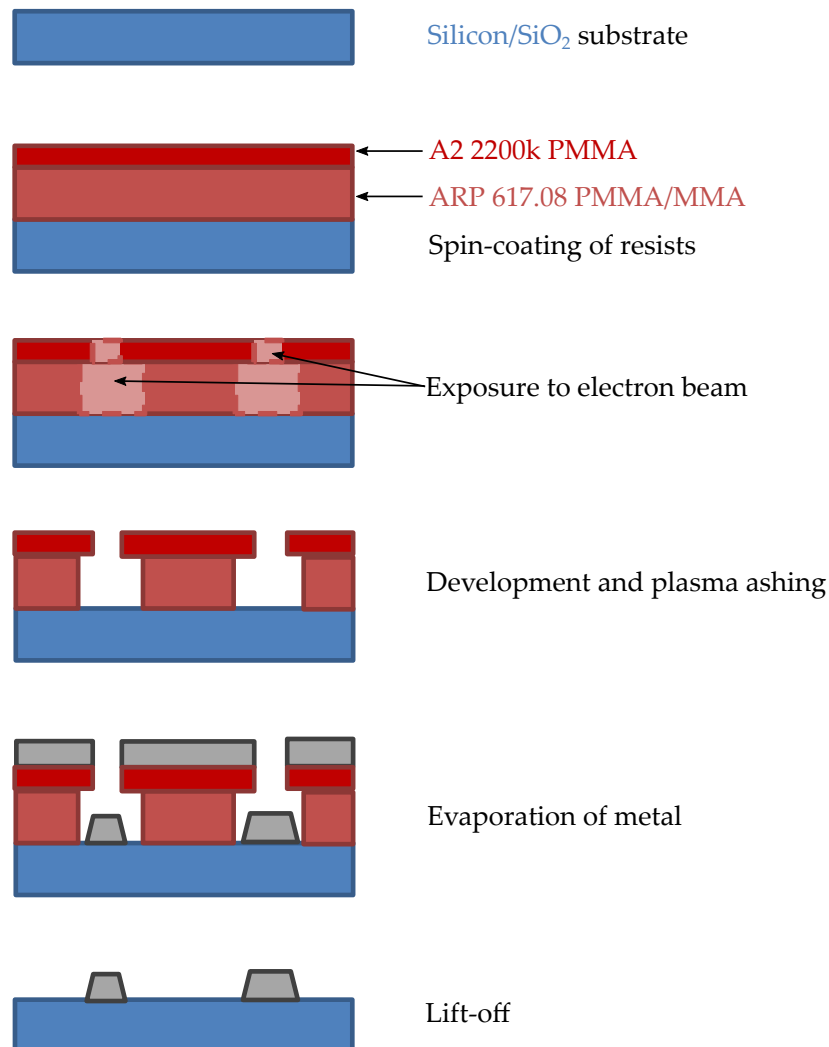
Figure 3.1: A schematic diagram indicating the stages in sample fabrication.

The first process is to coat the substrate with a resist, in which the pattern of the device will be written into by the e-beam. The coating is done in two stages: the first layer (Allresist ARP 617.08 PMMA/MMA co-polymer) is spin-coated onto the substrate (4000 rpm, with acceleration of 1400 rpm/s for 60 s) and then baked for 10 minutes at 180 °C on a hotplate. The substrate is then exposed to ultraviolet light for between 30 and 90 minutes, depending on device geometry and the substrate. The second resist layer (Microchem A2 2200k PMMA) is spin-coated onto the substrate (2400 rpm, 1400 rpm/s for 60 s), and the substrate is then baked again (10 mins, 160 °C).

The two layers are necessary for the multi-angle evaporation. The UV exposure to the first layer weakens the polymer bonds and makes it more sensitive to the e-beam than the second layer. Once the substrate has been exposed and developed, the second layer will overhang the first, acting as an aperture for the evaporated metal to be deposited on the substrate. The size of this overhang should be around 500 μm in order to fit in the pattern. A larger overhang will be unstable and prone to collapse.

The electron beam lithography is carried out using a 50 keV Crestec CABL-9000 electron beam lithography machine at the Nanoscience Centre clean room, University of Cambridge. Features smaller than 1 μm are written using a beam current of 100 pA at 0.2-0.3 μs with a pitch of 2 nm, and features great than 1 μm are written using a current of 10 nA at 1.5-2.0 μs with a pitch of 60 nm. Optimum dose times depend on the device geometry and substrate. The size of the resultant overhang is sensitive to the e-beam dose due to the back-scattering of the secondary electrons (see Fig. 3.2).

(a) 0.2 μs   (b) 0.3 μs   (c) 0.4 μs
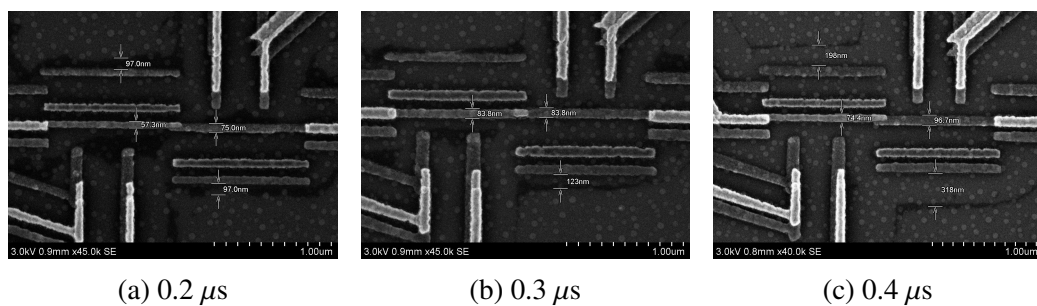
Figure 3.2: SEMs of a dose test for the superconducting double dot. Note the increasing distance between the nearest feature and the wall of the resist as the dose time is increased.

The sample is developed in a 1:3 solution of MIBK:IPA for 30 s, whilst rotating the sample in the horizontal plane to encourage removal of the exposed resist. The

sample is then placed and rotated in IPA for 30 s and is gently dried with a stream of nitrogen gas for 30 s. The resulting structure is delicate, so care is taken whilst moving the sample to keep the overhang intact [130].
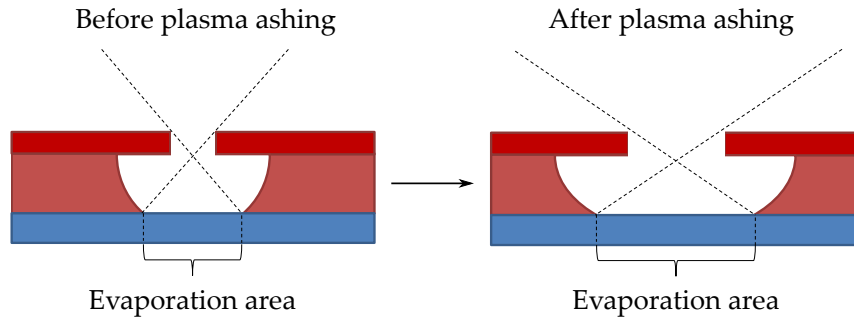

Figure 3.3: Sketch of the effect of plasma ashing on the window size and the evaporation area.

Finally, the sample is placed in an oxygen plasma asher (at a pressure of 0.4 mbar and RF power of 180 W for 15 s) to remove any residual resist within the confines of the developed region. This results in a larger window size and evaporation area (see Fig.3.3).

3.1.3 The evaporation process

3.1.3.1 Loading the evaporator

Metallic or superconducting tunnel junctions are fabricated via thermal evaporation of Al or manganese-doped aluminium (Al:Mn, 2% Mn). Manganese impurities in aluminium cause broadening in the BCS density of states and suppress superconductivity [131].

Sample wires are coiled up and placed in a tungsten basket, securely clamped in each turret in the evaporator chamber. The sample is mounted onto a metal stage with vacuum grease, and the stage is screwed onto an axle which is connected to a stepper motor.

For an effective evaporation, the chamber is required to be under high vacuum conditions (10^{-6} mbar). Liquid nitrogen is added to a cold trap to remove any residual water molecules within the chamber.

(a)

(b)

(c)
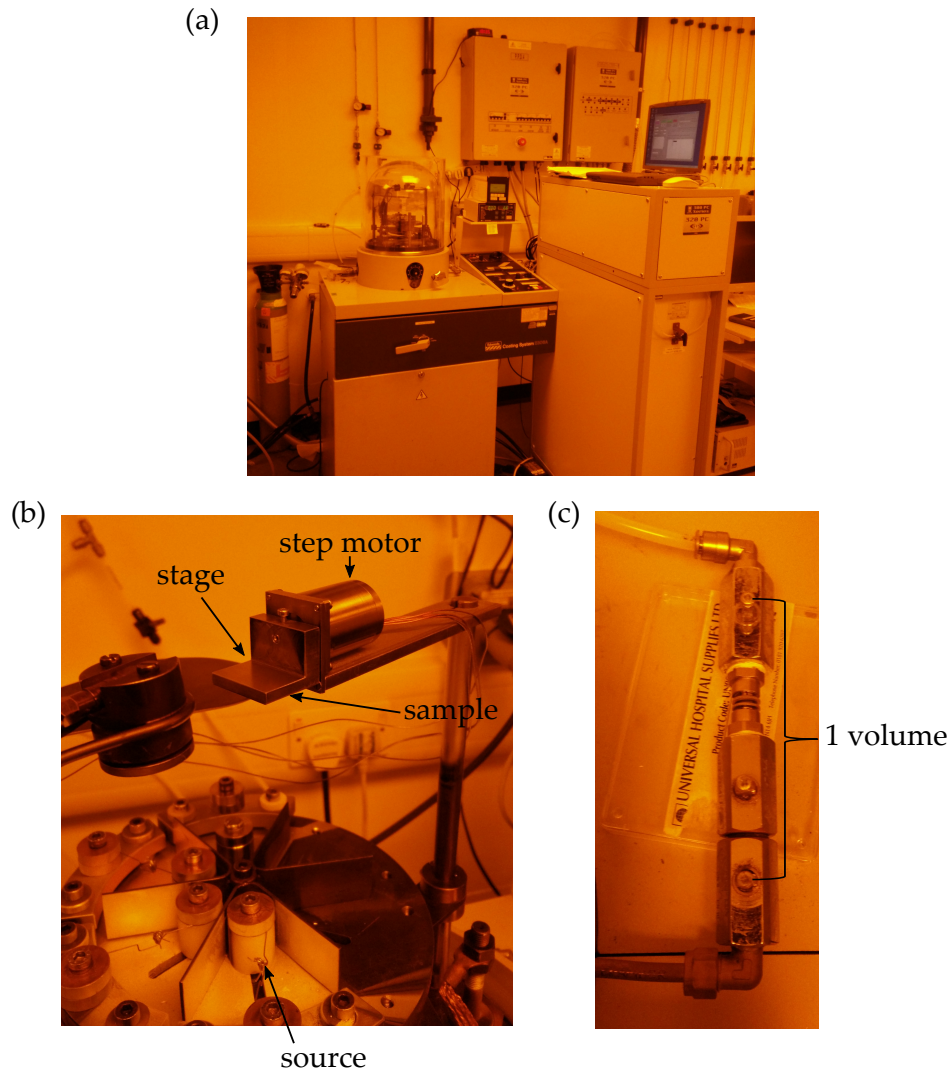
Figure 3.4: a) An Edwards thermal evaporator, modified for the use of shadow evaporation. b) A stage mounted to a stepper motor, controlled via a computer, to change the angle of evaporation. The sample is mounted to the stage via vacuum grease and is directly above the source metal, placed in a tungsten wire basket and clamped between the electrical turrets. c) An inlet with a manual valve allows oxygen to enter the chamber for controlled oxidation of the metal surface - the oxide formed is the insulating tunnel barrier.

3.1.3.2 Angle control

The evaporation angles are chosen so that the overlap between the islands create the geometry of the tunnel junction required. The angles are entered into a computer which controls, via a stepper motor, the angle of the rotating stage with respect to the tungsten

55
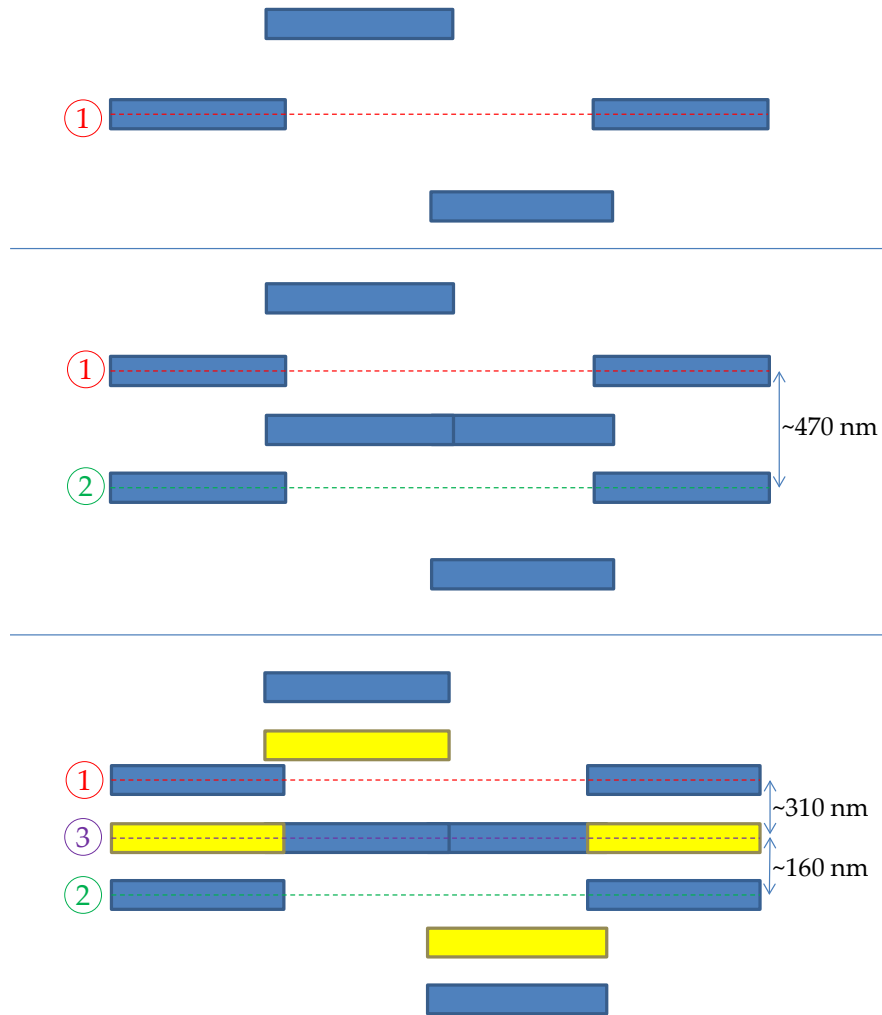
Figure 3.5: A schematic diagram showing how each evaporation stage defines the overall superconducting double dot pattern. Evaporations 1 and 2 define the superconducting double dots (Al, blue), and evaporation 3 defines the leads (Al:Mn, yellow). Large evaporation angles cause narrower depositions due to the smaller effective aperture; this is not shown on the diagram. Diagram not to scale.

basket. For the resist defined in Section 3.1.2, a change in angle of $\pm 1°$ corresponds to a displacement of approximately ± 10 nm. Fig. 3.5 shows an example of the order and relative positions of evaporations for a superconducting double dot device.

3.1.3.3 Evaporation and oxidation

Before starting the evaporation, the shutter, which separates the sample from the evaporation source, is closed. Once the first angle has been selected, a current is passed through the basket. The magnitude of current is adjusted until a steady evaporation rate is reached. It is necessary to wait approximately five seconds to outgas the metal of any impurities before opening the shutter. When the desired thickness of Al is reached, the sample is shielded from the evaporation source by a manually operated shutter and the current is turned off. The Al on the surface of the sample substrate is allowed to cool for 10 minutes before oxidation. Controlled oxidation allows an oxide to form on the surface of the Al which becomes the resistive tunnel barrier in the device. It is important to wait a significant amount of time for the sample to cool before oxidation, otherwise the oxidation will be rapid resulting in very resistive tunnel junctions. The turbo pump valve is closed and oxygen is let into the chamber via a fixed volume valve. Oxidation pressure and time are chosen to achieve the desired resistance of the tunnel junction. The chamber is pumped out again to a high vacuum ready for the next evaporation at the second angle.

3.1.3.4 Metal Lift-off

When all of the layers have been deposited, the sample is unmounted and then placed in acetone for 2 hours to lift-off the resist and unvalued Al from the substrate, followed by a 5 second ultrasonic vibration to encourage removal of any remaining resist. The sample is then cleaned in IPA, and dried with a stream of nitrogen gas.

3.1.3.5 Inspection and sample mounting

Each device is inspected using a scanning electron microscope (SEM) to check that there are no defects or discontinuities, and that the angles chosen have led to the expected result. Devices which are chosen to be tested are fixed (via General Electric (GE) Varnish) to a PCB with lumped element inductors and capacitors for the LC circuit, which is fixed onto the sample box (Section 3.3.4). The device is bonded to the PCB using a wedge bonder with 30 μm diameter Al:Si wires. Care is taken throughout handling to ensure that the devices are not at risk of electrostatic discharge (ESD), as this will destroy nanometre sized tunnel junctions (Fig. 3.6). Precautions include the

use of a grounding wrist strap during handling and bonding, and containing the sample box in a metallic or conductive box when transporting the sample.
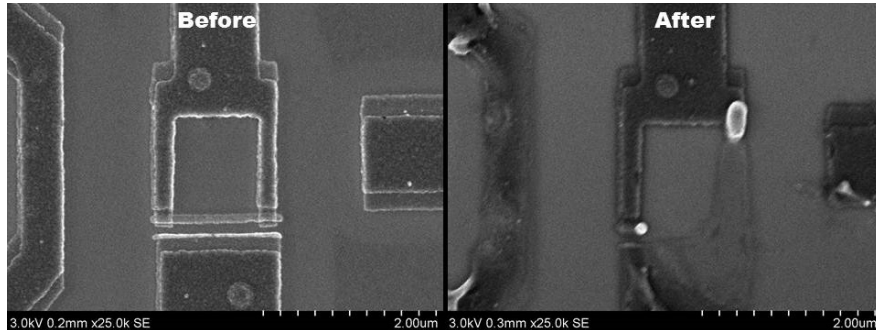

Figure 3.6: A cooper pair box before and after an ESD shock.

3.2 Cooling to mK - the dilution refrigerator

For Al superconducting devices, we require temperatures well below the critical temperature (T_c = 1.2 K) in order to thermally suppress quasiparticle excitations. Temperatures as low as ~1.75 mK have been achieved using a ^{3}He-^{4}He dilution refrigerator [133]. The measurements presented in this thesis were performed using an Oxford Instruments Kelvinox 400 dilution refrigerator, at the Hitachi Cambridge Laboratory. The refrigerator has a base temperature of approximately 35 mK. The temperature of the sample space can be increased by applying power to a heater coupled to the mixing chamber. A superconducting magnet provides a uniaxial field of 9 T maximum, in which the sample is mounted in plane or perpendicular to the field direction.

Fig. 3.7 shows a schematic diagram of a typical conventional dilution refrigerator. The dilution refrigerator exploits the phase separation in a ^{3}He-^{4}He mixture at low temperatures. At normal operating temperatures (T < 200 mK), the mixture separates into a ^{3}He-rich phase, which is almost pure ^{3}He, and a ^{3}He-dilute phase, which is 6.5% ^{3}He in ^{4}He. The superfluid ^{4}He acts as an inert background for a dilute Fermi gas of ^{3}He. The cooling mechanism is the endothermic process of ^{3}He atoms transferring from the low-enthalpy ^{3}He-rich phase to the high-enthalpy ^{3}He-dilute phase. The refrigerator acts to maintain a chemical potential gradient so that ^{3}He atoms continuously cross this phase boundary, resulting in cooling to mK temperatures within the mixing chamber.
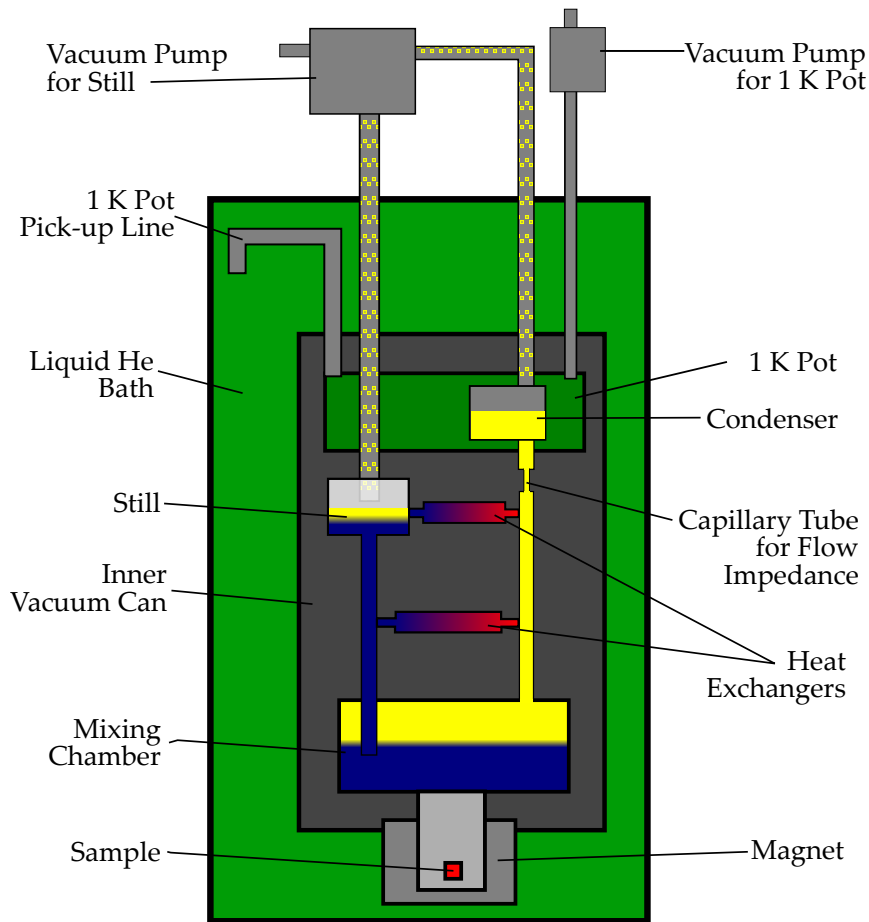
Figure 3.7: A schematic diagram of a dilution refrigerator. Original diagram from [132].

Details of operation of the dilution refrigerator can be found in Refs. [133, 134, 135, 136].

3.3 Radio frequency reflectometry

Radio-frequency reflectometry is a technique used to measure changes in impedance of a solid-state device. This is done by measuring the change in amplitude and phase of a microwave carrier signal reflected from a resonant circuit, in which the device is embedded, with respect to the incident signal. A circuit diagram of the setup is shown in Fig. 3.8 and is the typical setup for the measurements in this thesis. This section will give an overview and specifics of the setup.
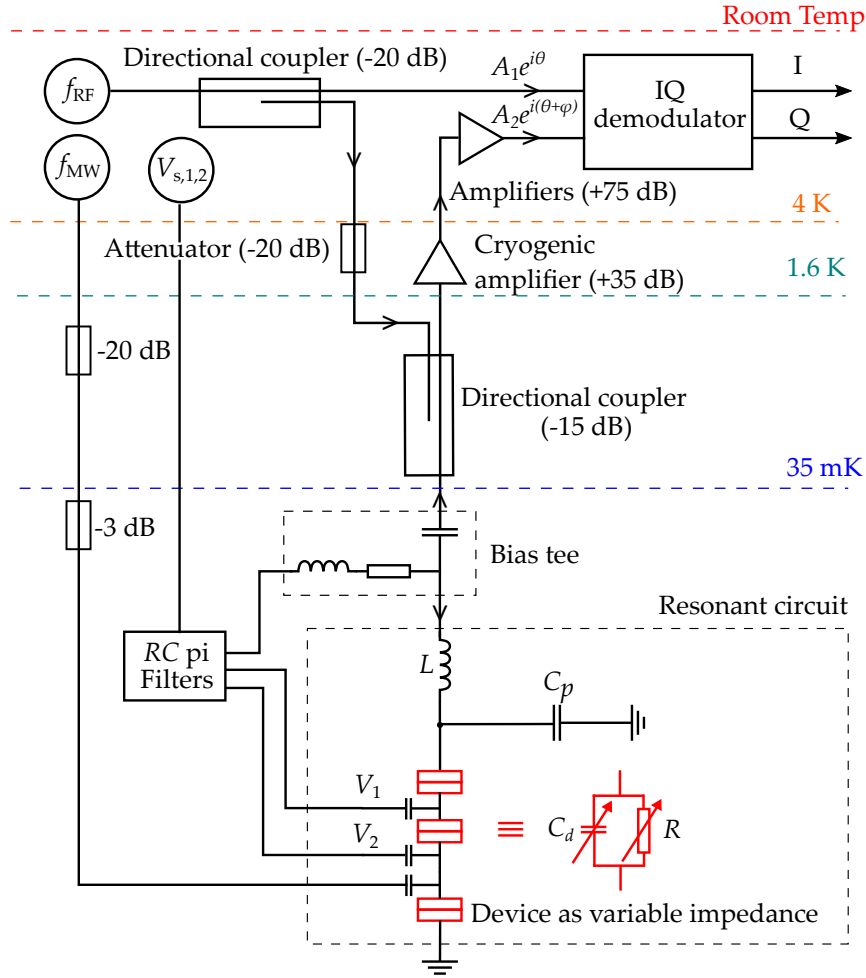
Figure 3.8: The experimental set-up for radio frequency (RF) reflectometry. The I and Q signals from the IQ demodulator are sent to a digital oscilloscope for digitization.

3.3.1 Overview

A radio frequency (RF) signal with amplitude A_1 and phase θ is transmitted from room temperature to the resonant circuit at mK and is reflected back with amplitude A_2 and phase $\theta + \varphi$. This reflected signal is homodyne demodulated, with the incident signal as a reference, to give their relative amplitude $A_2/A_1 = |\Gamma|$ and phase $\varphi = \arg(\Gamma)$. The devices presented in this thesis have a variable capacitance, which is measured as a phase shift at charge degeneracy points in this reflectometry experiment. Fig. 3.9 shows the amplitude and phase response of a typical circuit with a device as a function of frequency.
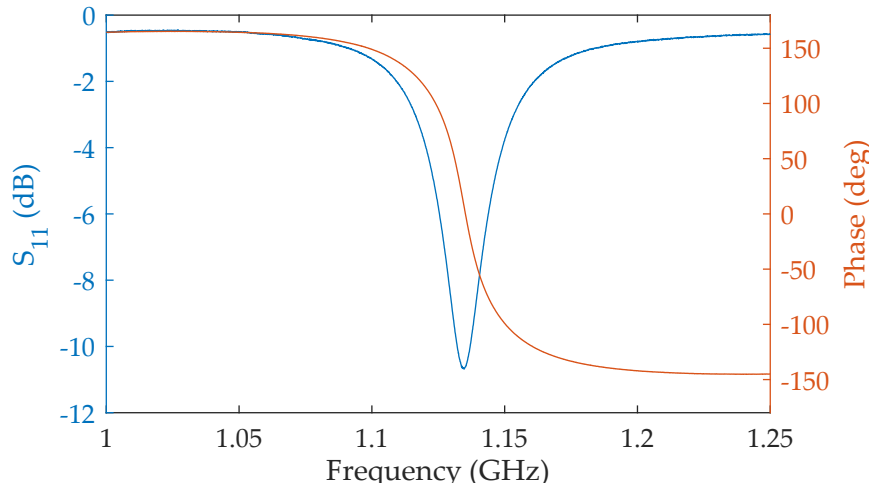
Figure 3.9: Reflected amplitude and phase response of a typical resonant circuit in a radio frequency reflectometry setup, with a quality factor $Q \approx 34$.

3.3.2 Resonant circuit

The components of the resonant circuit consist of a lumped element inductor, with inductance L, with a parasitic capacitance (C_p) to ground, and the embedded device with a total resistance R and capacitance C_d. The resonant frequency of the circuit is

$$\omega = \frac{1}{\sqrt{LC}}, \tag{3.1}$$

where $C = C_p + C_d$. The reflection coefficient is given by

$$\Gamma = \frac{Z - Z_0}{Z + Z_0}, \tag{3.2}$$

where Z_0 is the impedance of the transmission line ($\sim 50\Omega$) and Z is the impedance of the resonant circuit. With reference to the circuit diagram in Fig. 3.8, the impedance of the circuit is

$$Z = i\omega L + \frac{1}{i\omega C + R^{-1}} = \frac{R}{1 + \omega^2 C^2 R^2} + i\frac{\omega L - \omega C R^2(\omega^2 LC - 1)}{1 + \omega^2 C^2 R^2}, \tag{3.3}$$

Typically $RC^2 \gg L$ [109], so

$$Z \approx \frac{R}{1 + \omega^2 C^2 R^2} + i\frac{\omega C R^2(1 - \omega^2 LC)}{1 + \omega^2 C^2 R^2}. \tag{3.4}$$

At the resonant frequency of the circuit, $\omega_0 = 1/\sqrt{LC}$, Z is purely real and the reflection amplitude $|\Gamma|$ is at its minimum.

61

The phase of the reflected signal is

$$\varphi = \arg \Gamma = \tan^{-1}\left(\frac{-2\,|Z|\,Z_0}{|Z|^2 - Z_0^2}\right). \tag{3.5}$$

In Fig. 3.9, I plot an S_{11} measurement of a typical RF reflectometry setup using a Vector Network Analyser. This shows the power (blue) and phase (red) of the signal reflected from the resonant circuit. Near resonance, the phase is approximately linear in frequency. The phase either increases or decreases with frequency depending on whether the loaded impedance of the circuit, $|Z|$, is larger or smaller than the impedance of the transmission line, Z_0 [137]. It should be noted that, for an terminal impedance of the form in Eqn. 3.4, the total measured phase shift of the reflected signal can be greater than $180°$. This would not be the case for a transmission line terminated with a pure capacitance or inductance [138].

A change in the capacitance of the device causes a shift in the resonant frequency. By differentiating Eqn. 3.1, we can express this shift in terms of a small change in capacitance, dC;

$$d\omega = -\frac{1}{2}\frac{1}{\sqrt{L}C^{3/2}}dC. \tag{3.6}$$

The measured phase shift is therefore given by

$$d\phi = \left.\frac{d\phi}{d\omega}\right|_{\omega=\omega_0} d\omega = \left.\frac{d\phi}{d\omega}\right|_{\omega=\omega_0} \cdot -\frac{1}{2}\frac{1}{\sqrt{L}C^{3/2}}dC, \tag{3.7}$$

and for a known inductance the corresponding change in capacitance can be deduced.

3.3.3 Quality factor

An alternative way to calculate the capacitance shift is from the quality factor, Q, of the resonator. Q describes the energy loss in the system, and is defined as

$$Q = 2\pi\frac{\text{Energy stored}}{\text{Energy loss per cycle}} = \frac{\omega_0}{\Delta\omega}, \tag{3.8}$$

where $\Delta\omega$ is the full-width-half-maximum (FWHM) bandwidth of the resonator [139]. There are two sources of loss in the system, the internal loss in the resonator circuit (i.e. the resistance of the device, R) and the external loss between the circuit and the transmission line. These losses are characterised by the quality factors $Q_{\text{int}} = R\sqrt{C/L}$ and $Q_{\text{ext}} = 1/Z_0\sqrt{L/C}$, respectively. Therefore, the total quality factor is [125, 140]

$$Q = \left(\frac{1}{Q_{\text{int}}} + \frac{1}{Q_{\text{ext}}}\right)^{-1}. \tag{3.9}$$

The Q-values of resonators in typical RF reflectometry setups are usually dominated by external losses (i.e. $Q_{ext}^{-1} \gg Q_{int}^{-1}$), and are usually within the range $\sim 10 - 40$ [127, 120].

The change in capacitance, dC, and change in phase $d\phi$ are approximately related by [141]

$$d\phi \approx \frac{\pi Q}{C_p} dC. \tag{3.10}$$

3.3.4 Sample box

The sample box (as shown in Fig. 3.10) is designed to be "light-tight" to protect the sample from background radiation. Background microwave and infrared photons, from either the apparatus or some noise source, cause uncontrolled quasiparticle generation [13]. A major source of these photons is from blackbody radiators in the refrigerator. The sample box, made from oxygen-free copper, is coated in silicon carbide, epoxy and carbon powder, which is designed to strongly absorb radiation with wavelengths of the order of 1 mm [142]. Eccosorb microwave absorbent material[a] is placed inside and around the copper sample box of the refrigerator to further shield the device from stray photons. Aluminium tape is placed to cover gaps around the box which photons may leak through.

3.3.5 DC electronics

The DC gate voltages (V_1 and V_2 in Fig, 3.8) are controlled using a Tetronix Arbitary Function Generator (AFG3012). A loom of twelve twisted-pair wires carry the DC voltages from a BNC breakout box, which has ground switches for each connection, to the sample box fixed to the cold finger. These grounding switches keep the sample at ground whilst electrical contact is established, preventing any potential ESD destroying a device via a floating voltage. The wires are made from copper at room temperature stages, from constantan at low temperature stages, and copper once at 30 mK.

Whilst the phonon bath is kept at a low temperature, it is also crucial to keep the electron temperature at a minimum. Cryogenic filters are used at the mK state. These

---

[a]Eccosorb-SF, manufactured by Laird Technologies, absorbs 99% of radiation between 1 - 18 GHz.[143]
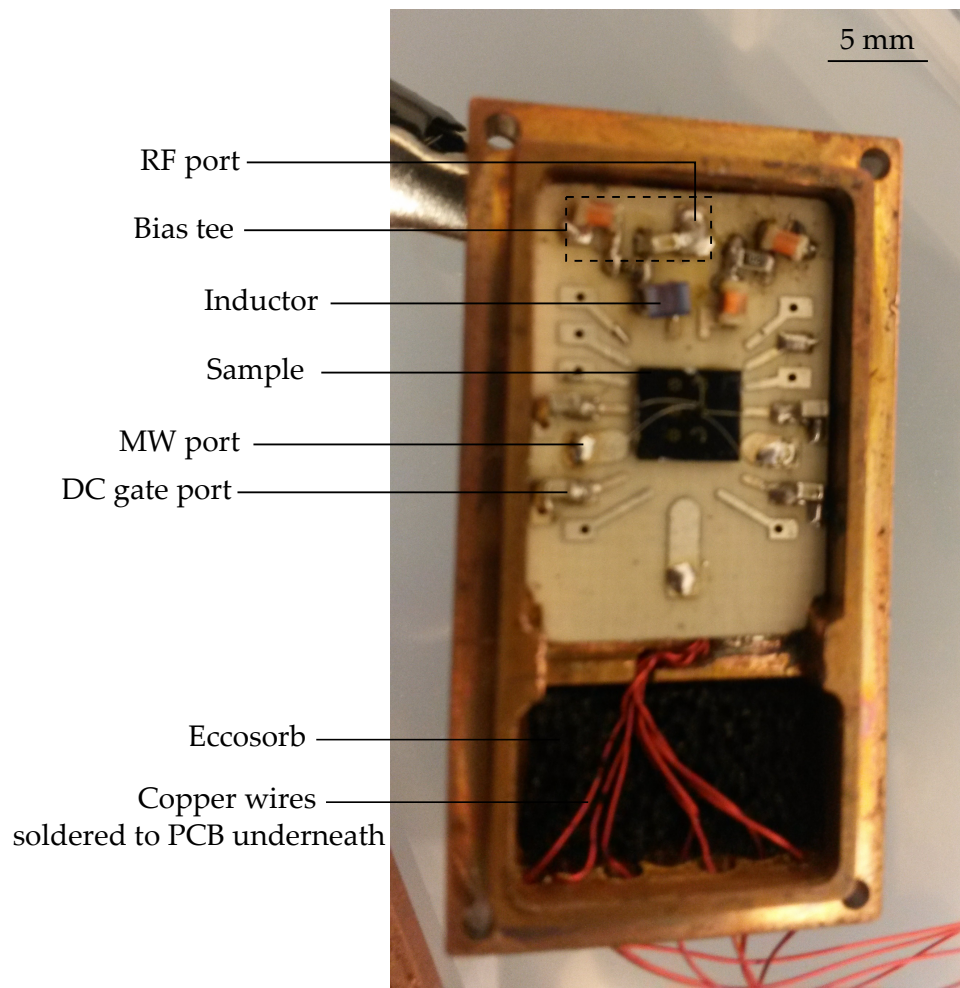
Figure 3.10: An annotated photograph of a sample bonded to a PCB and mounted in a sample box. The source is bonded to an inductor which acts as a resonator. This inductor is part of a bias tee in which both a DC bias and a RF signal for reflectometry can be applied to the same port. The drain lead is bonded to capacitors which are connected (via the groundplane on the back of the PCB) to the box and act as an RF ground.

are RC pi-filters[b] and filter signals from 1 kHz up to 1 GHz. They are made from a copper-core PCB and are enclosed in an oxygen-free copper box, for high thermal conductivity. Eccosorb is also placed around the copper wiring and acts as a filter against background radiation above 1 GHz [1, 3].

---

[b]Manufactured by Tebira Ltd., based in Cambridge.

64

3.3.6 RF electronics

A Rohde and Schwarz SMB100A signal generator is used to produce an RF signal for reflectometry. The RF signal is carried by UT-141 coaxial cables with a conducting material of copper (at room temperature and at 30 mK) or stainless steel (at intermediate temperature stages). Anritsu RF attenuators are added at each cooling stage in the refrigerator to suppress the Johnson-Nyquist noise from the warmer stage. Johnson-Nyquist noise is electrical noise generated by the thermal motion of charge carriers. The noise power spectral density, or voltage variance per Hertz of bandwidth, of a resistor R at temperature T is given by

$$\left\langle V^2 \right\rangle = 4k_B R T \Delta f, \tag{3.11}$$

where Δf is the measurement bandwidth [144]. For example, at the 4 K stage of the refrigerator, a 20 dB attenuator will reduce the noise equivalent power from the room temperature stage by a factor of 100, to an equivalent temperature of ~3 K. The dominant noise source is now the attenuator itself, so further attenuation at this cooling stage is not necessary [130].

The reflected signal from the sample is amplified by a QuinStar [c]cryogenic amplifer at the 4 K stage. The amplifer has a 300 - 400 MHz pass band, and so the components of the LC circuit are chosen such that the resonant frequency lies within this pass band. The signal is amplified further at room temperature and is then demodulated with the input signal into in-phase (I) and quadrature components (Q) by a Polyphase AD0105B quadrature demodulator. These are output as quasi-DC voltages and are digitised by a LeCroy WaveRunner 104Xi oscilloscope. The amplitude and phase of the reflected signal are:

$$A = \sqrt{I^2 + Q^2}, \tag{3.12}$$

$$\phi = \tan^{-1} \frac{Q}{I}. \tag{3.13}$$

Microwave photons are applied to the sample from an Anritsu microwave signal generator and are carried through an additional coaxial line. This is used for microwave spectroscopy to investigate the energy bandstructure of a device, as well as to induce Cooper pair breaking in the SDD.

---

[c]Model No. QCA-U350-30H

3.3.7 Measurements in superconducting and metallic devices
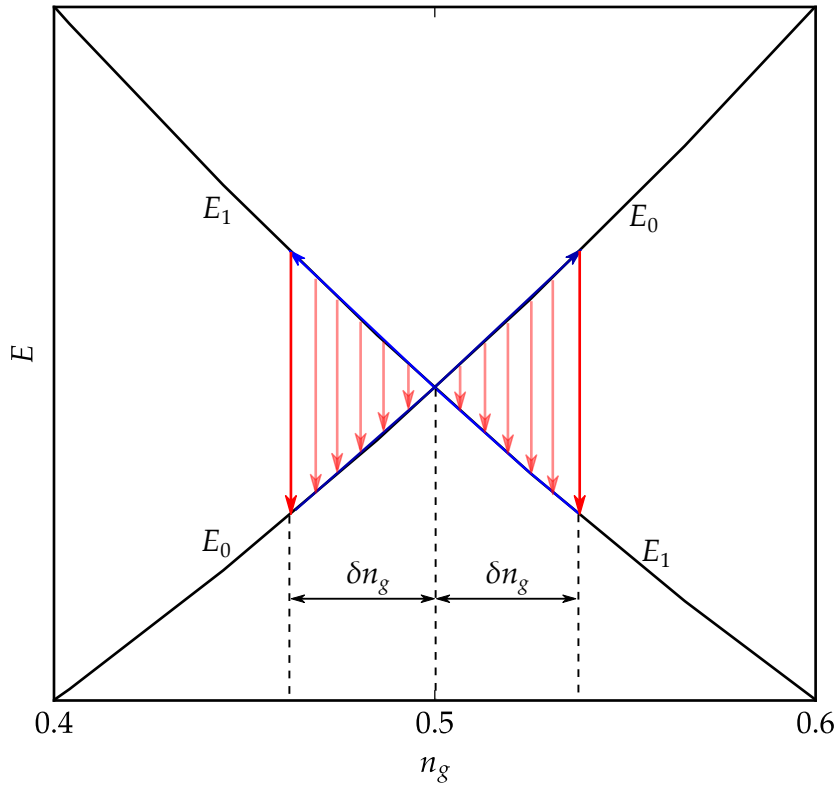
Figure 3.11: A diagram showing the process behind Sisyphus impedance in a metallic SET. E_0 and E_1 are the electrostatic energies of two charge states. In this example, the gate of the SET is biased at $n_g = 0.5$. The RF signal, with amplitude δn_g, drives the system past the degeneracy point and into an excited state (blue arrows), whilst at the same time charging the system. When the system eventually relaxes via charge tunnelling (red arrows), the energy is dissipated from the system. This process occurs every half RF cycle [139].

RF reflectometry has been used to measure quantum capacitance and detect quantum states in superconducting devices, such as Cooper pair boxes [120] and superconducting SETs [127]. RF reflectometry has also been used to measure tunnelling in metallic structures, such as single electron boxes [125] and single electron transistors [145]. The mechanism responsible for this is an effective impedance known as Sisyphus impedance, which consists of a dissipative and dispersive response of the device of a sufficiently fast RF drive [146].

Fig. 3.11 illustrates the process behind Sisyphus impedance. When an SET is biased towards a degeneracy point and an RF signal is applied, the SET is cyclically driven into an excited state. If the tunnelling rate is comparable to the frequency of the RF drive, the electrons tunnel on average after the degeneracy points has passed, resulting the SET being an excited state. At each half of the RF cycle, the SET relaxes to the lower energy state, causing energy dissipation. This results in a reduction in reflected power. This dissipative response is known as Sisyphus resistance [145]. There is also an associated tunnelling capacitance (which is distinct from quantum capacitance) due to the electron tunnelling being out of phase with the RF excitation [128]. These changes in resistance and reactance are together known as the Sisyphus impedance [146].

3.4 Analysis of random telegraph signals

Processes involving Markovian switching between two states often result in the experimental measurement of an asymmetric random telegraph signal (RTS), as shown in Fig. 3.12(a). An RTS is characterised by a signal switching between two levels a_0 and a_1, with a switching rate from a_0 to a_1 (a_1 to a_0) of $\Gamma_{0(1)}$. In Chapters 5 and 6, time domain measurements of capacitance yield random telegraph signals, due to stochastic switching between charge states.

The probability of a switching event with a mean average rate Γ to occur within a time interval t is

$$P = \Gamma t e^{-\Gamma t}. \tag{3.14}$$

The rates can therefore be extracted by recording the dwell times for each state (i.e. the individual time periods for which the signal remains above or below a specified threshold), plotting into a histogram and fitting to an exponential decay (Fig. 3.12(b)) [147].

3.4.1 Measurement difficulties

The presence of Gaussian noise may cause the signal to cross the level thresholds, leading to incorrect dwell time measurements. This can be dealt with to a certain extent by using a Schmidt trigger type algorithm, where different thresholds are used for entering and leaving the state.
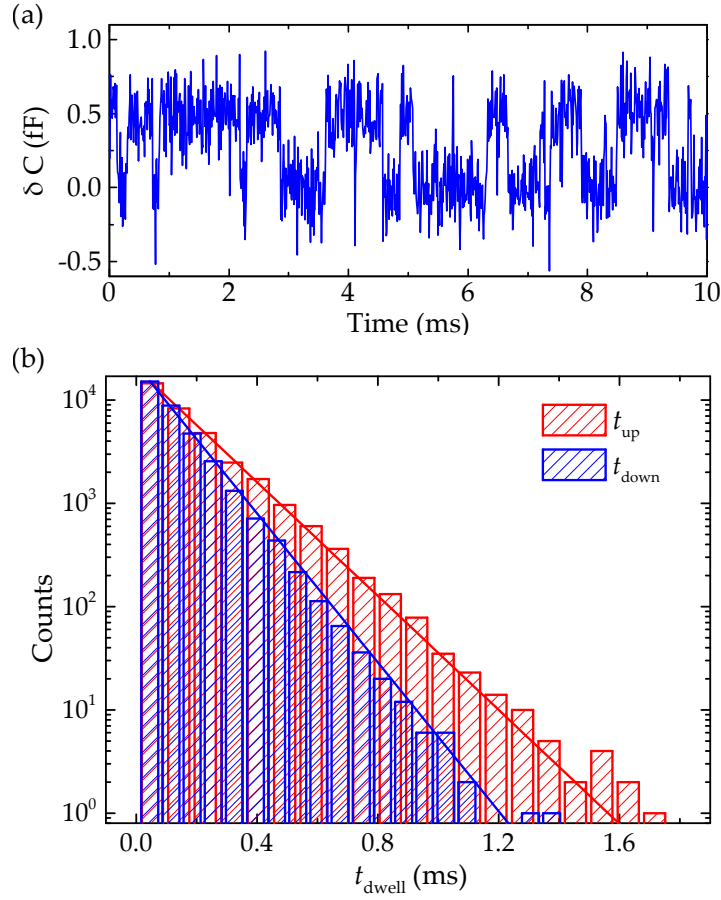
Figure 3.12: (a) An 10 ms extract of a typical time trace of the capacitance shift δC. The capacitance shift is calculated from the phase and reflected amplitude of the signal. (b) An example histogram of the dwell times in each capacitance state. t_{up} refers to the dwell time of the upper capacitance state, and t_{down} the lower state.

The limited bandwidth of the measurement apparatus is a further difficulty. If the bandwidth is not much greater than $\Gamma_0 + \Gamma_1$ than short-lived dwells in a particular state may be missed. This not only removes a short dwell time that should have been counted, but joins two longer time periods together in to one.

Low-pass filters are used to reduce the Gaussian noise in the switching trace. This is necessary in order to observe switching and determine the Capacitance thresholds, but also limits the bandwidth of the measurement to $\Delta f = 150$ kHz. This results in the measured rates (Γ_0^*, Γ_1^*) being less than the actual rates of the underlying system. This is dealt with by generating a series of synthetic time traces (10 s, 1.2×10^9 samples per second), with known switching rates, and the same noise profile as the experimental
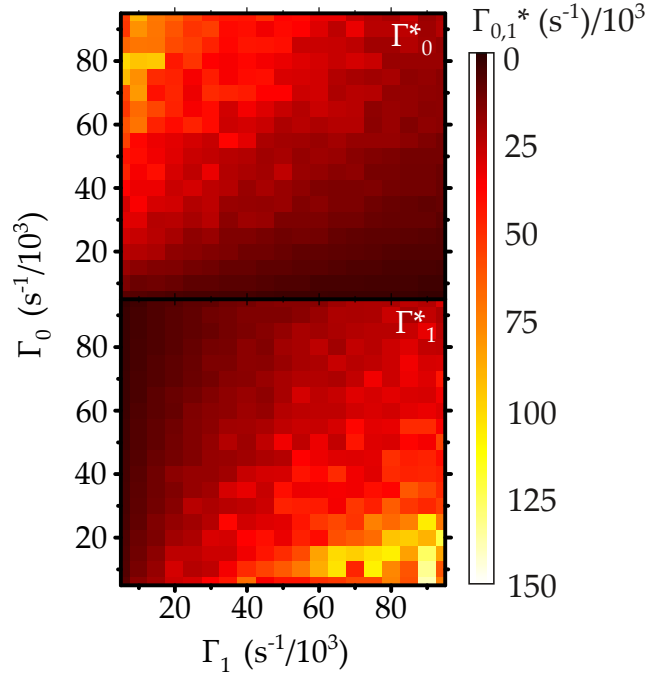
Figure 3.13: Calibration data for converting the measured rates ($\Gamma^*_{0,1}$) to the actual rates ($\Gamma_{0,1}$).

signal. By measuring the rates of these traces with the experimental set-up, we extract a correction table between the measured rates and Γ_0, Γ_1 (Fig. 3.13).

In Chapter 6, we are also required to accurately determine a_0 and a_1. To do this we use the probability density function (PDF) of a filtered RTS with no noise [148],

$$f(y) = \begin{cases} q_0 f_0(y) + q_1 f_1(y) & a_0 \leq y \leq a_1 \\ 0 & \text{otherwise,} \end{cases} \quad (3.15)$$

with

$$f_0(y) = \frac{a^{-1}\eta_0^{u_0-1}\eta_1^{u_1}}{B(u_0, u_1 + 1)} \quad f_1(y) = \frac{a^{-1}\eta_0^{u_0}\eta_1^{u_1-1}}{B(u_0 + 1, u_1)}. \quad (3.16)$$

Here,

$$B(x, y) = \int_0^1 t^{x-1}(1 - t)^{y-1}dt \quad (3.17)$$

is the Beta function, a_0 (a_1) is the lower (upper) level of the RTS, $a = a_1 - a_0$, $q_{0,1} = 1 - \Gamma_{0,1}/(\Gamma_0 + \Gamma_1)$, $\eta_j = |y - a_j|/a$, and $u_j = \Gamma_j\tau$, with τ being the measurement bandwidth. To include the effect of experimental noise, we convolve this expression with a Gaussian function with a width equal to the noise amplitude. We then fit the
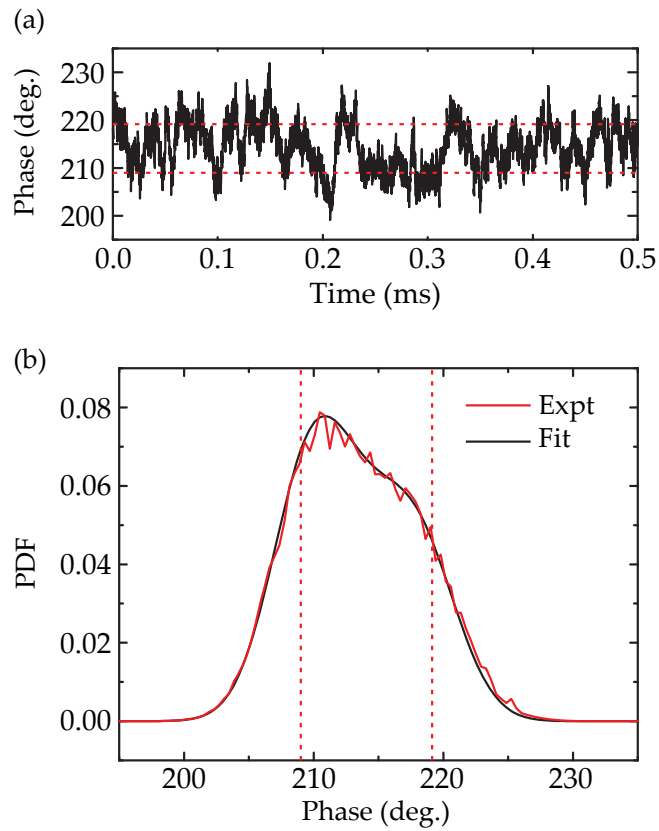
Figure 3.14: (a) A short section of a typical RTS with a low signal-to-noise ratio (SNR). (b) The PDF for a 10 s signal (red) with a fit to Eqn. 3.16 (black). The levels a_0 and a_1, marked with dashed red lines in both (a) and (b), are not coincident with the peaks of the PDF.

resulting expression to the PDF of the measured RTS (Fig. 3.14 - the extracted levels a_0 and a_1 are marked with dashed red lines).

3.5 Summary

- Nano-fabrication techniques used to fabricate the double dot structures were described. In particular, the triple angle shadow evaporation technique was outlined to show how the superconducting double dot is formed.

- The operation of a dilution refrigerator is discussed, in which samples are measured at phonon temperatures as low as 35 mK.

- The setup for radio frequency reflectometry at low temperatures has been presented, including methods to reduce electron temperature and non-equilibrium quasiparticle generation by signal filtering and absorbing background radiation.

THE SUPERCONDUCTING DOUBLE DOT

A superconducting double dot (SDD) comprises two superconducting Al islands coupled by a Josephson junction with each island connected to a normal metal lead. It is therefore similar to a semiconductor double dot, but rather than electrons, the SDD allows electrostatic control of Cooper pairs and Bogoliubov quasiparticles. In this section, we study the charge stability diagram of an SDD. We use its quantum capacitance to detect the anticrossings between coherently coupled Cooper pair charge states, and an independent superconducting charge sensor to directly measure the charge occupancy of the device. This work was done in collaboration with Dr Nicholas Lambert, and is published in Applied Physics Letters [2].

4.1 Device overview

A circuit diagram of the SDD is shown in Fig. 4.1. The van der Wiel charging energies [113] of the islands, E_{C1} and E_{C2}, and the coupling energy, E_{Cm}, are dominated by the capacitances of the junctions, a situation analogous to the metallic double dot (Chapter 2, section 2.2.5). We consider the regime $E_{C1,C2,Cm} \gg k_B T$, where we observe single charging effects. Depending on the magnitude of Δ relative to $E_{C1,C2}$, unpaired quasiparticles may be observed (known as the parity effect, Chapter 2, section 2.3.1). The Josephson energy of the middle tunnel junction, $E_J < E_{C1,C2}$, couples charge states
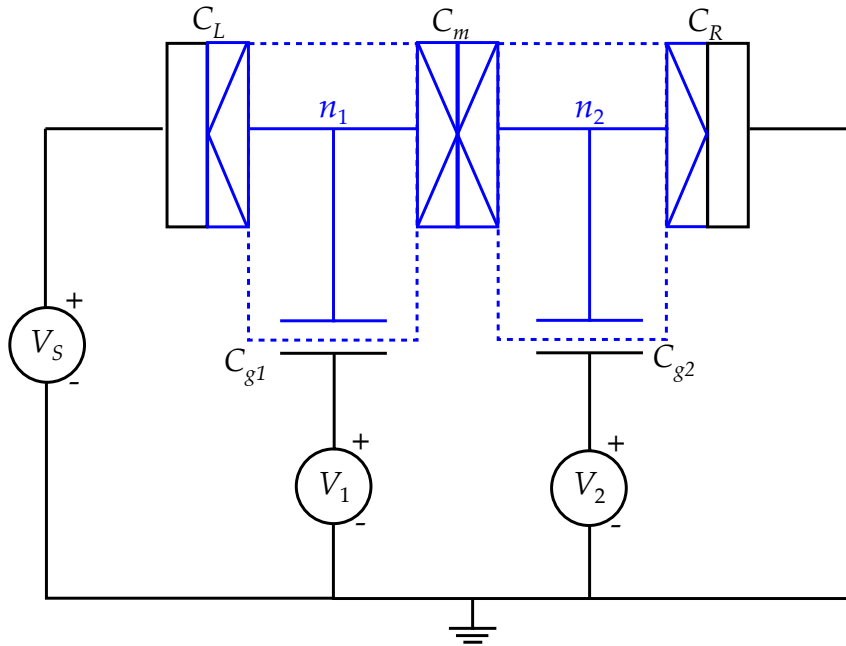
Figure 4.1: Schematic diagram of a superconducting double dot. The gate voltages $V_{1(2)}$ control the electrochemical potential of the left (right) dot. In this experiment the source-drain bias (V_S) is kept at zero, except when measuring Coloumb diamonds to determine the charging energies.

involving coherent tunneling of Cooper pairs, like that in a Cooper pair box (Chapter 2, section 2.3.3).

4.1.1 SDD Hamiltonian

The charge states are labelled (n_1, n_2), where $n_1(n_2)$ is the total offset charge (in units of e) from an arbitrarily chosen *even* parity state on the left (right) island. For even state parities, the ground state is the Cooper pair condensate, and the electrostatic energy $U_{el}(n_1, n_2)$ is the same as in a metallic double dot (see Eqn. 2.39 and van der Wiel et al. [113]). If either n_1 or n_2 is odd, then there is an unpaired quasiparticle which occupies the lowest available state with energy Δ. If both n_1 and n_2 are odd, there is one quasiparticle in each dot. The total internal energy is therefore

$$U = U_{el}(n_1, n_2) + \Delta (n_1 \bmod 2 + n_2 \bmod 2). \tag{4.1}$$

Including the off-diagonal components for Cooper pair tunnelling, we get the Hamiltonian of the SDD

$$
\begin{aligned}
H = & \sum_{n_1,n_2} (U_{el} + \Delta \, (n_1 \bmod 2 + n_2 \bmod 2)) \, |n_1, n_2\rangle \, \langle n_1, n_2| \\
& - \sum_{n_1,n_2 \text{ even}} \frac{E_J}{2} \, (|n_1 + 2, n_2\rangle \, \langle n_1, n_2 + 2| + |n_1, n_2 + 2\rangle \, \langle n_1 + 2, n_2|) \, .
\end{aligned}
\tag{4.2}
$$

4.1.2 Free energy of the SDD

To build the charge stability diagram of the SDD, we calculate the Helmholtz free energy $F = U - TS$ and plot the charge state which has the lowest free energy as a function of V_1 and V_2. The internal energy, U, is calculated using Eqn. 4.1. In the low temperature limit, $\Delta/k_B T \gg 1$, the entropy S for one quasiparticle in a superconducting island of volume V is $S = k_B \ln N_{eff}$, where $N_{eff} = 2\sqrt{2\pi} V D(E_F) \sqrt{\Delta k_B T}$ is the number of available quasiparticle states. $D(E_F)$ is the single spin normal state density of states at the Fermi energy (Chapter 2, section 2.1.5.1) [64, 149].

The free energy of the system is therefore

$$
F = U_{el} + \tilde{\Delta}(n_1 \bmod 2 + n_2 \bmod 2)
\tag{4.3}
$$

where $\tilde{\Delta} = \Delta - k_B T \ln(N_{eff})$.

4.2 Calculations for an ideal device

We calculate the free energy of the SDD in an ideal device with no cross capacitances between the gate $V_{1(2)}$ and dot 2 (1). We set $C_L = C_R = 0.8$ fF and $C_m = 0.4$ fF. These are much larger than the gate capacitances , and so dominate the charging energies $E_{C1} = E_{C2} = E_C = 150\ \mu\text{eV}$ and $E_{Cm} = 50\ \mu\text{eV}$. We also set the superconducting gap at zero magnetic field $\Delta_0 = 225\ \mu\text{eV} = \frac{3}{2}E_C$. The resistance of the middle tunnel junction is set at 20 kΩ, which gives a zero field E_J of 24 μeV. The volume is set to a typical $2 \times 10^{-3} \mu\text{m}^3$, giving $N_{eff} \sim 5,000$.

The charge stability diagram is periodic in gate charge. Therefore, taking a similar approach to the Cooper pair box, we only need to consider $-1 \geq (n_1, n_2) \geq 1$.
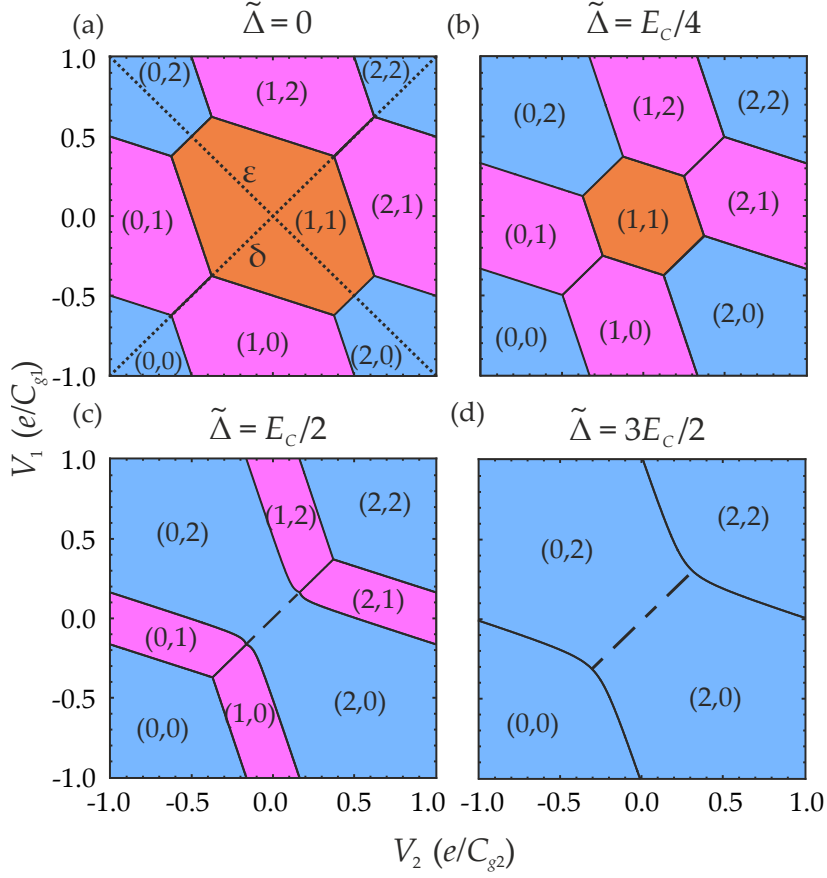
Figure 4.2: Theoretical charge stability diagrams for (a) $\tilde{\Delta} = 0$, (b) $\tilde{\Delta} = E_C/4$, (c) $\tilde{\Delta} = E_C/4$, (c) $\tilde{\Delta} = E_C/2$, (d) $\tilde{\Delta} = 3E_C/2$. Blue regions are Cooper pair states, pink regions have one quasiparticle present, and the red region has one quasiparticle on each island. Dashed lines in (c) and (d) correspond to anticrossings of the hybridised (2,0) and (0,2) levels. Dotted lines in (a) show the diagonal (δ) and the antidiagonal ε axes.

4.2.1 Charge stability diagram

The calculated charge stability diagram is shown in Fig. 4.2 in four different regimes, and the free energies of each charge state against the antidiagonal ε and diagonal δ detunings (as marked in Fig. 4.2(a)) in Figs. 4.3 and 4.4 respectively.

For $\tilde{\Delta}/E_C = 0$ the stability diagram is that of a metallic double dot (Fig. 4.2(a), see section 2.2.5). Increasing $\tilde{\Delta}/E_C$ leads to the odd parity charge states decreasing in area, as the energy cost for quasiparticles increase (Fig. 4.2(b)). When $\tilde{\Delta}/(E_C - E_J) > 1/2$, the (1,1) state is now higher in energy the Cooper pair states, and the ground state at $V_1 = 0, V_2 = 0$ is the symmetric combination of the Cooper pair states, $\frac{1}{\sqrt{2}}(|2,0\rangle + |0,2\rangle)$ (Fig. 4.2(c)). As $\tilde{\Delta}/E_C$ is increased further, the single quasiparticle charge states also
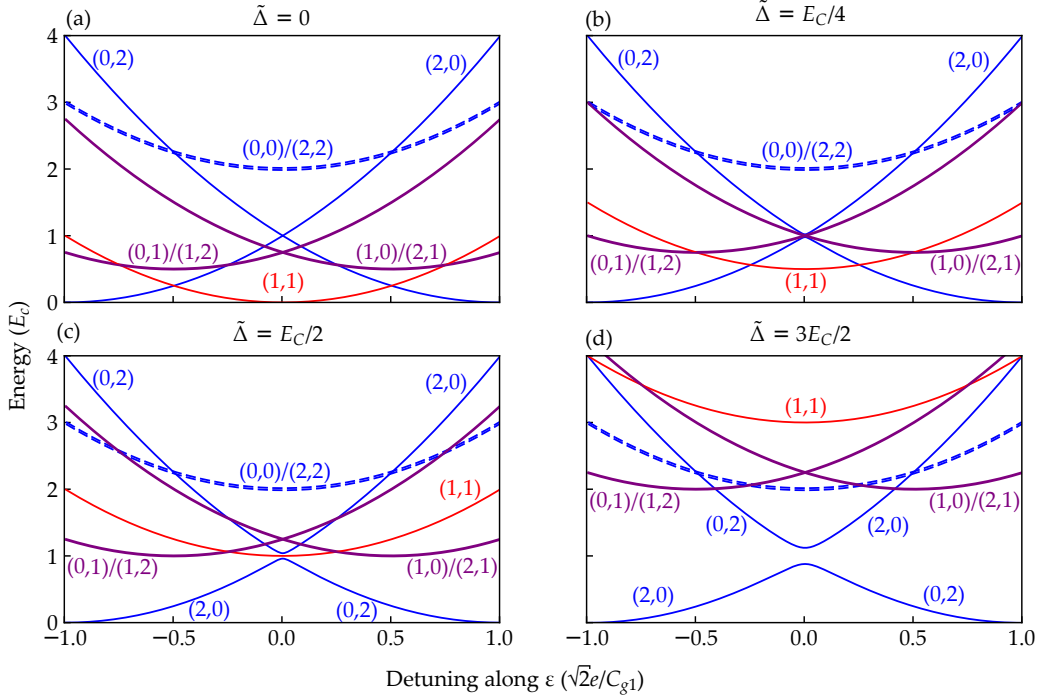
Figure 4.3: Free energy of the charge states along the ε-axis in Fig. 4.2 for (a) $\tilde{\Delta} = 0$, (b) $\tilde{\Delta} = E_C/4$, (c) $\tilde{\Delta} = E_C/2$, (d) $\tilde{\Delta} = 3E_C/2$. Colours are as for Fig. 4.2.

disappear from the stability diagram, leaving only the Cooper pair states (Fig. 4.2(d)). In addition, an anticrossing appears between the (2,0) and (0,2) states, analogous to the anticrossings observed in semiconductor double quantum dots (Chapter 2, section 2.2.6) and Cooper pair boxes (Chapter 2, section 2.3.3).

4.3 Experimental evidence of charge states

The $(0, 2)/(2, 0)$ anticrossing near zero detuning leads to a quantum capacitance shift relative to the other charge states, which can be detected via rf reflectometry. However, since none of the other charge states have a quantum capacitance, in general we need a charge sensor to measure the charge state of the device. A charge sensor is a nanodevice which responds to a change in charge of the local environment with a change of its impedance. This can either be a change in resistance, for example in SETs [72], or a change in reactance (i.e. capacitance [119, 120, 141] or inductance [150]). Measuring a change in reactance offers advantages over measurements of resistance, such as overcoming the shot noise limit for dissipative charge sensors [151]
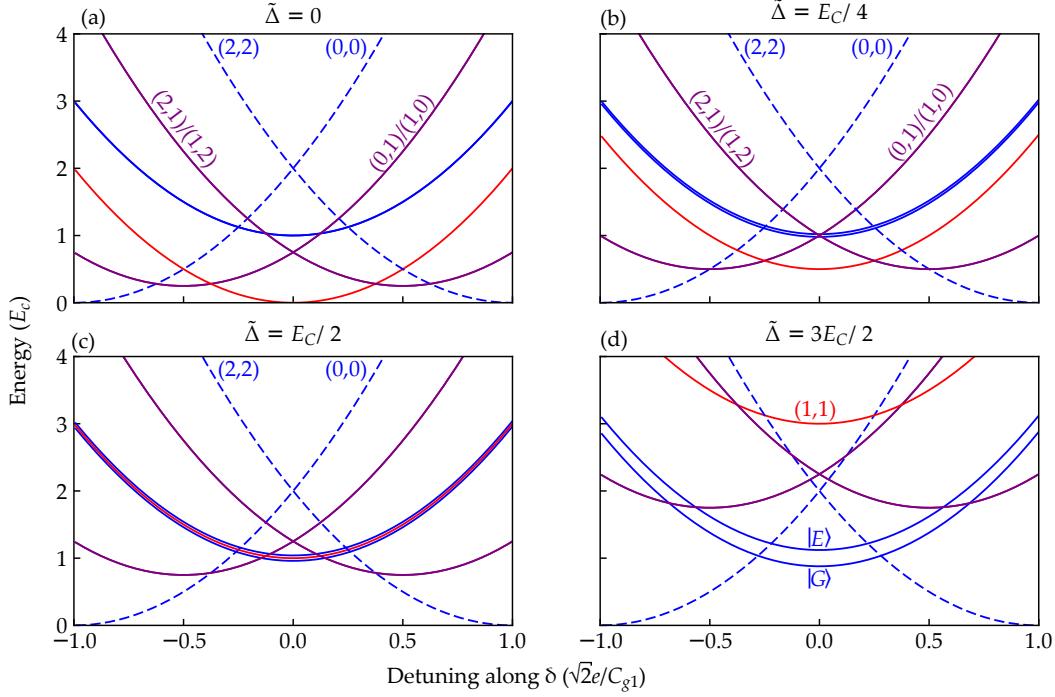
Figure 4.4: Free energy of the charge states along the δ-axis in Fig. 4.2 for (a) $\tilde{\Delta} = 0$, (b) $\tilde{\Delta} = E_C/4$, (c) $\tilde{\Delta} = E_C/4$, (c) $\tilde{\Delta} = E_C/2$, (d) $\tilde{\Delta} = 3E_C/2$. In Fig. (d), $|G\rangle$ and $|E\rangle$ correspond to the Cooper pair states which are a linear superposition of charge states (0,2) and (2,0). Colours are as for Fig. 4.2.

and reducing the backaction on the system to be measured [152]. We fabricate an SDD with an additional Cooper pair box (CPB) in close proximity to one of the SDD islands. For optimal sensitivity as a charge sensor, the CPB is tuned to the point at which its change in quantum capacitance (i.e. $\partial C_q / \partial V_{\text{rf}}$) is maximal. This is at the edge of a quantum capacitance peak [130].

4.3.1 Fabrication

The device fabricated for these measurements is made using a standard three angle shadow mask process (Chapter 3, section 3.1.3). Close to the SDD is a Cooper pair box (CPB), which acts as the charge sensor. Both devices are made in the same evaporation process, with an artefact of one of the SDD islands forming the CPB (An SEM of the device is shown on Fig. 4.5(a)). The evaporation process for this device is as follows:

1. Evaporate 25 nm of aluminium at an angle of $-22°$ to form the left dot of the SDD and the lead of the CPB.
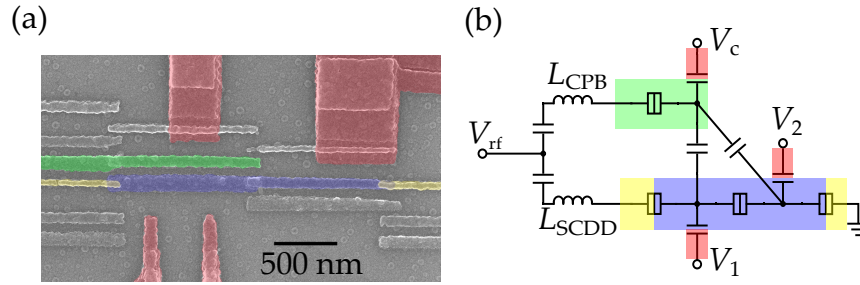
Figure 4.5: The superconducting double dot and Cooper pair box. (a) False colour electron micrograph of the device. The SDD is shown in blue, the CPB in green, and red regions are the electrostatic gates, Metallic leads are yellow. Other features are artefacts of the triple angle evaporation. (b) Schematic of the experiment. The rf signal is incident on resonant inductors L_{SDD} and L_{CPB}.

2. After waiting 10 minutes, peform controlled oxidation for 4 minutes at an O_2 pressure of 0.04 mbar.

3. Evaporate 15 nm of aluminium at an angle of $-8°$ to form the right dot of the SDD and the island of the CPB.

4. After waiting 10 minutes, perform controlled oxidation for 10 minutes at an O_2 pressure of 500 mbar.

5. Evaporate 30 nm of Al:Mn at an angle of $+22°$ to form the leads of the SDD.

The CPB island is chosen to be thinner (15 nm) than the lead (25 nm), which results in a larger Δ in the island than the lead [103]. This acts as an energy barrier to quasiparticles from the lead, protecting the CPB from quasiparticle poisoning [72]. The gate voltage V_c controls the electrochemical potential of the CPB island.

4.3.2 Experimental set-up

The leads of the SDD and CPB are bonded to separate LC circuits with resonant frequencies of f_{CPB} = 298 MHz and f_{SDD} = 350 MHz, so that the two devices can be probed independently. The charging energies of the two island of the SDD are determined from Coulomb diamonds to be ≈ 275 μeV. The mean value of Δ_0 of the two islands is 225 μeV. The thinner island is expected to have a larger Δ_0, but we cannot

discrimate between the two islands. The total resistance of the SDD is ≈ 1 MΩ. A circuit diagram of the set-up is shown in Fig. 4.5(b).

4.3.3 Quantum capacitance
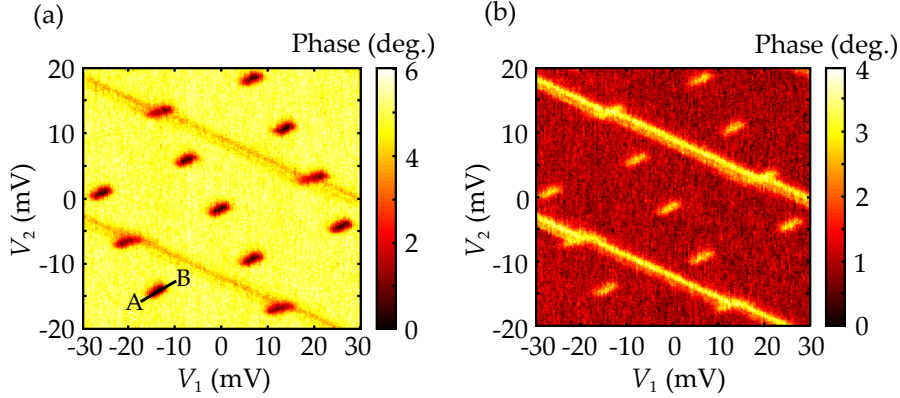
Figure 4.6: (a) Phase response at f_{SDD} as a function of V_1 and V_2 with V_c grounded, showing the quantum capacitance of the SDD. A smaller response due to the quantum capacitance from the CPB is visible. The line A → B shows the cross section used in Fig. 4.7. (b) Phase response at f_{CPB} as a function of V_1 and V_2 with V_c grounded. Here the CPB dominates the response, and the signal from the SDD is reduced.

In Figs. 4.6 (a) and (b), we show the phase response (averaged over 400 gate sweeps) of the SDD and the CPB as a function of V_1 and V_2 with V_c grounded. The regular pattern of ellipses is the quantum capacitance signal from the SDD, corresponding to the anticrossings between even charge states mediated by the transfer between the islands. The diagonal lines are due to the quantum capacitance near the charge transitions of the CPB. These diagonal lines coincidentally intersect the SDD quantum capacitance features. The same features are observed in both plots because the devices are capacitatively coupled to each other. The visibility of the feature associated with each device is enhanced when that device is probed directly. The fact that we can observe quantum capacitance due to the anticrossings means that the device is either in the regime in Fig 4.2 (c) or (d), i.e. $\tilde{\Delta}/(E_C - E_J) > 1/2$.

We analyse the quantum capacitance of the SDD in the antidiagonal ε direction. In these measurements, we use V_c to compensate for the action of V_1 and V_2 on the charge sensor, keeping the CPB at a fixed charge state so that the SDD is not affected.

The capacitance change is calculated from the phase shift of the SDD tank circuit. We plot the normalised capacitance with varying temperature, T (Fig. 4.7(a)), and observe that the magnitude of the capacitance shift decreases with increasing T. Here, a normalised capacitance of 1 is the capacitance for a blockaded state (i.e. in the centre of a charge stability hexagon). We observe a similar effect in increasing in-plane magnetic field, B. (Fig. 4.7(b)). In both of these cases, the free energy of the quasiparticle states decreases with increasing B and T. We model the thermal occupancy of the charge states, given by the Boltzmann distribution [153], and calculate the expected quantum capacitance. The thermal occupancy of a state i is

$$p_i = \frac{e^{\frac{F_i}{k_B T}}}{\sum_i e^{\frac{F_i}{k_B T}}}, \tag{4.4}$$

where F_i the free energy of state i (Chapter 2, Section 4.3).

We assume a lower bound for the electron temperature of 75 mK. The symmetric Cooper pair state $|G\rangle$ has a positive quantum capacitance and the antisymmetric Cooper pair state $|E\rangle$ as a negative quantum capacitance (Chapter 2, section 2.4). All other charge states have zero quantum capactiance. The antisymmetric Cooper pair state has negligible occupation in these measurements due to the short T_1 lifetime ($\sim$ 7 ns, see Chapter 6, section 6.2). The expected normalised capacitance signals are plotted in Figs. 4.7 (c) and (d). The free energy of the odd parity states decrease with temperature and magnetic field. In the case of increasing temperature, the thermal occupancy of the higher energy charge states increase, explaining the difference in dependency between capacitance vs. T and capacitance vs B.

This model agrees qualitatively with the measurements. However, the heavily averaged measurements lead to broadening in the quantum capacitance signal, due to $1/f$ charge noise from background two-level fluctuators (e.g. impurities in the SiO_2 substrate) [129]. The effect of this broadening is not included in our model.

4.3.4 Charge sensing

The quantum capacitance data shows that the SDD device is in one of the two regimes shown in Figs. 4.2 (c) and (d), in which the anticrossings are visible. To verify these conclusions, we measure the charge state of the SDD using the CPB charge sensor. We now set V_c to keep the CPB near a charge transition, where it is most sensitive as a charge sensor. In Fig. 4.8 (a) we show the phase response of L_{CPB} as a function of V_1
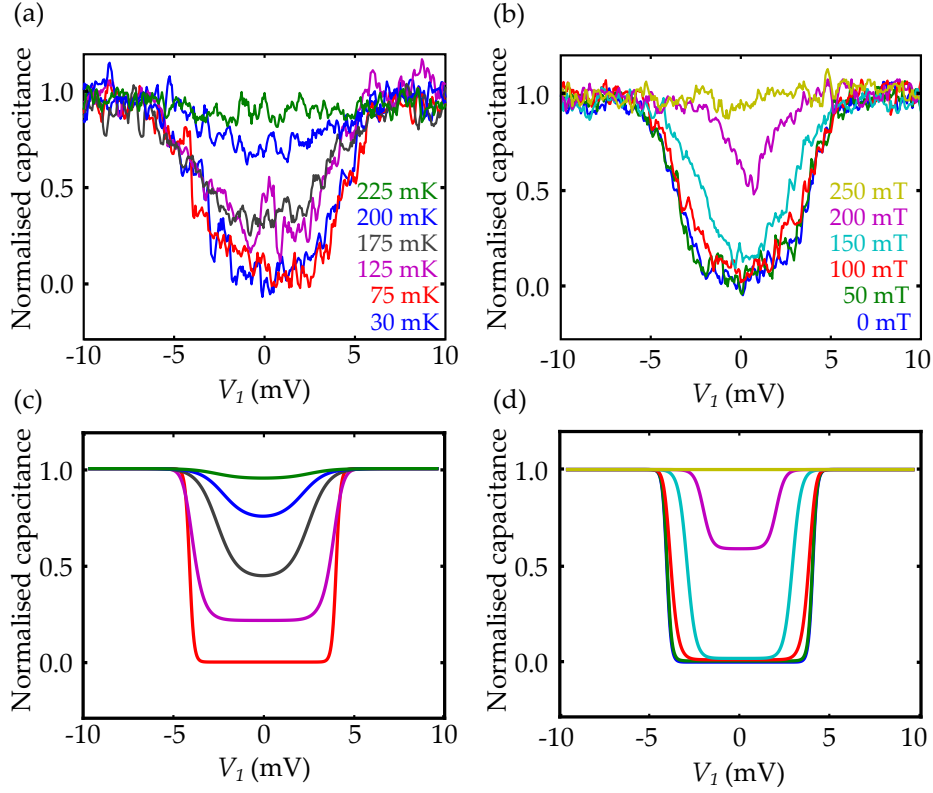
Figure 4.7: Quantum capacitance plots along the line A → B in Fig. 4.6. (a) Normalised capacitance at different temperatures with $B = 0$. (b) Normalised capacitance with different in-plane magnetic fields at base temperature. In (a) and (b) V_c is used to compensate for the action of V_1 and V_2, holding the CPB in a single charge state. (c) Calculated normalised device capacitance weighted by state occupancy for the temperatures measured in (a). We assume a base electron temperature of 75 mK, so no curve is plotted for 30 mK. (d) Calculated normalised device capacitance weighted by state occupancy for the magnetic fields measured in (b).

and V_2. We observe a hexagonal stability diagram, characteristic of electrostatically coupled double dots (Chapter 2, Section 2.2.6). By comparing the gate periodicity with the normal state stability diagram measured at $B \approx 2$ T we find that it is $2e$ periodic. We also observe here the quantum capacitance of the SDD at the inter-island charge transitions, as in Fig. 4.6(b).

In Fig. 4.8(b) we show the phase along the line C → D, as marked in Fig. 4.8(a) for applied magnetic field values between 0 mT and 100 mT. In this part of the stability diagram, the CPB is tuned such that $(0, 0)$ and $(0, 2)$ give similar signals in order
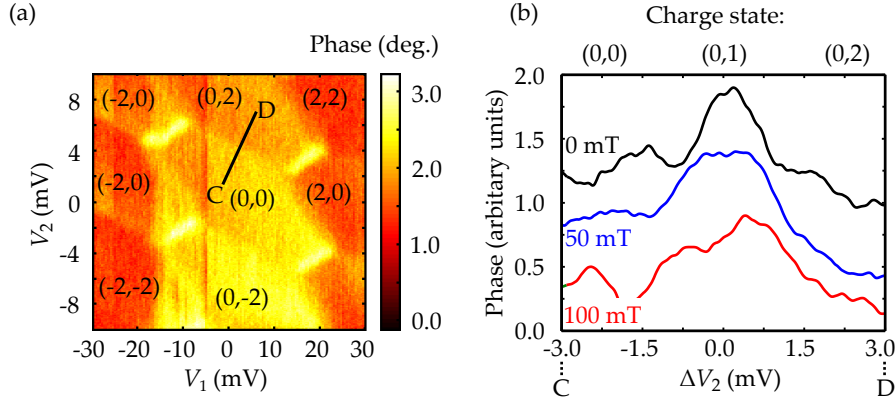
Figure 4.8: Charge sensing. (a) Phase response at f_{CPB} with V_c acting to hold the CPB close to a charge transition, and $B = 0$. A honeycomb charge stability pattern is observed, with a background phase gradient due to the imperfect compensation of the action of V_1 and V_2 by V_c. (b) Normalised phase response at f_{CPB} along C $\rightarrow$ D, for increasing magnetic fields. As field increases, the central plateau corresponding to the $(0,1)$ charge cell increases in width (observed around $\Delta V_2 = 0$).

to maximise the contrast with the $(0, 1)$ state, which is observed between the $(0, 0)$ and $(0, 2)$ states. This confirms that this device is in the regime shown in Fig 1c at $B = 0$ i.e. $1/2 < \tilde{\Delta}/(E_C) < 3/2$. As B increases, $\tilde{\Delta}$ decrease, and the odd parity $(0,1)$ state increases in size, although most of the stability diagram is still even parity. At 150 mT and higher, the quantum capacitance signal of the CPB is suppressed due to quasiparticle excitations (like that observed in the SDD), and it can no longer be used as a charge sensor.

4.3.5 Limitations to the CPB charge sensor

The limiting factor of this experiment is that when $B > 150$ mT, the Cooper pair box no longer operates as a charge sensor. A normal state rf SET electrometer would operate at higher magnetic fields. This would allow charge sensing in the regime $\tilde{\Delta}/(E_C - E_J) > 1/2$ in which the $(1,1)$ state, where a single quasiparticle is present in both islands, can be detected. Fabricating such an electrometer in the proximity of the SDD would require a second electron beam lithography step with a high precision alignment (to the order of 100 nm).

4.4 Conclusions

We have studied the energetics and charge stability diagram of the superconducting double dot (SDD) and have presented experimental results which support the overall model. The behaviour of the SDD depends on the competition between the charging energies and the superconducting energy gap. Measurements of quantum capacitance reveal an anticrossing between Cooper pair states, and charge sensing measurements show the presence of single quasiparticle states.

In the next two chapters, we use these results to explain how Cooper pairs in the SDD can be broken into their constituent quasiparticles via microwave radiation. Furthermore, in Chapter 7, we will see how the energetics of the SDD change when the double dot system is galvanically isolated.

4.5 Summary

- The superconducting double dot (SDD) is a nanoscale device consisting of two superconducting islands each connected to normal lead and coupled to each other via a Josephson junction.
- The physics of the SDD involves the parity effect, like that observed in superconducting charge devices, and charge stability diagrams, like that observed in semiconductor double quantum dots.
- We calculate the energy landscape and charge stability diagram for four different regimes of the SDD defined by Δ/E_C.
- We carry out an experiment in order to verify the charge state model. We fabricate an SDD coupled to an RF circuit to detect changes in device impedance, and to a Cooper pair box to act as a charge sensor.
- We detect the anticrossings of the Cooper pair states in the SDD via quantum capacitance. We model the capacitance shift with varying magnetic field and temperature. We also observe single quasiparticle states via charge sensing.

BREAKING SINGLE COOPER PAIRS WITH

MICROWAVE LIGHT

In the previous Chapter we discussed the energy landscape of the superconducting double dot (SDD), and its dependency on the relative magnitudes of the superconducting gap Δ and the charging energies of the islands E_C. Degeneracies between Cooper pair states in the SDD were found by measuring its quantum capacitance.

In this Chapter, we investigate the time dependence of the quantum capacitance of the SDD, and find that it stochastically switches between two values. We analyse the rates of the switching and conclude that this results from stray photons exciting the SDD from the symmetric Cooper pair state, $|G\rangle = \frac{1}{\sqrt{2}}(|2,0\rangle + |0,2\rangle)$, to a "broken" pair band of states, $(1,1)$, in which there is an unpaired quasiparticle in each island. We observe the continuous breaking and recombining of Cooper pairs and measure the rates as functions of in-plane magnetic field and temperature. We then apply microwaves and observe a linear increase in breaking rate with incident power. We then discuss the potential of the SDD device as a single microwave photon detector.

The experimental work presented in this chapter was done in collaboration with Dr Nicholas Lambert and Dr Megan Edwards, and the theoretical modelling was done in collaboration with Dr Felix Pollock. This work is published over two papers in Physics

Review B [1, 3].

5.1 Device fabrication and parameters

The SDD for this experiment (Fig. 5.1) is fabricated using a triple angle shadow evaporation process (see Chapter 3, section 3.1.3). The tunnel junctions are formed by controlled oxidation for four minutes at an O_2 pressure of 0.04 mbar for the inter-island Josephson junction, and 10 minutes at 500 mbar for the tunnel barriers to the leads. The inter-island normal state resistance is ≈ 8.5 kΩ, and the NIS junction resistances are chosen to be ≈ 5 MΩ to suppress quasiparticle poisoning from the leads.

Microwave excitations are driven by an Anritsu microwave source[a] via an additional gate electrode (coloured in red in Fig. 5.1). The source lead is bonded to a resonant LC circuit consisting of a surface mount inductor ($L = 510$ nH) and parasitic capacitance to ground ($C_p = 0.41$ pF). We apply an RF signal at the circuit's resonant frequency ($f = 349$ MHz) of low power (≤ -95 dBm) for the purpose of RF reflectometry (Fig. 5.1). An on-board bias-tee allows a dc bias to be applied to the source.

5.2 Charge stability diagram

We measure the average phase of the reflected RF signal as a function of the gate voltages V_1 and V_2. At $B = 0$, the SDD is in the superconducting state (Fig. 5.2(a)). The phase maxima appear due to the quantum capacitance of the SDD, corresponding to the anticrossings between charge states in which a Cooper pair coherently tunnels between the islands (Chapter 4, section 4.3.3). The capacitance shift δC is calculated from the phase shift using Eqn. 3.7 (Chapter 3, section 3.3.2). We define $\delta C = 0$ as the capacitance shift for the blockaded case, e.g. in the middle of the (0,0) hexagon.

The phase shift for all of the charge states is plotted against the antidiagonal detuning ε in Fig. 5.3(b) . The maximum capacitance shift is at the anticrossing centre ($\delta = \epsilon = 0$) and is $\delta C = 0.5$ fF for $|G\rangle$, $\delta C = -0.5$ fF for $|E\rangle$ and $\delta C = 0$ for all other charge states.

_____

[a] Anritsu MG3964C

(a)

(b)
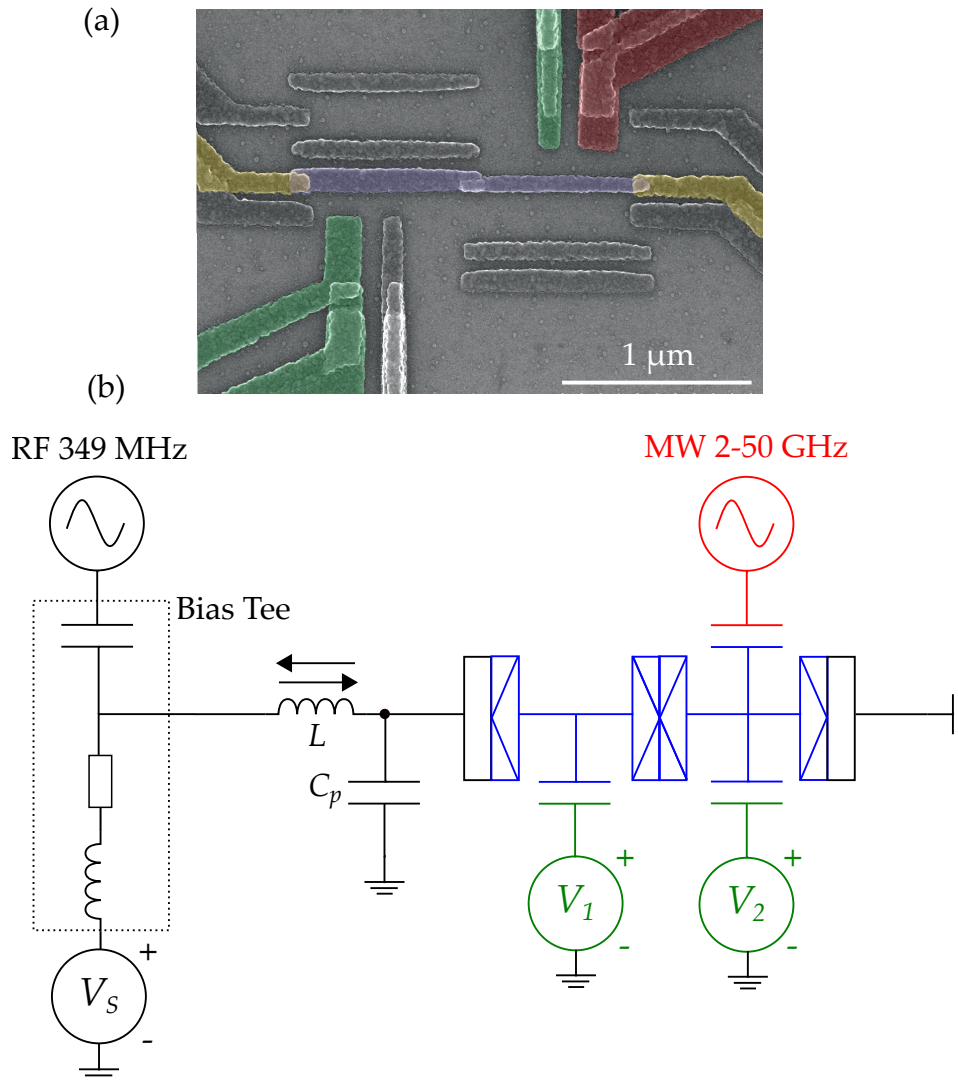
Figure 5.1: (a) Scanning electron micrograph of the superconducting double dot (SDD) device. The false colour regions show the dc gates (green), microwave agte (red), the source and drain contacts (yellow) and the islands (blue). Uncoloured metal regions are the artefacts of the triple angle evaporation process (b) Schematic diagram of the SDD device embedded in a lumped element LC resonant circuit, with $L = 510$ nH and $C_p = 0.41$ pF. The circuit resonates at 349 MHz with a loaded Q factor of ≈ 50. Other electronic components in the experimental setup are shown in Fig. 3.8 in Chapter 3, section 3.3.
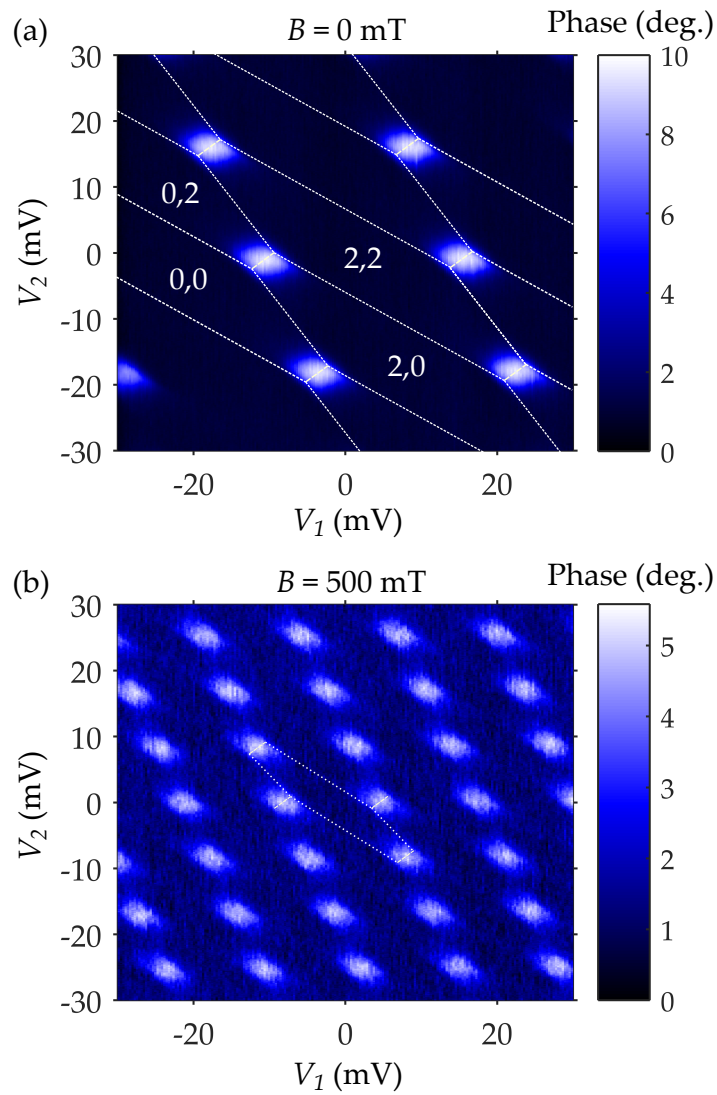
Figure 5.2: Charge stability diagrams. (a) Phase shift (400 averages) as a function of the dc control gates (V_1, V_2) at $B = 0$, with the charge stability diagram highlighted (dotted white lines). Charge states are shown, with (0,0) chosen arbitrarily. (b) Average phase shift at $B = 500$ mT, with one cell of the charge stability diagram highlighted.

We verify that this is 2e-periodic by measuring the average reflected phase with the SDD in the normal state, at $B = 500$ mT, and observe the periodicity of the maxima halve (Fig. 5.2(b)). This response is the result of an effective impedance, known as the Sisyphus impedance, as explained in Chapter 3, section 3.3.7. We find that this normal state charge stability appears at $B = 320$ mT - we determine that this is the superconducting critical field of the device.

We use the normal state charge stability diagram to extract the gate capacitances, and measure bias triangles (by applying $V_S = 100$ μV bias) to extract the junction capacitances (Chapter 2, section 2.2.5.5). We use these capacitances to calculate the charging energies $E_{C1} = 314$ μeV, $E_{C2} = 227$ μeV and $E_{Cm} = 88$ μeV. The Josephson energy of the middle tunnel junction is $E_J = 110 \pm 10$ μeV, determined by microwave spectroscopy (see Chapter 6, section 6.1). The superconducting gap as a function of B is found by measuring Coulomb diamonds, and at $B = 0$ and a temperature of 35 mK, $\tilde{\Delta} = 250$ μeV.

5.3 Observation of capacitance switching

In the presence of a magnetic field, the average quantum capacitance signal at the (0,2)/(2,0) degeneracy is reduced, and at $B = 175$ mT the phase shift is close to zero (Fig. 5.4(a)&(b)). To investigate this effect further, we measure the time dependence of the phase at a Cooper pair degeneracy point ($\delta = \varepsilon = 0$). For both zero and finite magnetic field, we observe an asymmetric random telegraph signal (RTS) indicative of stochastic switching between the ground state ($\delta C = 0.5$ fF) and another charge state with ($\delta C = 0$). We see that in the case of $B = 180$ mT, $\delta C = 0$ for the majority of the time. We do not attribute the switching to transitions to and from the excited Cooper pair state $|E\rangle$ ($\delta C = -0.5$ fF), as the measured relaxation time of the state is ~ 7 ns (Chapter 6, section 6.2), which is shorter than the measurement bandwidth.

The switching rates from ($\Gamma_{G\rightarrow}$) and to ($\Gamma_{\rightarrow G}$) the ground state are extracted by analysis of the random telegraph signals (see section 3.4). We take 10 second traces consisting of 10^6 data points, which is enough points to ensure a good fit to the histogram.
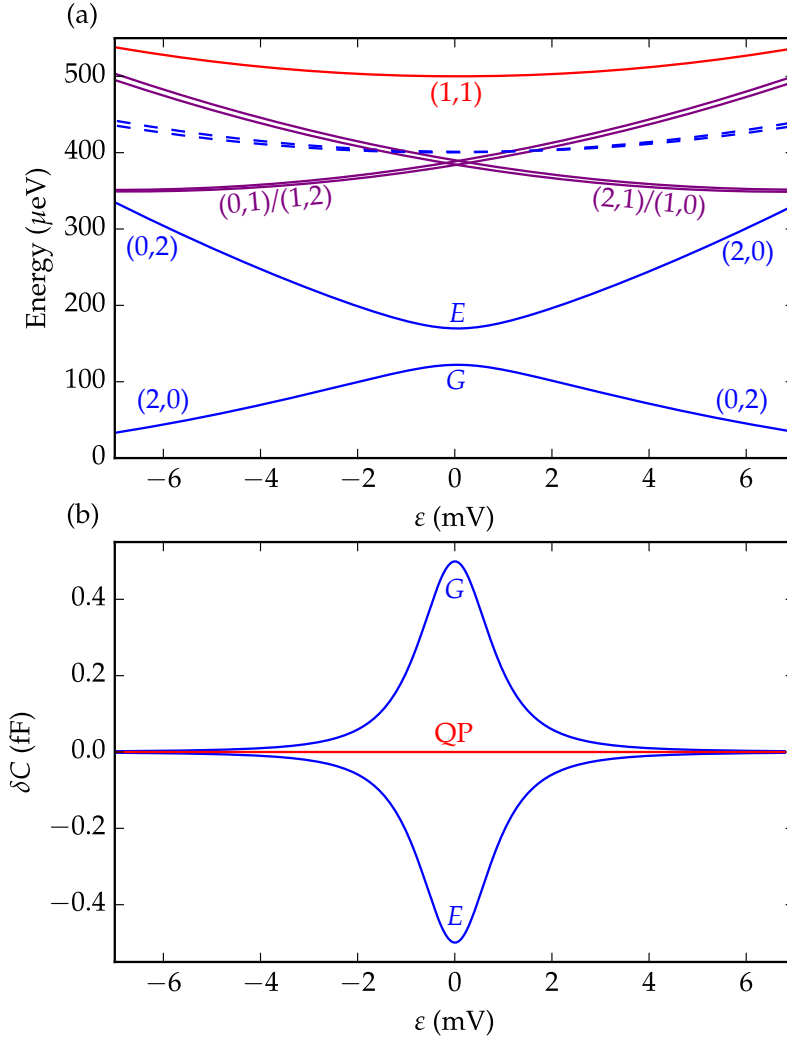
Figure 5.3: (a) Calculated energies of the charge states of the SDD as a function of ε detuning, using experimentally determined device parameters. (b) Calculated capacitance shift δC as a function of ε detuning for the ground $|G\rangle$ and the excited $|E\rangle$ Cooper pair states and the quasiparticle bands.

5.3.1 Possible excitations from $|G\rangle$

There are three different kinds of excitations from the ground state of the SDD. These transitions result in the same capacitance shift and cannot be directly distinguished in our measurement setup. We calculate the theoretical rates for each process and compare the sum of the modelled rates with the measured rates to determine which
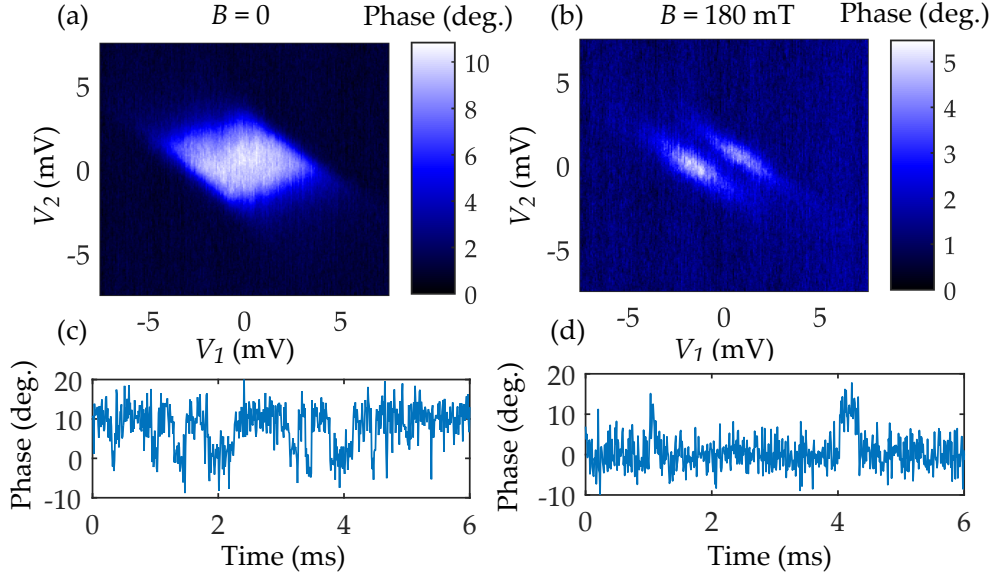
Figure 5.4: (a) & (b) Zoom-in of a single phase (capacitance) peak showing the region around a single anti-crossing, for 0 mT and 180 mT. (c) & (d) Time domain measurements of phase for fixed gate voltages for 0 mT and 180 mT, taken at $\delta = \varepsilon = 0$.

processes dominate.

$|G\rangle \rightarrow$ (1,1): Cooper pair breaking

It is possible for the SDD to be excited from its ground state $|G\rangle$ to the (1,1) state. A photon or phonon with energy $hf \geq E_{(1,1)} - E_G \equiv E_{(1,1)-G}$ is absorbed by the SDD and splits the excess Cooper pair in the left dot into two quasiparticle excitations. One of the quasiparticles tunnels to the neighbouring dot via the Josephson junctions and the SDD is now in the (1,1) state.

The rate of pair breaking is proportional to the number of photons or phonons which are able to break a Cooper pair. The thermal energy associated with the SDD $k_B T \ll E_{(1,1)-G}$, so the number of thermal phonons and photons that are able to break pairs is close to zero. Any breaking observed without the presence of a microwave drive will be due to non-equilibrium photons from some noise source.

The rate is also strongly dependent on the energy separation $E_{(1,1)-G}$: for a given photon energy hf, the number of available (1,1) states increases as $E_{(1,1)-G}$ decreases. As $E_{(1,1)-G}$ is constant with the diagonal detuning parameter, δ, we expect $\Gamma_{G \rightarrow (1,1)}$ to be constant with δ.

$|G\rangle \rightarrow$ (0,1), (1,0), (2,1), (1,2): Single quasiparticle tunnelling

These transitions correspond to a single quasiparticle excitation, where a quasiparticle tunnels into or out of one of the dots from the leads. The rate of tunnelling is like that for a NIS-junction where the effective bias is the energy difference between the charge states [106]. The rate is proportional to the bias and inversely proportional to the resistance of the junction. We use the expressions given in Ref. [94].

$|G\rangle \rightarrow$ (0,0), (2,2): Andreev reflection

These transitions correspond to the addition (or removal) of a Cooper pair to (from) one of the superconducting dots. This occurs via Andreev reflection: a electron in the normal lead tunnels into the superconducting dot, and at the normal-superconducting interface the electron is reflected as a hole and, to conserve charge, a Cooper pair is transmitted on the superconducting side [11]. The reverse process may also happen, and is known as an "inverse Andreev reflection". The rates for these processes are derived following a nonlinear response approach, using expressions from Refs. [65] and [154].

5.3.2   Proof of Cooper pair breaking ($|G\rangle \rightarrow$ (1,1))

We measure $\Gamma_{G\rightarrow}$ as a function of diagonal detuning δ (Fig. 5.5(b)), and compare with the calculated rates (Fig. 5.5(c)) using our theoretical model with the calculated charge state energies shown in Fig. 5.5(a). The measured rate is constant in the region near $\delta = 0$ and for larger values of $|\delta|$ increases exponentially with $|\delta|$ until it reaches the bandwidth limit.

We plot the theoretical rates in Fig. 5.5(c), choosing a temperature of 125 mK for these calculations, as we find this to be a good estimate of the electron temperature (Section 5.4.4). When the rates are summed, they agree qualitatively with the experimental data as long as the breaking rate term $\Gamma_{G\rightarrow(1,1)}$ is added. Only the breaking process occurs in the flat region, with the rates of other processes vanishing to zero. At larger detunings of δ, the model indicates that the dominant excitation process is Andreev reflection from/to the leads.

In conclusion, for small δ detunings from the SDD degeneracy point, only the process $|G\rangle \rightarrow (1, 1)$ is responsible for the switching. For the rest of the measurements,

we keep $\delta = \varepsilon = 0$ (unless otherwise stated) and attribute the measured rate $\Gamma_{G\rightarrow}$ to the single Cooper pair breaking rate.

5.4 Mechanisms of pair breaking and recombination

5.4.1 Origin of pair breaking

We have demonstrated that the capacitance switching at the Cooper pair degeneracy point of the SDD is caused by the stochastic breaking of a single Cooper pair, generating two quasiparticles in each dot, followed by the recombination of the two quasiparticles to go back to the initial state.

As discussed in section 5.3.1, pair breaking can only occur if the SDD absorbs a photon from the environment. With no applied microwave signal, the photons which cause pair breaking must come from some thermal noise source.

We plot the breaking rate with in-plane magnetic field, B (Fig. 5.6(a)), and observe that the rate increases with B. As B is increased, it suppresses $\tilde{\Delta}$ and the energy separation between the (1,1) and $|G\rangle$ states, $E_{(1,1)-G}$. More photons in the environment will have sufficient energy to excite the SDD to the (1,1) state, resulting in an increase of the breaking rate.

We can use this data to perform spectroscopy on the pair breaking photons and extract a temperature and find a possible source for the stray radiation.

5.4.2 Probing of ambient photon environment

We make the approximation that only photons with energy $hf \geq E_{(1,1)-G}$ are able to break Cooper pairs (i.e. we only consider single photon excitation). Thus

$$\Gamma_{G\rightarrow} \propto \int_{E_{(1,1)-G}}^{\infty} D_{\gamma}(E) dE, \tag{5.1}$$

where $D_{\gamma}(E)$ is the photon density of states. Assuming that the radiation is from a black-body, $D_{\gamma}(E)$ is given by the Planck distribution [155]:

$$D_{\gamma}(E) = \left(e^{\frac{E}{k_B T_{BB}}} - 1 \right)^{-1}. \tag{5.2}$$
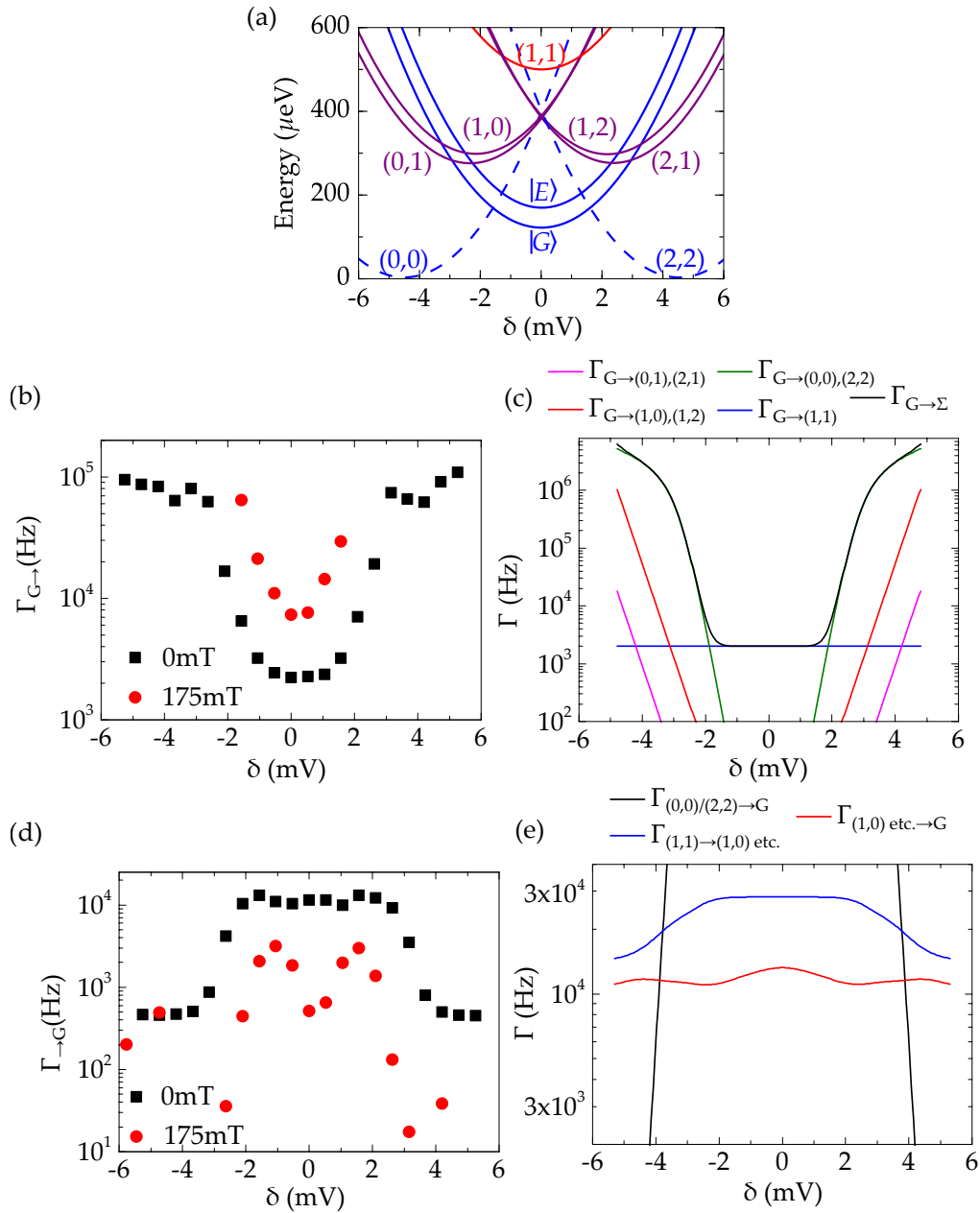
Figure 5.5: Pair breaking and recombination rates as a function of diagonal voltage detuning, δ. (a) Energies of SDD charge states as a function of δ. The energy difference between $(1,1)$ and G is constant along this axis. (b) Measured switching rate from ground state as a function of δ. (c) Calculated rates for various transitions from the ground state. Sum of the rates shown in black. (d) Measured switching rate to the ground state as a function of δ, with the total rate $\Gamma_{G\to\Sigma}$ shown in black. (e) Calculated rates for various transitions to the ground state.

(a)

(b)
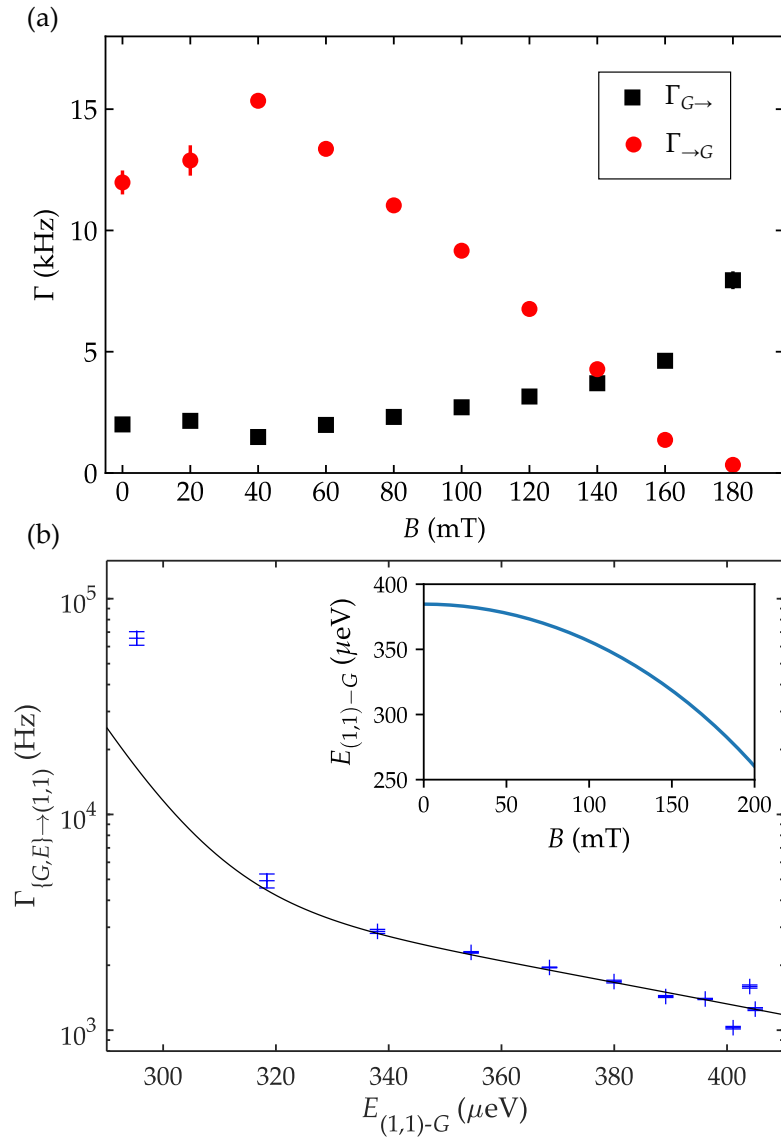
Figure 5.6: (a) The pair splitting ($\Gamma_{G\rightarrow}$) and recombination ($\Gamma_{\rightarrow G}$) rates as functions of magnetic field, B, at T = 35 mK. (b) $\Gamma_{G\rightarrow}$ as a function of the minimum excitation energy $E_{(1,1)-G}$. Inset: $E_{(1,1)-G}$ as a function of B. Error bars are the error in the fit to the histogram.

We convert the data from the rate $\Gamma_{G\rightarrow}$ against magnetic field (Fig. 5.6(a)) to $\Gamma_{G\rightarrow}$ against excitation energy $E_{(1,1)-G}$ (Fig. 5.6(b)) and fit an integrated Planck spectrum in Eqn. 5.1 to extract a black-body temperature, T_{BB}. The data fits well for $B < 200$ mT. Above this field, the rate sharply increases above this trend, due to processes other than $G \rightarrow (1,1)$ become important at $\varepsilon = 0$. The fitted black-body temperature is $T_{BB} = 542 \pm 5$ mK, which most likely comes from Johnson-Nyquist noise from the 20 dB attenuator on the microwave line at ~ 1.4 K, subsequently attenuated by a factor of two by the 3 dB attenuator at the mixing chamber [16].

This demonstrates that the SDD can be used to probe its environment and provide an understanding of the source of pair breaking photons.

5.4.3   Recombination
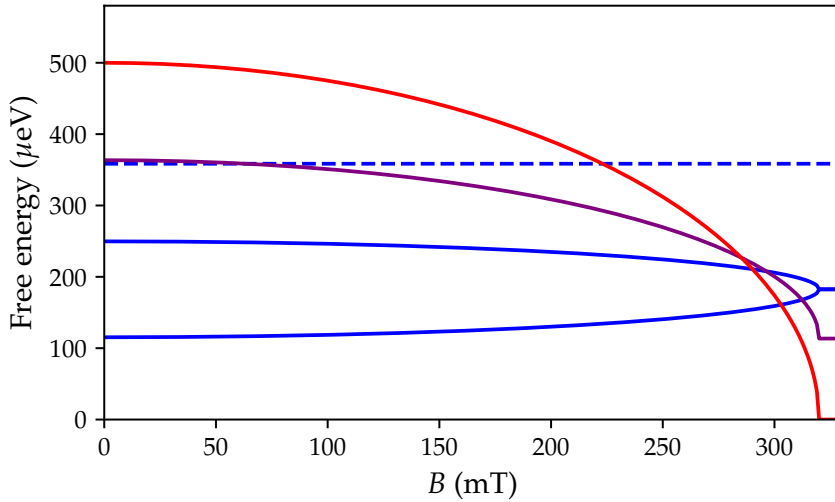
Figure 5.7: The free energies of the charge states at $\delta = \varepsilon = 0$ as a function of magnetic field, B. The intersection between the (1,0) and (0,0) states is marked with an arrow.

State relaxation in the SDD from (1,1) to $|G\rangle$ occurs via quasiparticle recombination. The quasiparticles can recombine directly from the (1,1) state, or indirectly via quasiparticle tunnelling to intermediate charge states. From Wilson et al. [105], the average rate of direct recombination between two quasiparticles within a volume of that of the SDD ($V \approx 4 \times 10^3 \mu m^3$) is

$$\Gamma_{\mathrm{rec}} = \frac{4\Delta_0^2}{N_0 V \tau_0 (k_B T_c)},$$ (5.3)

where N_0 is the single spin normal density of states at the Fermi energy, which for aluminium is $1.72 \times 10^{10} \, \mu m^{-3}$. τ_0 is the electron-phonon coupling constant (458 ns for aluminum) [16]. We calculate $\Gamma_{rec} \approx 5$ kHz. The equivalent process in the SDD, $(1,1) \rightarrow |G\rangle$, will be lower than this, as there is a tunnel junction which spatially separates the quasiparticles. This rate is lower than recombination process via the leads: $(1,1) \rightarrow (1,0)/(0,1)/(1,2)/(2,1) \rightarrow$ or $(1,1) \rightarrow |G\rangle$ $(1,0)/(0,1)/(1,2)/(2,1) \rightarrow (0,0),(2,2) \rightarrow |G\rangle$. The theoretical rates of these processes as a function of δ (Fig. 5.5(e)) qualitatively agree with the measured recombination rates (Fig. 5.5(d)).

As the magnetic field increases, $\Gamma_{\rightarrow G}$ is approximately constant until $B = 75 \pm 25$ mT, when it begins to decrease. This is because the $(1,0)$ odd state is now lower in energy than the $(0,0)$ even state (Fig. 5.7). After one quasiparticle is ejected from the leads $((1,1) \rightarrow (1,0))$ the SDD is trapped in the $(1,0)$ state until it is released by thermally activated tunnelling $((1,0) \rightarrow (0,0))$. As B increases, the thermal barrier between $(1,0)$ and $(0,0)$ increases, resulting in a slower relaxation to $|G\rangle$. For $B > 150$ mT, the breaking rate exceeds the recombination rate, and the time-averaged population of the $(1,1)$ state becomes higher than that of the Cooper pair state $|G\rangle$.

5.4.4 Temperature dependence of rates
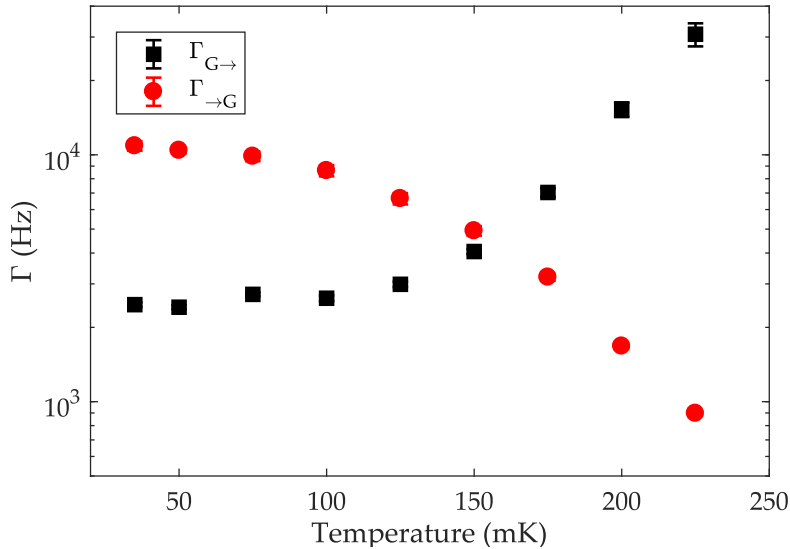
Figure 5.8: The temperature dependence of the pair splitting ($\Gamma_{G\rightarrow}$) and recombination ($\Gamma_{\rightarrow G}$) rates at $B = 0$. Error bars are the error in the fit to the histogram.

A plot of the temperature dependence of rates $\Gamma_{G\rightarrow}$ and $\Gamma_{\rightarrow G}$ is shown in Fig 5.8. $\Gamma_{G\rightarrow}$ is approximately constant until a temperature of approximately 125 mK, after which it rapidly increases with increasing temperature, and $\Gamma_{\rightarrow G}$ decreases with increasing temperature. This is due to the suppression of $\tilde{\Delta}$, lowering the free energy of the quasiparticle states, similar to the effect of increasing the magnetic field. We interpret $T = 125$ mK as the base electron temperature of the SDD, which is higher than the temperature of the mixing chamber (35 mK) due to imperfect shielding and filtering [13, 155].

5.5 Driving pair breaking with microwave radiation

We now apply microwaves to the SDD via the microwave gate and measure breaking rate as a function of incident power. We measure with a range of frequencies (20 - 55 GHz) and find similar results. I present the data for 40 GHz in this thesis.

5.5.1 Results

$\Gamma_{G\rightarrow}$ increases linearly with microwave power, P (Fig. 5.9(a)). This suggests that a single photon process is responsible. The derivative $\frac{d\Gamma_{G\rightarrow}}{dP}$ is the change in the rate (i.e. the response of the SDD) with respect to the number of incident microwave photons per unit time. It therefore characterises the microwave sensitivity of the SDD.

Fig. 5.9(b) shows this variation of sensitivity with applied magnetic field, with a microwave frequency of 40 GHz. For low magnetic fields, the sensitivity is constant. As $E_{(1,1)-G}$ with increasing magnetic field, the density of states in the region within hf of the energy of state $|G\rangle$ increases and the sensitivity sharply increases as a result. The pair breaking rate due to electromagnetic radiation is given by

$$\Gamma_{G\rightarrow} \propto \int\limits_{0}^{hf+E_C/2} R_E D_S^D(E)\left(hf + \frac{E_C}{2} - E\right)dE. \tag{5.4}$$

Here, hf is the photon energy, $D_S^D(E)$ is the Dynes density of states (Chapter 2, section 2.1.5), R_E is the case II coherence factor corresponding to a perturbation that is odd under time reversal [11], and the additional term involving $E_C/2$ is due to the additional energy available from charge reconfiguration in the device.
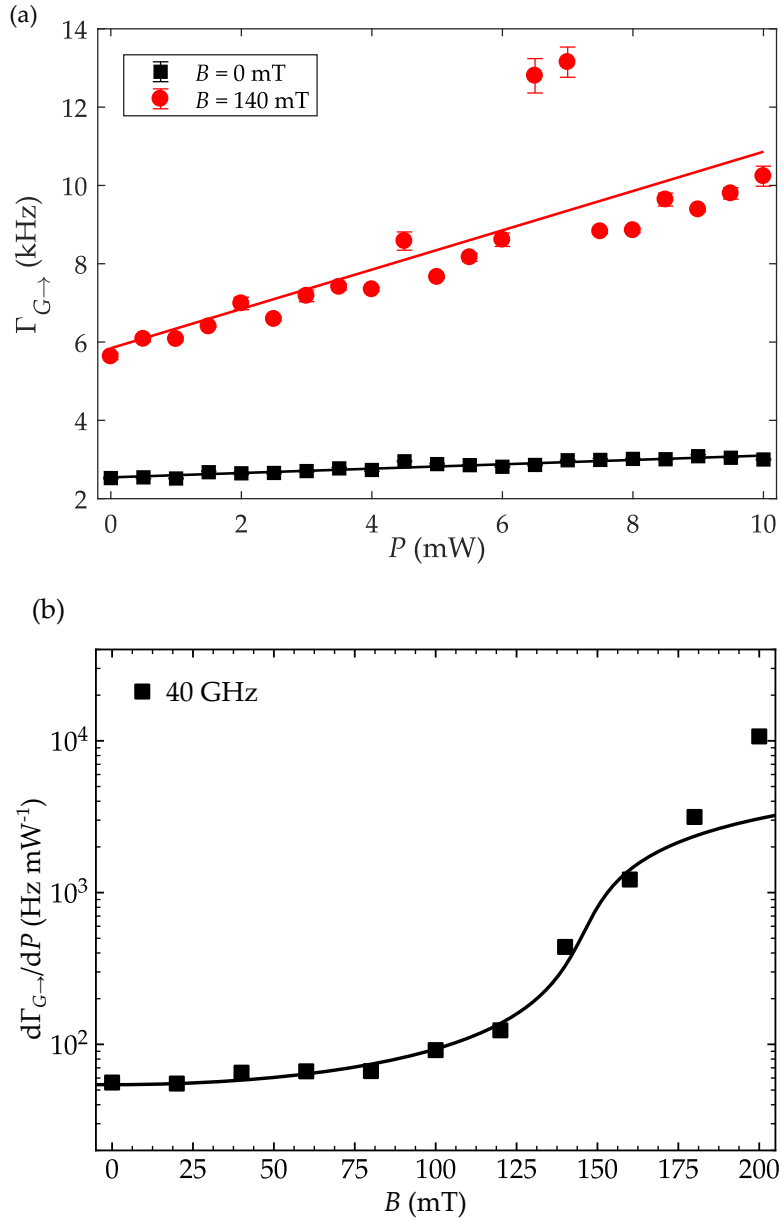
Figure 5.9: (a) The Cooper pair splitting rate as a function of microwave source power at a microwave frequency of 40 GHz for B = 0 mT (black) and 140 mT (red). (b) The gradient of splitting rate versus microwave power as a function of magnetic field for 40 GHz microwaves, with a fit to Eqn. 5.4. These measurements were taken at a mixing chamber temperature of 35 mK.

We fit the data to Eqn. 5.4 with Dynes broadening parameter $\gamma = 0.014$. As before, we neglect data at $B = 200$ mT. Our model replicated the above-exponential rate of increase of sensitivity well, and similar behavior is seen at 20, 25, 30, 35, 45 and 50 and 55 GHz [3].

5.5.2 SDD as a photon detector

These results show that the SDD can potentially be used as a broadband (20-55 GHz) detector for single microwave photons, with tunable sensitivity and detection bandwidth. The device acts as a passive 'click' detector, which switches its state when it absorbs a photon, and then resets to its original state to be ready for the next detection event. The key parameter for a single photon detector is the quantum efficiency. Other parameters include the dark count rate (detection of stray light) and the dead time (time taken between registering a count and resetting back to its detection state) [18].

In its current form, the SDD needs some optimization to become a practical single photon detector. The quantum efficiency is very low ($\sim 10^{-8}$), owing to the impedance mis-match between the SDD and the 50Ω microwave line. The impedance matching would be improved significantly by embedding the device inside a superconducting coplanar waveguide resonator. The quantum efficiency would increase by a factor of the Q of the resonator (typically $\sim 10^6$) [156]. The dark count, i.e. the minimum $\Gamma_{G\rightarrow}$ measured is 2 kHz, which could be improved with increased attenuation to reduce the Johnson-Nyquist noise. The reset time is limited by the recombination time $1/\Gamma_{\rightarrow G}$. This time can be shortened by using an active reset protocol, where after a detection event is recorded, the gate voltages are tuned to a region where the recombination time is maximal, and then tuned back to the operation point ($\delta = \varepsilon = 0$) to detect the next event.

Such a single microwave photon detector would have applications in quantum information processing where it could, for example, be used to measure the photon occupancy of a superconducting resonator, or to detect flying qubits between superconducting qubits. Efficient detection in the microwave regime is a challenging task due to the correspondingly low energy of microwave photons. Although, such a detector has been demonstrated recently using a superconducting flux qubit coupled to a resonator [157].

5.6 Summary

- We observe the breaking of single Cooper pairs in the SDD and retain the quasiparticles in separate dots. Recombination of the quasiparticles occurs via multiple tunnelling processes though the leads.
- Pair breaking and recombination rates are measured by analyses of random telegraph signals due to the stochastic switching of capacitance.
- We plot the pair breaking rate with the minimum energy for pair breaking, which fits well to an integrated Planck spectrum. We extract the blackbody temperature which reveals the most probable cause of pair breaking.
- The pair breaking rate is linearly proportional to the microwave incident power, suggesting that there is a single photon process involved. The microwave sensitivity of the SDD is measured with magnetic field, and fits well to a single photon excitation model up to $B = 200$ mT.
- The SDD has potential as a single microwave photon 'click' detector for use in quantum information processing.

STATE DEPENDENT BREAKING OF COOPER

PAIRS

In the previous chapter, I presented results demonstrating the breaking of single Cooper pairs in the SDD. An incident photon is absorbed by the device and causes an excitation from state $|G\rangle$, the ground Cooper pair state, to a continuum of states, (1,1), in which there is one quasiparticle in each dot. We measured the rates of breaking and recombination and observed a linear dependence on incident microwave power.

In this chapter, we now consider the excited Cooper pair state $|E\rangle$. At the operation point ($\delta = \varepsilon = 0$), $|E\rangle$ is E_J higher in energy than $|G\rangle$, where E_J is the Josephson energy. So far, we have not considered this state, as the occupancy at thermal equilibrium is zero. However, in this experiment, we use a Rabi pulse to prepare a significant population in $|E\rangle$ before driving the transition from $|E\rangle$ to the (1,1) band. When the system is in state $|E\rangle$, the energy required to reach the quasiparticle band edge is reduced by E_J, and we expect the excitation rate to be enhanced as a result. Hence, we have a Cooper pair breaking rate which is dependent on the initial quantum state of the SDD.

The results presented in this chapter were obtained in collaboration with Dr Nicholas Lambert and Dr Megan Edwards, and have been published in Physical Review B [3]. The device used for this experiment is the same as that described in

Chapter 5.

# 6.1 Measurement of the Josephson energy
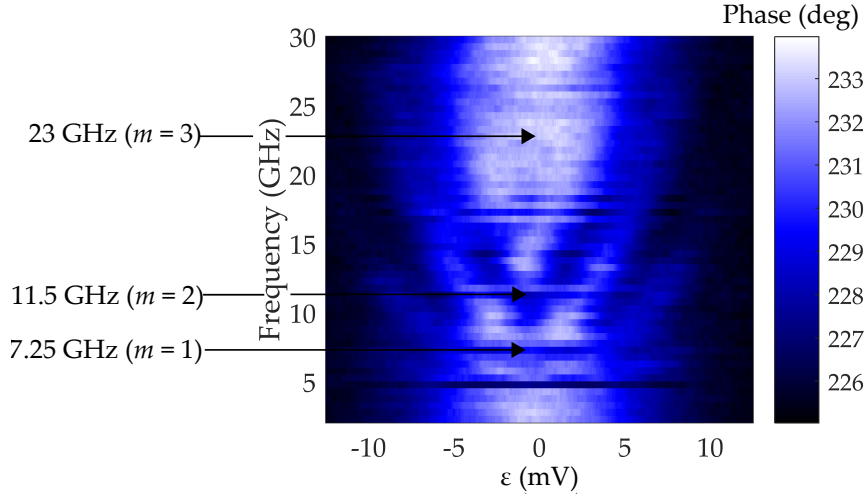
Figure 6.1: Measured phase along the ε axis as a function of applied microwave frequency. The phase shift due to the quantum capacitance of $|G\rangle$ is seen in the centre of the region (white). When the applied photons are resonant with the transition between $|G\rangle$ and $|E\rangle$, Rabi oscillations are driven, and the population weighted quantum capacitance of the two states is zero (black regions). Parabolic lines corresponding to two and three photons transitions are seen clearly.

We measure E_J by performing microwave spectroscopy of the two level system, $|G\rangle$ and $|E\rangle$. When the total energy of an integer number of photons, mhf, equals the energy separation, Rabi oscillations are driven between the two states. The quantum capacitance is a weighted average of those of the two states: $p_G \cdot \delta C_G + p_E \cdot \delta C_E$. We measure the phase shift due to quantum capacitance as a function of ε detuning and frequency of applied microwaves.

For a fixed source power, the microwave power transmitted to the device varies with frequency. This is because the microwave line acts as a transmission line with a frequency dependent impedance. We calibrate the power delivery by recording the power at source required to reduce the quantum capacitance signal by 50% for each frequency point.

From Fig. 6.1, we deduce $E_J \approx 23$ GHz. We observe transitions corresponding to two ($hf = 11.5$ GHz) and three ($hf = 7.25$ GHz) photons. The one photon transition is less clear, because the transmission response of the coaxial cables in the microwave line is small around 23 GHz. From $\Delta \approx 250\,\mu$eV and the Ambegoakar-Bartoff relation ($E_J = h\Delta/8e^2R$), we deduce a normal state resistance $R \approx 8.5$ kΩ for the Josephson junction.

6.2 Measurement of the relaxation time of $|E\rangle$
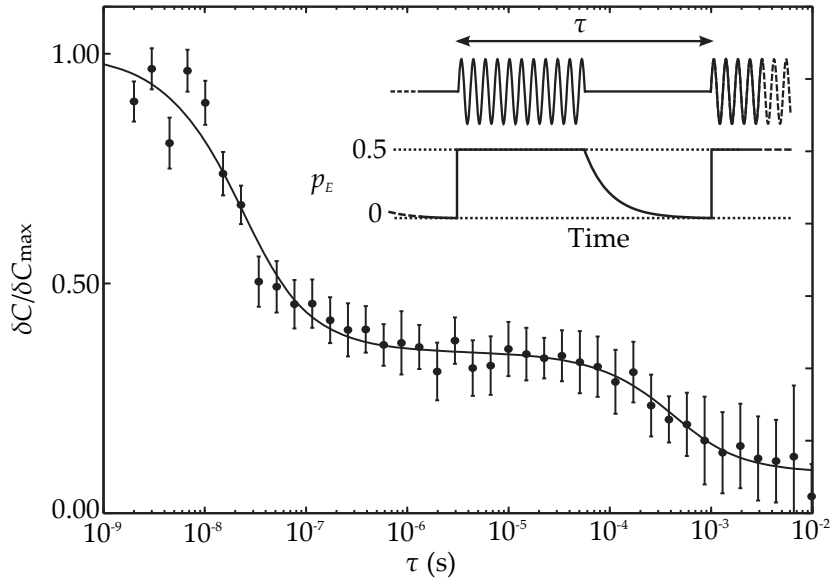
Figure 6.2: Normalised change in capacitance $\delta C(\tau)/\delta C_{\mathrm{max}}$ under symmetrically pulsed 11.5 GHz microwave excitation as a function of pulse period τ, with a fit to Eqn. 6.1. Inset: the pulse sequence and the probability of occupation of the excited state, p_E. Two relaxation times are observed; a fast relaxation of p_E with $T_1 = (6.8 \pm 1.0) \times 10^{-9}$ s, and a slower relaxation of p_{qp} with time constant $T_{\mathrm{qp}} = (1.2 \pm 0.4) \times 10^{-4}$ s [3].

We now probe the relaxation time T_1 of $|E\rangle$ at $\delta = \varepsilon = 0$. We proceed by saturating the transition with a microwave tone modulated by a symmetric square wave of period τ, with the use of an IQ modulator, and measure the time averaged quantum capacitance. The period of the Rabi oscillation of the system is much shorter than the relaxation time and so at the limit of $\tau \ll T_1$, the time averaged populations of the

105

states, p_G and p_E, are $p_G = p_E = 1/2$, and the measured quantum capacitance averages to zero. For longer τ, there is sufficient time for some decay in p_E to occur during the time that the microwave signal is off, and a finite quantum capacitance is measured [95].

We plot the averaged normalised change in capacitance under the modulated drive, as a function of τ. Two relaxation times can be seen, one at short time scales and one at much larger τ. We ascribe the short timescale behavior to relaxation on $|E\rangle$, and the long timescale dynamics to relaxation from a small population (p_{qp}) in the quasiparticle states. These states include the broken pair state, (1,1) and single quasiparticle states ((1,0) etc.) which are occupied during the recombination process[a]. The normalised capacitance[b] is therefore given by

$$\frac{\delta C}{\delta C_{max}} = \frac{1}{2} + \frac{p_E T_1}{\tau}(1 - e^{-\tau/(2T_1)}) + \frac{p_{qp} T_{qp}}{\tau}(1 - e^{-\tau/(2T_{qp})}), \qquad (6.1)$$

where T_{qp} is the relaxation time of the quasiparticle state. We fit Eqn. 6.1 to the data in Fig. 6.2, giving $T_1 = (6.8 \pm 1.0) \times 10^{-9}$ s. This is similar to T_1 times measured in Cooper pair box qubits in which charge noise and non-equilibrium quasiparticles limit the relaxation time ($T_1 \sim 7 - 10$ ns) and dephasing time [119, 120]. This is, however, much shorter than T_1 for charge states in optimised semiconductor double dots, due to the large dipole moment associated with the charge transitions between the ~ 1 μm islands, and the strong coupling between them. We find that $T_{qp} = (1.2 \pm 0.4) \times 10^{-4}$ s, which agrees with the recombination time $1/\Gamma$ at $B = 0, T = 35$ mK, as measured from random telegraph signals in Chapter 5, Fig. 5.6(a).

6.3 Experimental set-up for two-tone microwave pulses

The experiment is set up for radio frequency reflectometry, as discussed in Chapter 3, section 3.3, with the addition of two microwave sources connected to the microwave gate (Fig. 6.4). An Anritsu MG3694C signal generator (2 - 40 GHz) is used to drive the transition between $|G\rangle$ and $|E\rangle$ (we call this the Rabi tone). An Anritsu MG3697C signal generator (2-67 GHz) is used excite the SDD from the Cooper pair levels to

---

[a] We recall in Chapter 5, section 5.4.3 that at certain magnetic fields the SDD is trapped in the (1,0), therefore this state may have a finite occupation.

[b] This is also equal to the normalised phase shift $\delta\Phi/\delta\Phi_{max}$.
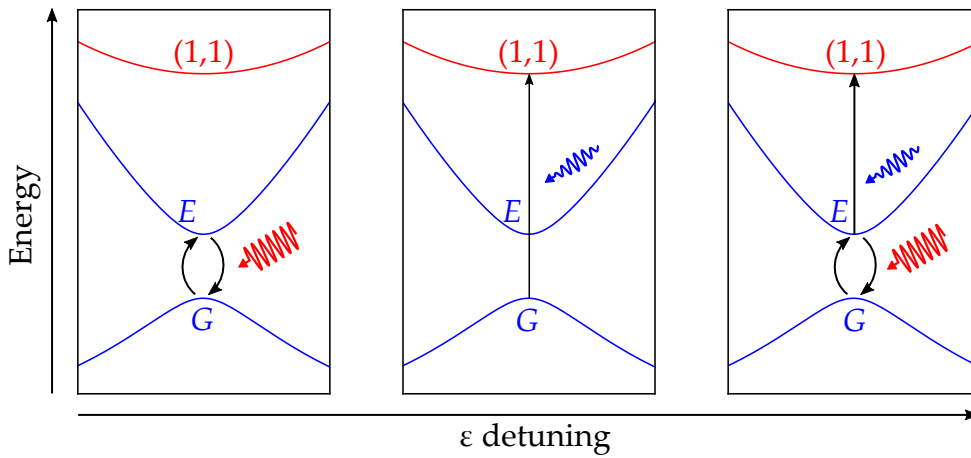
Figure 6.3: Outline of the experiment. (a) A preparation pulse populates the excited Cooper pair state from the ground state. (b) A breaking pulse excites the SDD from the Cooper pair manifold to the (1,1) state. (c) By combining these two processes, we demonstrate pair breaking in which the rate of breaking is dependent on the initial quantum state.

(1,1) (we call this the breaking tone). Both of these sources are externally triggered and modulated by a Tektronix AFG3102 Arbitrary Function Generator to produce microwave pulses at specified time intervals.

6.4 Pulse sequence

To measure the effect on the breaking rate of different populations of $|E\rangle$, we need to determine the population of $|E\rangle$ for a given Rabi tone power, and the breaking rate with and without each tone. To achieve this, we apply the following pulse sequence (Fig. 6.5(a)) and measure the phase response (Fig. 6.5(b), averaging the measurement over 3×10^4 repetitions.

1. A Rabi tone alone, at 7.25 GHz, is applied. The antisymmetric state is populated via three-photon transitions, giving a sharp drop in capacitance on the timescale of the Rabi oscillations, and some pair breaking occurs.

2. The Rabi tone is switched off. The excited population relaxes rapidly ($\sim$ ns), and the broken pair population relaxes more slowly.

3. A breaking tone is applied, resulting in a moderate rate of Cooper pair breaking.

4. The breaking tone is switched off and the broken pair population relaxes.

Room Temp.
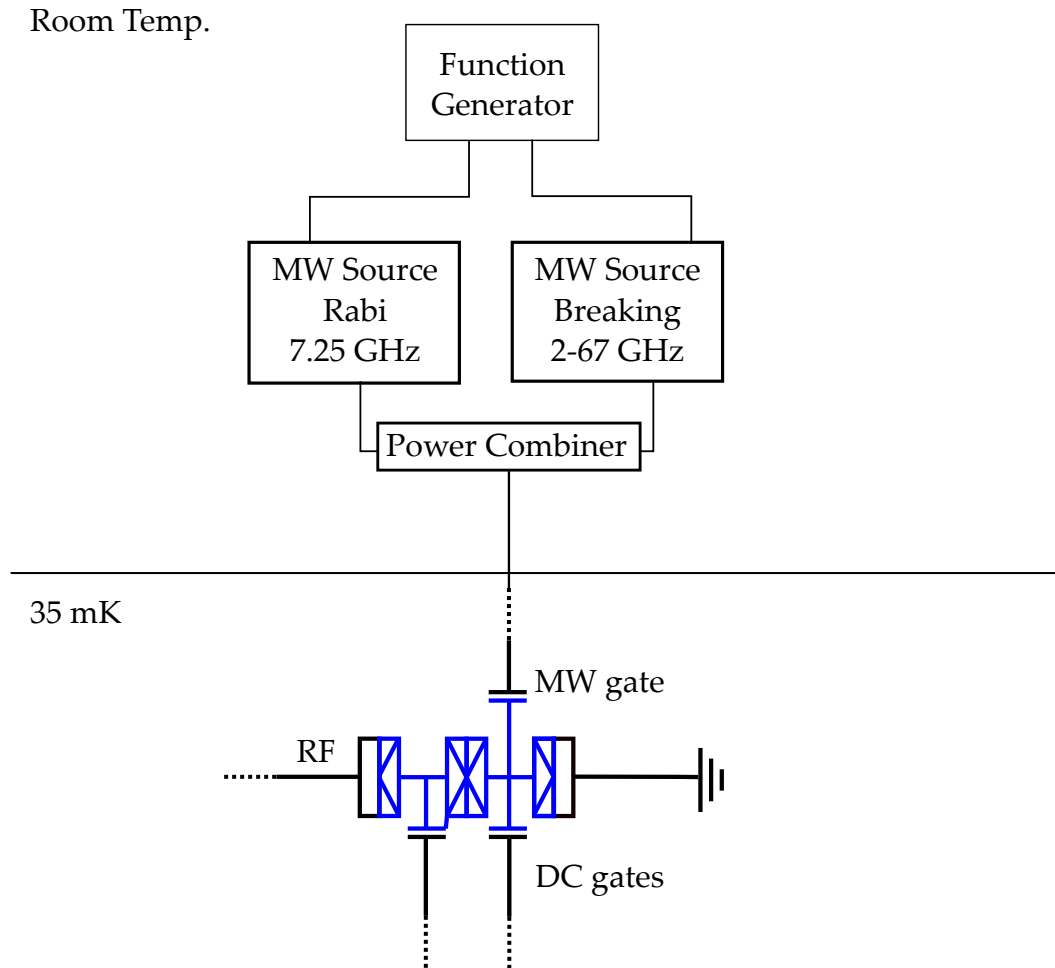
Figure 6.4: Additional experimental setup for state dependent pair breaking. Two microwave sources are connected to the microwave gate via a frequency mixer. Each microwave source is pulse modulated and triggered via one channel of an Arbitrary Function Generator. The pulse lengths, duty cycles and trigger times are set remotely via computer.

5. Both Rabi and breaking tones are applied simultaneously. The antisymmetric state is populated on short timescales, followed by faster pair breaking.

6. Both tones are switched off. The antisymmetric population relaxes rapidly, and the broken pair population relaxes slowly.

We choose the frequency for the three photon transition, as the higher frequency one and two photon transitions induce significant pair breaking when applying power levels necessary to saturate the transition. We choose 40 GHz for the breaking tone and
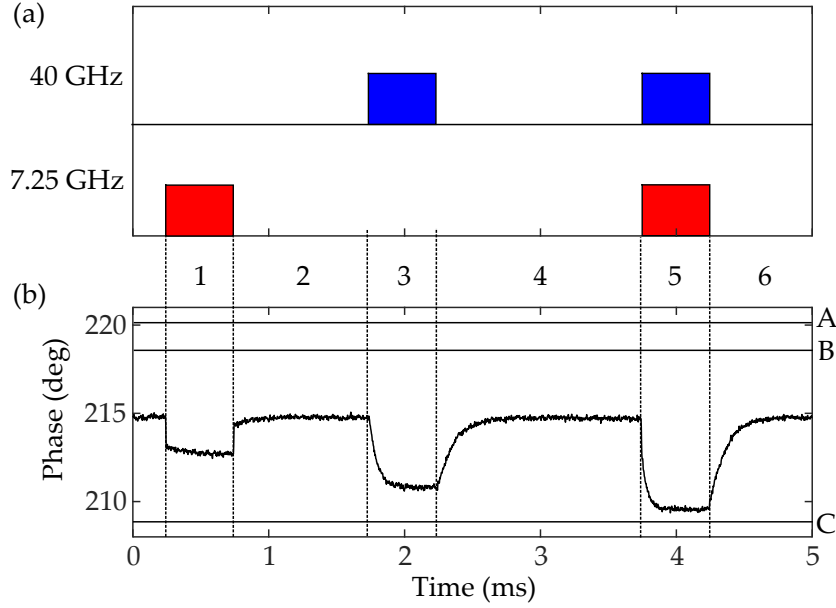
Figure 6.5: Scheme for measuring state dependent Cooper pair breaking. (a) Envelopes of applied microwave pulses as a function of time. 40 GHz pulses intended to break Cooper pairs are show in the top row, and 7.25 GHz pulses to populate the excited Cooper pair state $|E\rangle$ are in the bottom row. (b) Measured phase averaged over 3×10^4 repetitions. The 7.25 GHz radiation populates $|E\rangle$ on timescales much faster than the measurement bandwidth. The change in phase due to Cooper pair splitting driven by the 40 GHz radiation shows as a slower exponential decay in capacitance. From analysis of RTSs, we associate the phase marked A with the ground state $|G\rangle$, B with the weighted mixture of $|E\rangle$ and $|G\rangle$ due to the Rabi tone (0.08 mW in this plot), and C with the (1,1) state. There is a significant quasiparticle population in all sections, so the measured phase is a weighted average of A, B and C.

130 mT for the in-plane magnetic field. The time-dependent quasiparticle population, p_{qp} is given by

$$
\frac{dp_{\text{qp}}(t)}{dt} = \Gamma_{\{G,E\} \to (1,1)} \left(1 - p_{\text{qp}}(t) \right) - \Gamma_{\to \{G,E\}} p_{\text{qp}}(t). \tag{6.2}
$$

The solution to this equation is

$$
p_{\text{qp}}(t) = \frac{\Gamma_{\{G,E\} \to (1,1)}}{\Gamma_{\to \{G,E\}} + \Gamma_{\{G,E\} \to (1,1)}} + C e^{-(\Gamma_{\to \{G,E\}} + \Gamma_{\{G,E\} \to (1,1)})}. \tag{6.3}
$$

C is the constant of integration. The rates Γ now include excitation from and relaxation to both Cooper pair states, $|G\rangle$ and $|E\rangle$.

To convert the time trace in Fig. 6.5(b) to $p_{(1,1)}$, it is necessary to know the capacitance (or phase) change associated with the quasiparticle state. We take 10 s time
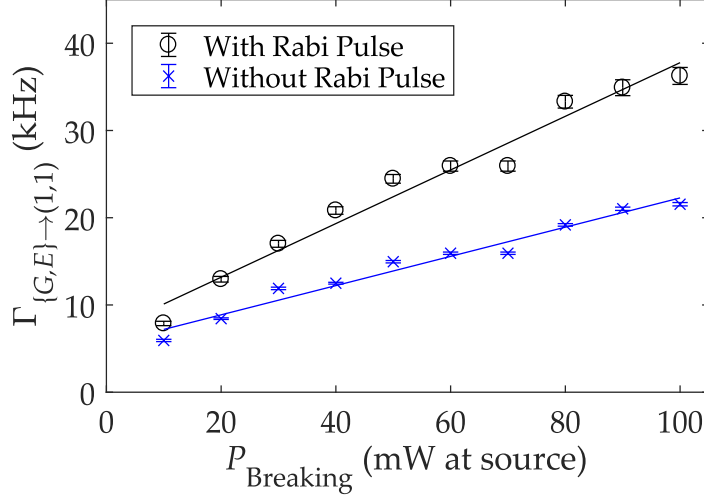
Figure 6.6: Pair breaking rate under simultaneous driving with 0.08 mW 7.25 GHz and 40 GHz tones (black circles) and under 40 GHz driving only (blue crosses) as a function of microwave power (as applied by the source) of the 40 GHz tone. The sensitivity of the SDD in these two regimes are 170 s^{-1} mW^{-1} and 310 s^{-1} mW^{-1}, respectively.

traces with the Rabi pulse off and analyse the random telegraph signal to accurately determine the phases corresponding to the two states, using the technique described in Chapter 3, section 3.4. We also take the same traces with the Rabi pulse on for each power level to determine p_E as a function of Rabi pulse power. We then convert the phase into $p_{(1,1)}$ and fit Eqn. 6.3 to extract the breaking and recombination rates to each section 1-6.

In Fig. 6.6 we show $\Gamma_{\{G,E\} \to (1,1)}$ as a function of breaking tone power for both Rabi tone on and off. The breaking rate is linear with breaking power, as in section, in both cases. However, the sensitivity to microwave radiation (parameterised by $\frac{d\Gamma_{\{G,E\} \to (1,1)}}{dP_B}$) increases when the Rabi pulse is on by $\sim 80\%$.

In Fig. 6.7(a) we confirm this increase in sensitivity is due to the enhanced population of $|E\rangle$ by showing $\Gamma_{\{G,E\} \to (1,1)}$ as a function of Rabi power. The population p_E as a function of Rabi power is estimated from the quantum capacitance signal from the Cooper pair states (Fig. 6.7(b)). By increasing the population of the excited Cooper pair state, we increase $\Gamma_{\{G,E\} \to (1,1)}$ and with it the sensitivity of the device to the breaking tone.

(a)

(b)
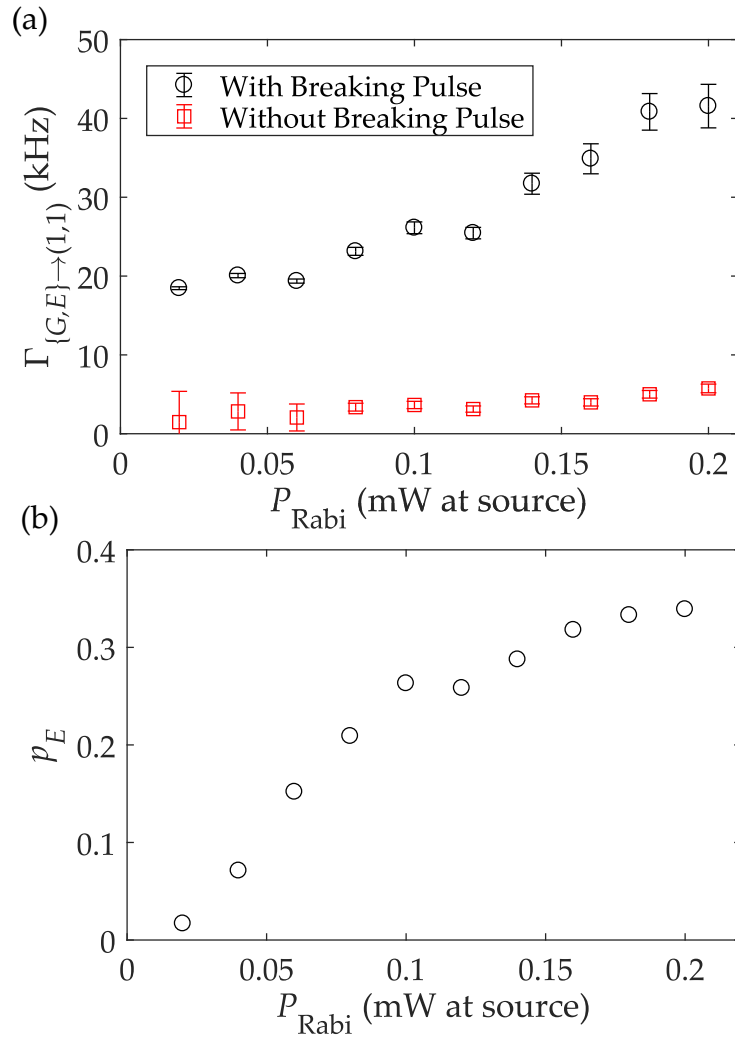
Figure 6.7: (a) Pair breaking rate under simultaneous driving with 0.08 mW 7.25 GHz and 40 GHz tones (black circles) and under 7.25 GHz driving only (red triangles) as a function of microwave power (as applied by the source, attenuation in microwave line given in Chapter 3, Fig. 3.8) of the 7.25 GHz (Rabi) tone. (b) The population of the excited Cooper pair state, p_E as a function of the Rabi tone power.

6.5 Summary

- We drive Rabi oscillations between the ground and excited Cooper pair states of the SDD and measure the relaxation time by fitting to a decay of the averaged normalised capacitance.

- We apply Rabi microwave pulses to populate the excited state and induce pair breaking from the excited state.

- We extract the breaking and recombination rates by measuring the average phase shift and fitting to the time dependent quasiparticle population.

- We observe an enhancement of microwave sensitivity with the presence of the Rabi tone.

- We demonstrate the principle that the probability of Cooper pair breaking may depend on the initial quantum state of the SDD.

GALVANICALLY ISOLATED DOUBLE DOT

In Chapter 5, we concluded that the SDD relaxes from the (1,1) state to the ground Cooper pair state via intermediate charge states, e.g. $(1, 1) \rightarrow (1, 0) \rightarrow (0, 0) \rightarrow |G\rangle$. In other words, the quasiparticles recombine *indirectly* via tunnelling through the normal state leads, which act like quasiparticle traps.

If the SDD had no such leads, then quasiparticles generated from pair breaking will need to recombine *directly*. As recombination requires the quasiparticles to have equal and opposite momentum and spin, quasiparticle lifetimes can be as long as ~ 0.1 ms [158].

In this Chapter, we investigate a superconducting double dot with neither source nor drain leads. The device is completely disconnected from an electron reservoir, meaning that the total charge inside the system is fixed. Furthermore, the double dot geometry is re-designed as a DC-SQUID loop so that the Josephson energy, E_J, can be tuned by varying the out-of-plane magnetic field.

The observed physics depends on whether the number of electrons in the system is odd or even. We measure quantum capacitance and determine a 2*e* periodic charge stability diagram, indicating that the total number of electrons on the dots is even. This is in contrast with those measured in similar structures by Shaw et al., where only *e*-periodicity was observed [149, 159]. We perform simulations of the phase shift due to the quantum capacitance of the device in a RF reflectometry setup and compare the

results with the measured phase shift.

7.1 Device overview
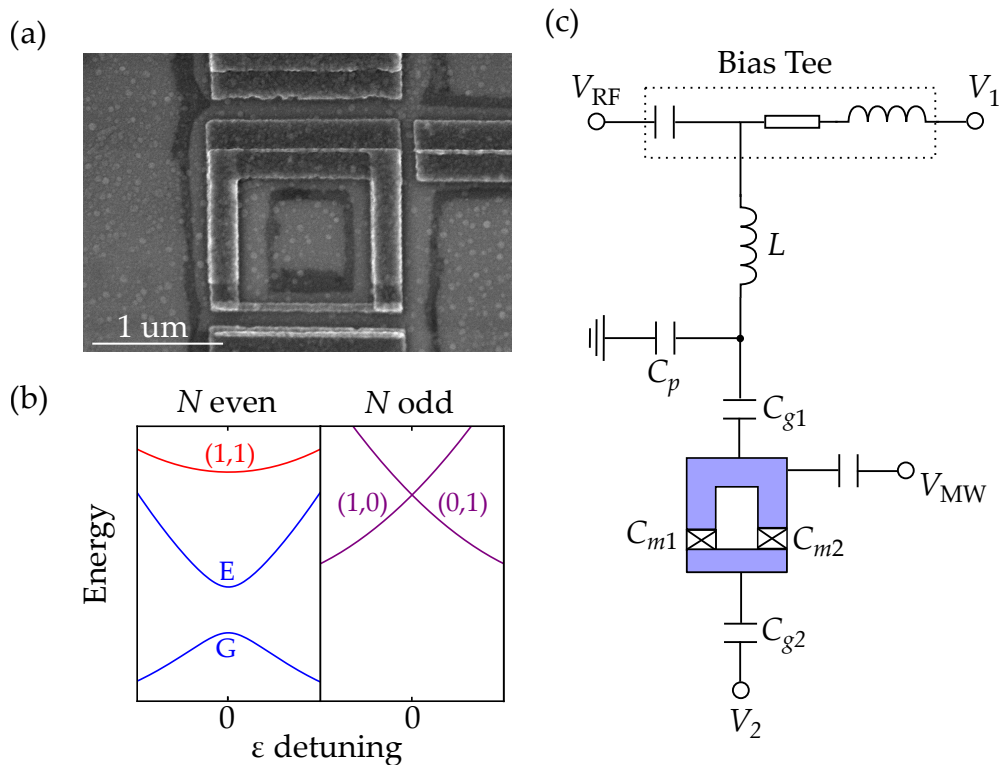
Figure 7.1: (a) An SEM image of an isolated double dot (IsDD). (b) Schematic plot of the accessible charge states (n_1, n_2) of the IsDD when $N = n_1 + n_2$ is even or odd. (c) Schematic diagram of reflectometry setup, including a bias tee which allows an RF carrier signal V_{RF} and a gate voltage V_1 to be sent to the same gate. Other electronic components in the experimental setup are shown in Fig.3.8 in Chapter 3, section 3.3.

The isolated double dot (IsDD) consists of two aluminium islands coupled together by two Josephson junctions in parallel. The two islands form a ring. An SEM image of an example IsDD is shown in Fig. 7.1(a). The plane of the sample is placed perpendicular to the magnetic field, so that the Josephson coupling may be tuned. There are two DC gate electrodes to control the electrochemical potential of each of the dots, and a microwave gate for microwave spectroscopy. The charge states are of the same form as in the superconducting double dot, as discussed in Chapter 4. The key difference is that only a subset of charge states are accessible depending on whether

the total number of charges in the two dot system, $N = n_1 + n_2$, is an even or odd number (Fig.7.1(b)).

7.1.1   Charge periodicity

For even N, the even-parity Cooper pair states $|G\rangle$, $|E\rangle$ and the double odd-parity state (1,1) are accessible. The device may switch between these two states via the breaking and recombination of Cooper pairs. The quasiparticles generated will remain on the dots until they directly recombine. If the breaking rate significantly exceeds the recombination rate, then quasiparticles will always be available to tunnel and the device will be strictly e-periodic at low temperatures. Otherwise, Cooper pairs will tunnel through the barrier and the device will be $2e$ periodic [149].

For odd N, there is always one unpaired quasiparticle in the left or right dot, and only such charge states e.g. (1,0), (0,1) can be accessed. The system will always be in an odd parity, and therefore e-periodic.

7.1.2   Fabrication

The IsDD is fabricated using double angle shadow mask evaporation (Chapter 3, section 3.1.3). For the upper dot, 20 nm of aluminium is evaporated at 0.1 nm/s at an angle of $+8°$. An oxide layer is grown by controlled oxidation at 0.04 mbar for 4 minutes. The lower dot is formed from 20 nm of aluminium evaporated at 0.1 nm/s at $-12°$.

The internal area of the SQUID loop is designed to be as small as possible for a shadow mask evaporation (~ 1 μm^2). This is to maximise the field period $B = \Phi_0/A$, as the resolution of the superconducting magnet in our experimental setup is limited to 0.1 mT with the available power supply. Fabricating a SQUID loop smaller than this would decrease yield, as the resulting shadow mask becomes more susceptible to overhang collapse inside the loop.

7.1.3   Experimental setup

The circuit diagram for the RF reflectometry set up is shown in Fig. 7.1(c). The IsDD is embedded in a lumped element LC resonant circuit with an inductor, $L = 560$ nH, and parasitic capacitance to ground, $C_p = 0.33$ pF. The RF signal is sent via a bias tee to
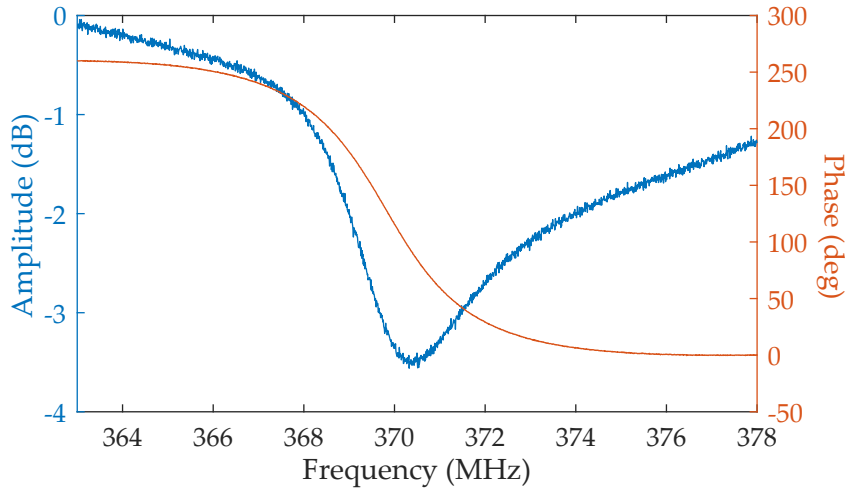
Figure 7.2: Amplitude (blue) and phase (red) components of S_{11} of the RF reflectometry set up with the IsDD.

gate V_1 at the circuit resonant frequency $f = 370.25$ MHz. The phase near resonance varies linearly with frequency at approximately $-56°$/MHz (Fig. 7.2). Using this setup, an increase in quantum capacitance is detected as a decrease in phase. This is different with the setups used in Chapters 5 and 6, where an increase in quantum capacitance is detected as an increase in phase (Chapter 3, section 3.3.2).

7.2 Observation of Cooper pair tunnelling

We measure the average phase shift of the RF signal as a function of the gate voltages V_1 and V_2 with the IsDD at low ($B = 1$ mT, Fig. 7.3(a)) and high ($B = 1$ T, Fig. 7.3(b)) magnetic fields. We observe antidiagonal lines of minimum phase, indicative of charge tunnelling between the dots. These lines indicate that the only accessible charge states (n_1, n_2) are those in which the total charge $N = n_1 + n_2$ is fixed. In other words, charge can be transferred between the dots, but not in or out of the system as a whole.

From Figs. 7.3(a) & (b), we deduce that at low fields the IsDD is in the superconducting state, and at high fields it is in the normal state. The evidence for this is that the periodicity of the lines halve when the IsDD goes from the superconducting state to the normal state (i.e from $2e$ to e). In the superconducting state, the phase shift is due to the quantum capacitance at the anticrossing of the Cooper pair ground state (Chapter 2, section 2.4). In the normal state, the phase shift is due to the Sisyphus
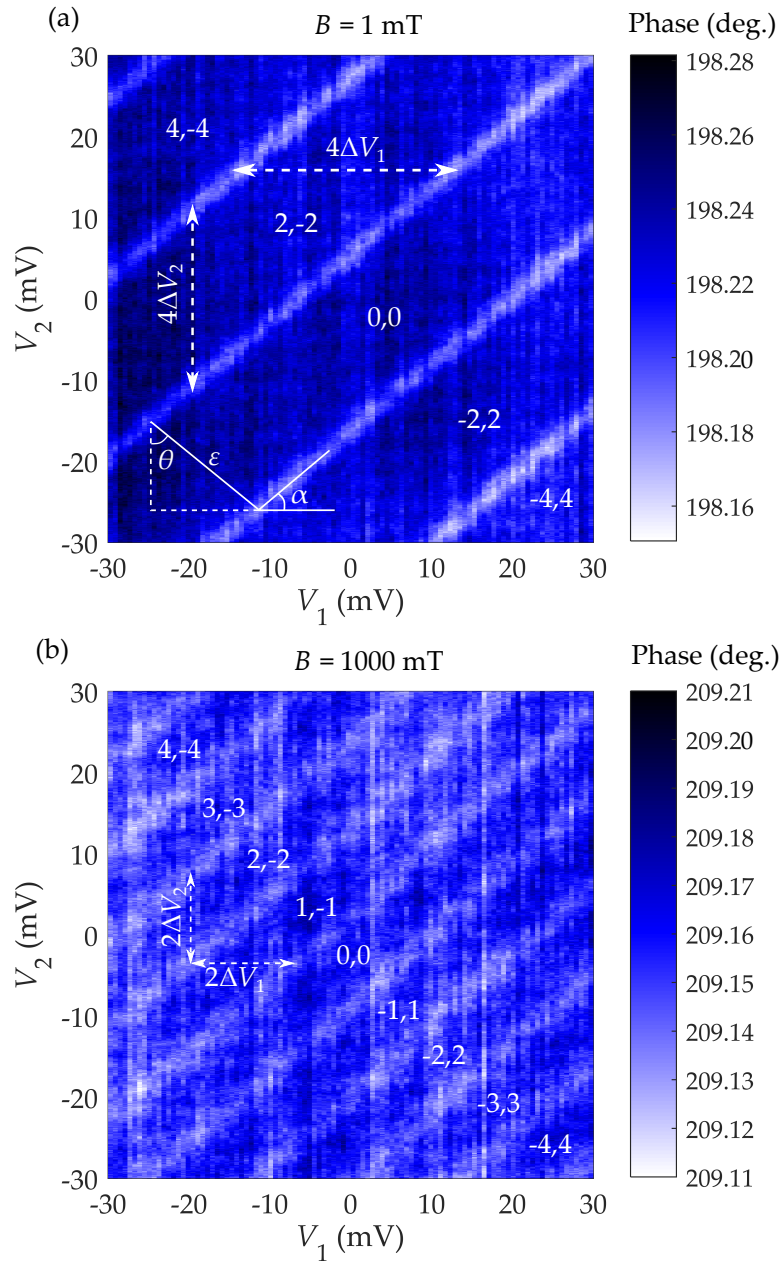
Figure 7.3: Phase shift of IsDD as function of gate voltages (V_1, V_2) in (a) the superconducting state and (b) normal state. Note the number of lines indicating charge tunnelling doubles in frequency in the normal case. This is indicative of electron tunnelling, as opposed to Cooper pair tunnelling in the superconducting state. The angle $\alpha = 40.5°$ is discussed in Section 7.7. The antidiagonal ε-axis (labelled in (a)) is not perpendicular to the charge stability lines due to the slight difference in gate capacitances C_{g1} and C_{g2}. The ε-axis makes an angle $\theta = 47°$ to the V_2-axis.

impedance due to electron tunnelling (Chapter 3, 3.3.7).

The visible $2e$-periodic signal in the superconducting state means that the number of electrons in the IsDD must be even. We observe Cooper pairs tunnelling through the junction, and the population of non-equilibrium quasiparticles is relatively low.

We use the method laid out in Chapter 2, section 2.2.5.5 (from van der Wiel et al.[113]) to find the voltage gate periods ΔV_1 and ΔV_2. These quantities are labelled in Figs. 7.3(a)&(b). However, due to the total charge of the system being fixed, only every other diagonal charge boundary is observed. Hence, in the normal state, the period in gate voltage 1 (2) between Sisyphus impedance peaks is $2\Delta V_{1(2)}$. Consequently, in the superconducting state, the period in gate voltage 1 (2) between quantum capacitance peaks is $4\Delta V_{1(2)}$. This has been confirmed using simulations (Section 7.7), setting the gate capacitances as $C_{g1,g2} = e$.

From the gate periods, we measure the capacitances $C_{g1} = e/\Delta V_1 = 26.7$ aF and $C_{g2} = e/\Delta V_2 = 27.8$ aF. We also estimate a finite microwave gate capacitance $C_{\mathrm{mw}} = 6.6$ aF (see Section 7.7).

7.3 Estimate of device parameters

In the case of the superconducting double dot, it is possible to apply a small source-drain bias and measure bias triangles in order to the extract the device parameters, such as the capacitance of the middle tunnel junction and Josephson energy [113, 103]. In the case for the IsDD, a bias cannot be applied in this way as the device is isolated. We estimate these parameters by comparing the device structure to other devices with known parameters. We also fabricate a test tunnel junction on the same chip with the same designed junction area as that of one of the junctions of the IsDD.

7.3.1 Estimate of C_m

We estimate the capacitance of the middle tunnel junctions C_{m1} and C_{m2} by comparing with our SDD device presented in Chapter 5. We consider the junctions as parallel-plate capacitors, in which their capacitance is proportional to the junction area. These are measured from the SEMs of each device. We do not consider the capacitance contribution from the side wall of the junction, as this is area is negligible compared to the junction overlap in the plane of the sample.
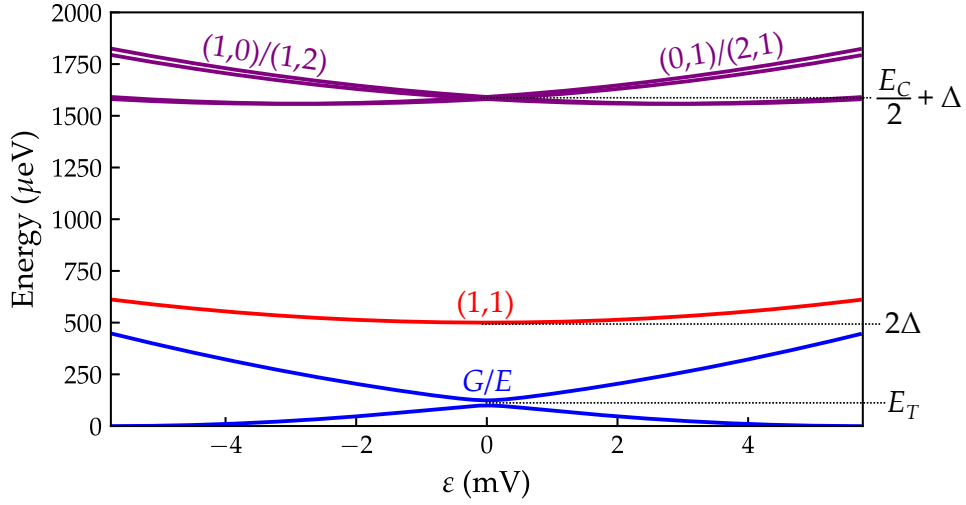
Figure 7.4: Energy bandstructure of the IsDD as a function of ε detuning, wtith annotations of energy scales.

The middle Josephson junction of the SDD has an area of approximately 130 nm $\times$ 71 nm $\approx$ 9230 nm^2 and a capacitance of 220 aF. For the IsDD, the area of the left junction is approximately 180 nm $\times$ 72 nm $\approx$ 12,960 nm^2, and the right junction 200 nm $\times$ 82 nm $\approx$ 16400 nm^2. We then approximate the capacitance of the junctions $C_m = C_{m1} + C_{m2} \approx$ 700 aF.

7.3.2 Estimate of Josephson energy

We estimate the Josephson energy, E_J, using the Ambegokar-Baratoff relation $E_J = h\Delta/8e^2R$. We measure the resistance of the test junction at 4 K to be 66 kΩ. The IsDD has two junctions in parallel, which has approximately the same geometry, and since it was fabricated on the same chip as the IsDD, we assume it has approximately the same tunnel barrier thickness. Therefore, we approximate the normal state resistance of the IsDD as $R = 33$ kΩ. The test junction was not responsive at mK temperatures and thus we could not measure a superconducting gap, so we estimate Δ to be the same as the SDD in Chapter 5 $\Delta = 250$ μeV. From this, we get $E_J = 24$ μeV.

7.4 Energy bandstructure

We use the measured gate capacitances and estimates of the device parameters to calculate the charge state energies of the IsDD. The energies are given by the Hamiltonian of a superconducting double dot, as given in Chapter 4. The electrostatic energy terms $U_{el}(n_1, n_2)$ are derived from the capacitance matrix (as discussed in Chapter 2, section 2.2.5). In this particular case, we let the lead capacitances $C_{S,D} = 0$. We also add the capacitance of the microwave gate C_{mw} as this is now a significant contribution to the overall capacitance of the device.

The total island capacitances $C_1 = 735$ aF and $C_2 = 727$ aF are close to C_m. This results in the charging energies $E_{C1} = 2.6$ meV, $E_{C2} = 2.7$ meV and $E_{Cm} = 2.5$ meV far exceeding Δ. These energies are not relevant to the IsDD, however, as it is not possible to add or remove charge from the double dot system as a whole. We define a transfer energy

$$
\begin{aligned}
E_T &= \frac{1}{2} \left(\mu_1(n_1 + 1, n_2) - \mu_1(n_1, n_2 + 1) + \mu_2(n_1 + 1, n_2) - \mu_2(n_1, n_2 + 1) \right), \\
&= \frac{E_{C1} + E_{C2}}{2} - E_{Cm},
\end{aligned}
\tag{7.1}
$$

which is the change in electrochemical potential (averaged over the two dots) when an electron is transfered from one dot to the other. We get $E_T \approx 112$ μeV, which is lower than Δ. Hence, we observe a $2e$ periodic signal, corresponding to a Cooper pair tunnelling from one dot to the other.

In Fig. 7.4 we plot the energy bandstructure of the IsDD. At $\varepsilon = 0$, the energies of the Cooper pair states are $E_T \pm E_J/2$, and the edge of the $(1,1)$ band lies at 2Δ. The single quasiparticle bands (purple) are much higher in energy than the Cooper pair states and the $(1,1)$ band. This is due to the large charging energies E_{C1} and E_{C2} making the addition or removal of an electron from the double dot system energetically unfavourable.

7.5 Flux periodicity

The Josephson coupling energy between the two dots can be controlled by the magnetic flux through the loop, $\Phi = B \times A_{\mathrm{IsDD}}$. The Josephson energy is

$$
E_J = E_{J,\mathrm{max}} \left| \cos\left(\frac{\pi \Phi}{\Phi_0} \right) \right|,
\tag{7.2}
$$
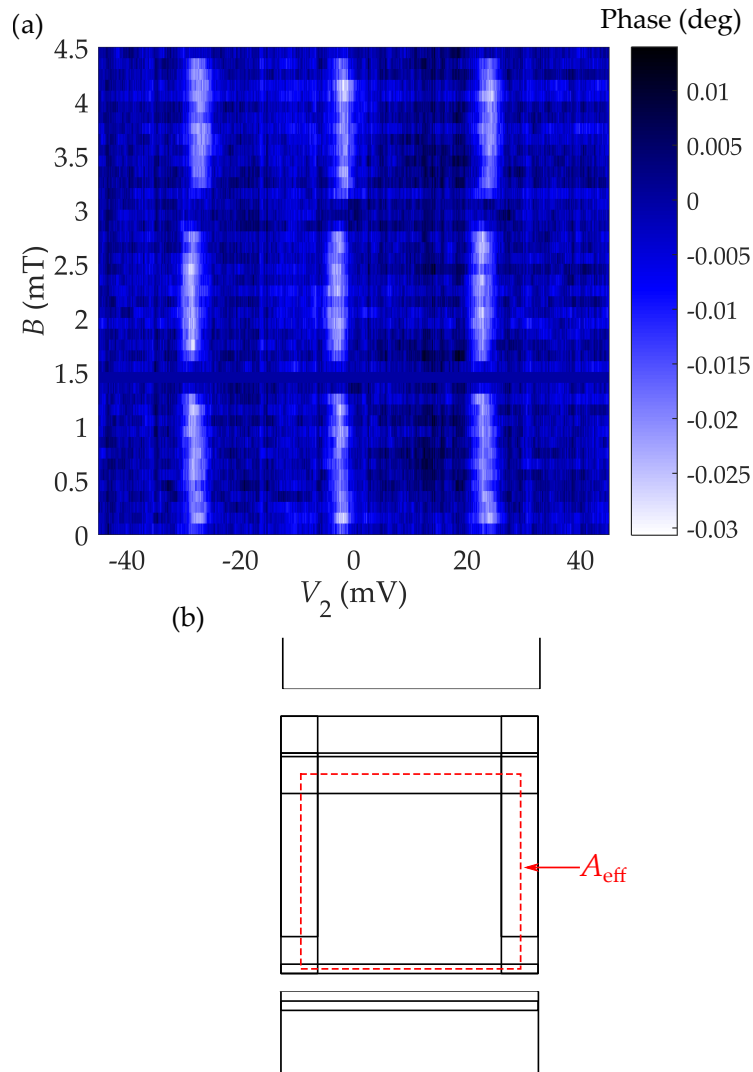
Figure 7.5: (a) Phase shift against gate voltage V_2 and out-of-plane magnetic field, B over three gate periods and three flux periods. (b) A diagram of the IsDD, with the effective area of the loop A_{eff} which includes the flux incident on the aluminium surface expelled into the loop.

where $E_{J,\text{max}}$ is the maximum Josephson energy, reached when Φ/Φ_0 is an integer (Chapter 2, section 2.3.2.1). $\Phi_0 = h/2e$ is the flux quantum. When the magnetic flux equals a half integer multiple of flux quanta, $E_J = 0$. The quantum capacitance of the IsDD varies with the coupling energy, E_J. As E_J decreases, the quantum capacitance increases due to the increased curvature near $\varepsilon = 0$. However, as $E_J \to 0$, thermal occupation of the excited Cooper pair state $|E\rangle$ tends to a maximum of $1/2$. This results in the phase shift tending to zero.

We measure the flux periodicity by measuring the quantum capacitance as a function of magnetic field. We define one period as the difference in magnetic field between two neighbouring minima in capacitance (i.e. maxima in phase). We measure a flux period of 1.5 mT (see Fig. 7.5(a)).

We compare this value with the expected flux period, which we calculate by doing the following method. We measure an effective area, A_{eff}, of the SQUID loop, which is defined by the perimeter halfway between the internal and external perimeters of the loop (see Fig. 7.5(b)) This area encloses all of the magnetic flux which enters the loop, including flux which is expelled from the aluminium surface due to the Meissner effect. We measure $A_{\text{eff}} = (1.38 \pm 0.04))\ \mu\text{m}^2$. The error in the area is derived from the error in the measurement of the device geometry. This gives a predicted magnetic field period of $B = (1.49 \pm 0.04)$ mT, which agrees with our measured value within experimental error.

7.6 Spectroscopy

In principle, it should be possible to extract the charging energy and Josephson energy via microwave spectroscopy (see Chapter 6, section 6.1). We vary the incident microwave power at different frequencies and observe phase shifts at high incident powers. These correspond to excitations between the Cooper pair states. We measure a phase shift due to the formation of dressed states - where Cooper pair states hybridise with the photonic states of the RF drive - and appear as avoided level crossings [160].

However, in this experiment the microwave transmission to the sample is very low, due to the increased attenuation on the microwave line. These phase shifts were observed away from the anticrossing for only three frequencies, 22, 24 and 30 GHz. The plot fof $f = 24$ GHz is shown in Fig. 7.6(a).

Away from the anticrossing (i.e. at normalised gate charges $n_g \ll n_{\text{odd}}$ or $n_g \gg n_{odd}$, where n_{odd} is an odd integer), the energy of the m-photon transition is given by [125]

$$mhf \approx 4E_T\left(n_g - 1\right). \tag{7.3}$$

We fit Lorentzian curves to the phase peaks to accurately determine the position of the peaks (see Figs. 7.6(b)&(c)). The normalised gate charge n_g is defined along the ε-axis (annotated in Fig. 7.3(a)). We transform V_2 to $n_g = C_{g2}V_2/e \times \cos(\theta)$, where $\theta = 47°$.
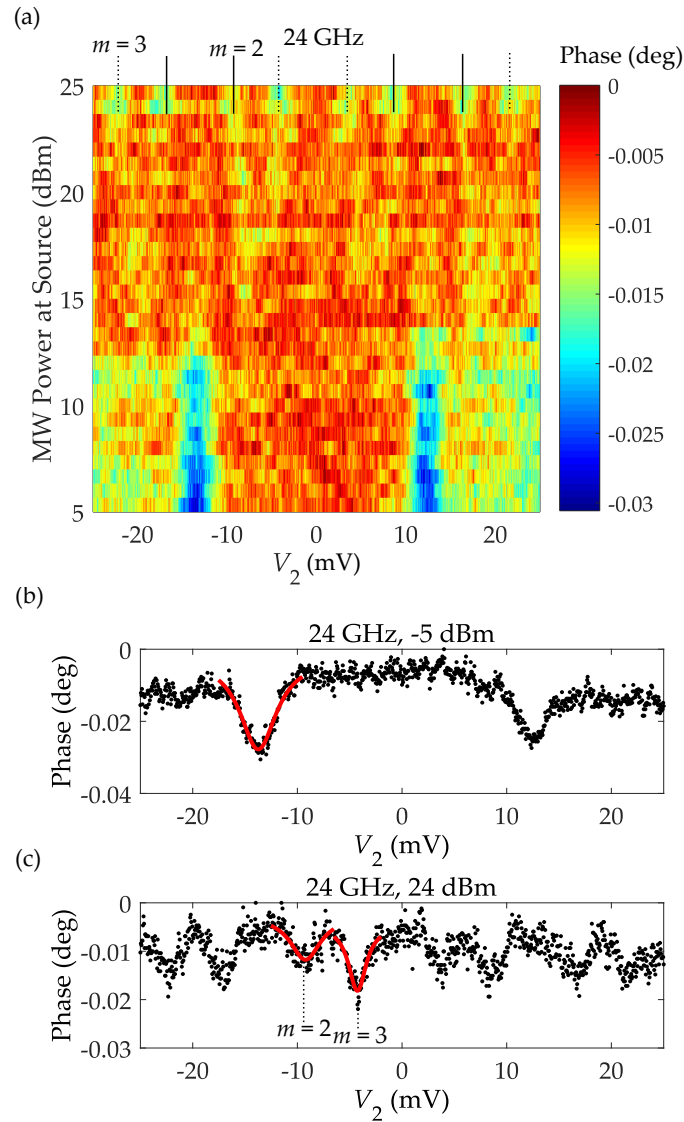
Figure 7.6: (a) Phase shift as a function of V_2 and incident microwave power (at source). (b) Phase at low power, with a fit to one of the peaks due to quantum capacitance (c) Phase at high power, with fits to peaks corresponding to photon assisted tunnelling processes.

We plot the sideband position (relative to the quantum capacitance signal at $n_g = 1$) against microwave frequency and calculate the gradients $\approx mh/4E_T$. The gradient for the first sideband is 0.0188 ± 0.0016 GHz^{-1}, and for the second sideband is 0.0312 ± 0.0037 GHz^{-1}. The ratio of these gradients is, within experimental error, 2:3, indicating that it is likely that these transitions correspond to the two and three photon transitions, respectively. Assuming this, we get $E_T \approx 110\,\mu$eV, which agrees
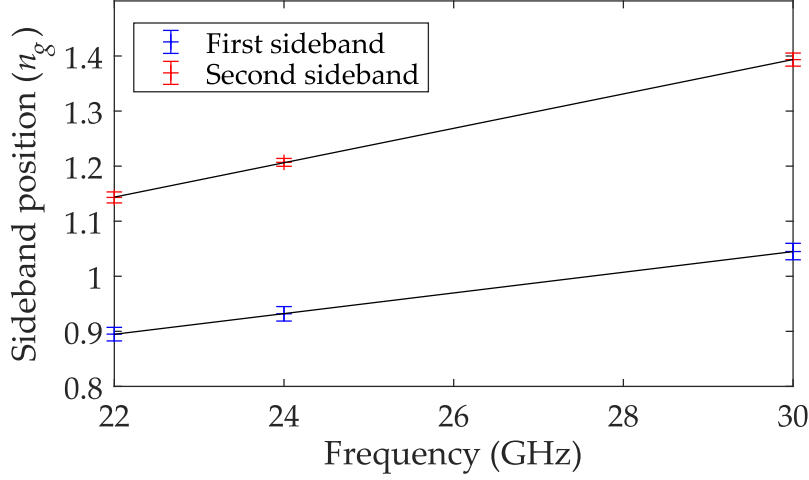
Figure 7.7: Sideband position relative to quantum capacitance signal at the anticrossing. The ratio of the gradients indicate the the first and second sideband are most likely the one and two photon tunnelling transitions.

with our original estimate from the device capacitances.

7.7 Simulations of RF reflectometry

To support the estimates of the device parameters, we simulate the phase shift patterns shown in Fig. 7.3(a) and Fig. 7.5(a) by calculating the quantum capacitance of states $|G\rangle$ and $|E\rangle$ and the resulting phase shift.

7.7.1 Phase shift calculation

We calculate the theoretical capacitance shift

$$\delta C = p_G \cdot C_Q^G + p_E \cdot C_Q^E, \tag{7.4}$$

where $C_Q^k = -\partial^2 E_k/\partial V_2^2$ is the quantum capacitance of the system when purely in state k. The populations of the ground and excited state are

$$p_E = 1 - p_G = \frac{e^{-\Delta E/k_B T}}{1 + e^{-\Delta E/k_B T}}, \tag{7.5}$$

where $\Delta E = \sqrt{16 E_C^2 (1 - n_g)^2 + E_J^2}$ is the energy separation between $|G\rangle$ and $|E\rangle$. We then use this to calculate the expected frequency shift

$$\frac{\delta f}{f} = -\frac{1}{2} \frac{\delta C}{C_p} \tag{7.6}$$

(a)

(b)
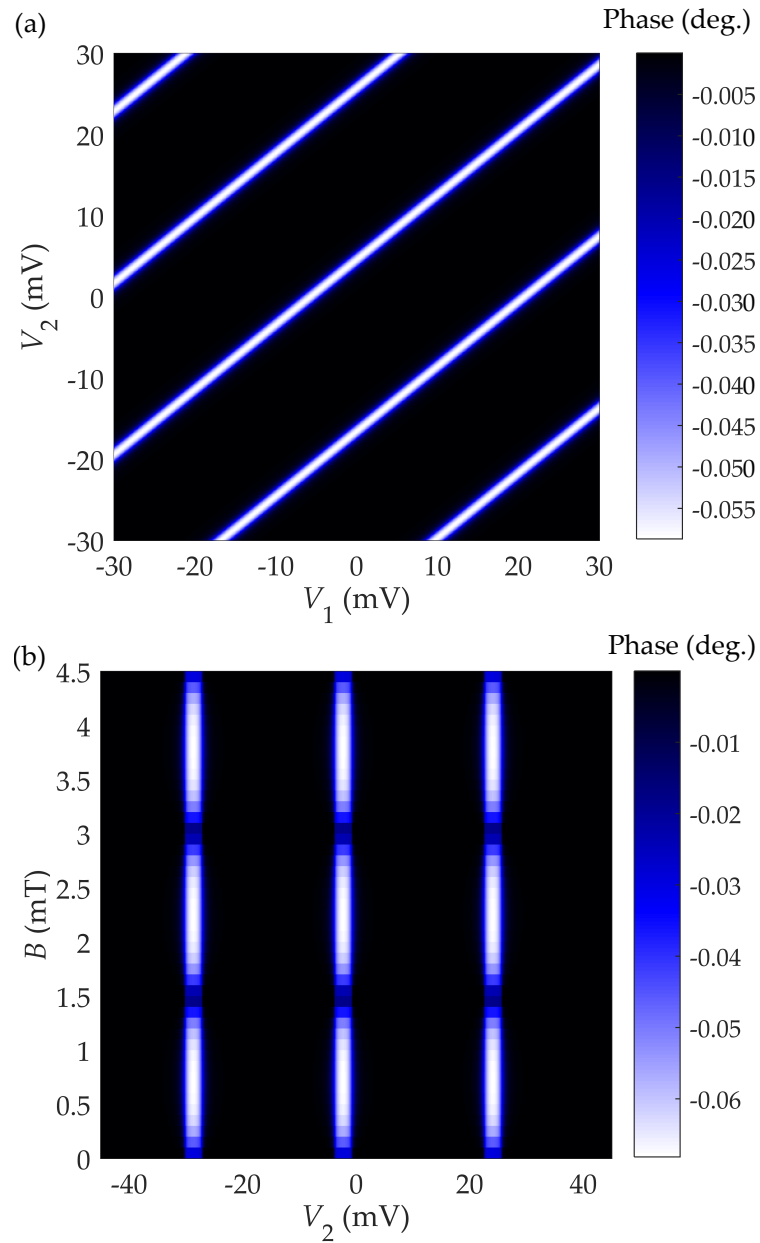
Figure 7.8: Simulations of the phase shift of the IsDD with (a) varying gate voltages V_1 and V_2 and (b) varying out-of-plane magnetic field B and gate voltage V_2. The phase shift is calculated using the method outlined in Section 7.7.1. The parameters used for these simulations are given in Sections 7.7.2 and 7.7.3.

We then use the phase-frequency relation in Eqn. 3.7 to calculate the expected phase shift (Chapter 3, section 3.3.2).

### 7.7.2 Simulated phase shift against gate voltage

In Fig. 7.8(a) we plot the phase shift against gate voltages V_1 and V_2. The resulting pattern matches well with the measured phase shift pattern in Fig. 7.3(a), although we find it necessary to add a capacitance $C_{mw} = 6.6$ aF into the model in order to match the angle that the transition line makes with the V_1 axis, $\alpha = 40.5°$.

7.7.3 Simulated phase shift against magnetic field

We plot the calculated phase shift in Fig. 7.8(b) and find the resulting pattern agrees well with the measurement in Fig. 7.5(a), with a gate period of $\Delta V_2 = 26.5$ mV.

The calculated phase shift is smoothed using a moving average filter over a 2.5 mV range to simulate the effect of RF averaging (over the voltage window equal to the magnitude of the RF carrier signal) and $1/f$ charge noise. We set the temperature $T = 125$ mK, which is the same as the electron temperature determined with an SDD in a similar environment. The resulting magnitude of the phase shift is ~ 0.06 degrees. This is higher than the measured phase shift (~ 0.03 degrees), although the occupation of the (1,1) band has not been taken into account in the model. We expect photons from higher temperature stages in the dilution refrigerator cause non-equilibrium pair breaking, as observed in the SDD (chapters 5 & 6).

7.8 Conclusions

We have measured the quantum capacitance of a galvanically isolated superconducting double dot (IsDD). Although we have estimated some of the device parameters, such as C_m and E_J, there is a close quantitative agreement between our simulations and measurements. Our simulations also demonstrate that the model from van der Wiel et al. [113] even applies to a double dot system without source and drain leads.

This is the first measurement of a superconducting charge isolated device in which $2e$ periodic tunneling is observed. The $2e$ periodicity was observed in one sample out of three; for the other two samples no capacitance shift was observed at either low ($B = 0 - 2$ mT) or high (1000 mT) magnetic fields.

126

Shaw et al. [70] measured four charge isolated double dots (which they call differential single Cooper pair boxes or DSCBs) and measured strictly *e*-periodic behaviour, even with a quasiparticle trap. The authors comment that this is due to quasiparticle poisoning, most likely due to Cooper pair breaking from noise and radiation from the RF-SET charge sensor [70].

We expect that quasiparticles are stochastically generated due to radiation from a noise source, much like what is observed with the SDD (chapters 5 & 6), and to observe random telegraph signals. However, due to the low signal to noise ratio ($\sim 3 - 5$ at a measurement bandwidth of 15 kHz), no such signals could be observed. By comparing the measured phase shift (~ 0.03 deg.) with the model (~ 0.06 deg.), we estimate that the IsDD is poisoned $\sim 50\%$ of the time. This would imply that the pair breaking and quasiparticle recombination rates are roughly equal.

The isolated double dot has potential to be used to examine the lifetimes of single quasiparticle pairs in superconducting aluminium. Furthermore, galvanically isolated devices usually have lower electron temperatures than non-isolated devices [161], which would further increase lifetimes. However, the low capacitive coupling results in a small signal to noise for a given RF carrier power. This is partially mitigated by applying a higher RF carrier power (~ -85 dBm) than is used for previous reflectometry experiments (c.f. ~ -120 dBm for the SDD), but it is not sufficient for time-domain pair breaking and recombination to be observed. Applying a higher RF power leads to significant pair breaking and a reduction in the reflectometry signal.

7.9 Summary

- We fabricate a galvanically isolated superconducting double dot (IsDD), consisting of two superconducting islands coupled together with a Josephson junction. The islands are decoupled from an electron reservoir, meaning that the charge on the dots is fixed.

- We measure quantum capacitance as a function of gate voltage and detect a $2e$ periodic signal, indicating the tunnelling of Cooper pairs and low quasiparticle occupation.

- We measure the phase shift due to the quantum capacitance of the IsDD with varying gate voltage and magnetic flux. We find that it agrees with our model with estimates of the device capacitances and Josephson energy.

- Due to the low coupling to the double dot system and the low signal to noise ratio, random telegraph signals due to pair breaking and recombination could not be measured.

CONCLUSIONS AND FURTHER WORK

8.1 Conclusions

This thesis has presented experiments on charge dynamics in superconducting double dots (SDDs). Specifically, we observe the tunnelling of Cooper pairs and quasiparticles, the breaking of Cooper pairs and the recombination of quasiparticles. Radio frequency reflectometry has been used throughout to detect the charge state of a device, either by measuring the quantum capacitance of the device or the quantum capacitance of a charge sensor.

In Chapter 4, we studied the charge stability diagram and energetics of the superconducting double dot, and determined that behaviour of the SDD depends on the competition between the charging energies and the superconducting gap, Δ. To confirm our models, we fabricated an SDD with a Cooper pair box charge sensor. We measured the quantum capacitance of both the SDD and of the Cooper pair box, and observed both even and odd parity states in the charge stability diagram.

In Chapter 5, we observed, in the time domain, the breaking of single Cooper pairs and subsequent recombination of the resulting quasiparticles. These processes were observed by measuring the stochastic switching between two capacitance values. By measuring the breaking rate and fitting the data to a black-body radiation spectrum, we established that pair breaking is caused by photons due to thermal noise from a

microwave attenuator in the dilution refrigerator. This demonstrates that the SDD can be used to detect the presence of photons in the ambient environment. We apply microwave excitations to the SDD and find that the rate of pair breaking increases linearly with incident microwave power. We conclude that the pair breaking is a single photon process, and the SDD has the potential to be used as a single photon detector in the microwave spectrum. This has potential applications in quantum information processing.

In Chapter 6, we used a Rabi pulse to excite the SDD from the symmetric ground Cooper pair state to the antisymmetric excited Cooper pair state before applying a microwave pulse to break pairs. We conclude that the rate of pair breaking is dependent on the symmetry of the initial Cooper pair state.

In Chapter 7, we fabricated and performed experiments on a galvanically isolated superconducting double dot. We observed $2e$-periodic signals indicated the tunnelling of Cooper pairs. We would expect to detect the continuous breaking and recombination of pairs, similar to what was observed in the SDD. However, this was not observed due to the low signal to noise ratio as a result of the small capacitative coupling between the device and the RF gate. A measurement of the recombination rate in this device would represent the direct recombination of quasiparticles.

In the context of superconducting devices described in Chapter 1, SDD acts as a Cooper pair splitter in which the resulting quasiparticles are retained in separated islands until the quasiparticles recombine via diffusion to the leads. The key findings are that the rich range of charge dynamics observed in the SDD have been explored with theoretical analyses and that the device can potentially be used to detect microwave light.

8.2 Further work

There are two areas of further work in which the SDD can be used for quantum information processing. In the low charging energy regime, ($E_C < \Delta$), the SDD can be used to detect microwave photons. In the high charging energy regime, ($E_C > 2\Delta$), the SDD may be used to measure the spin dephasing time of a quasiparticle spin pair.
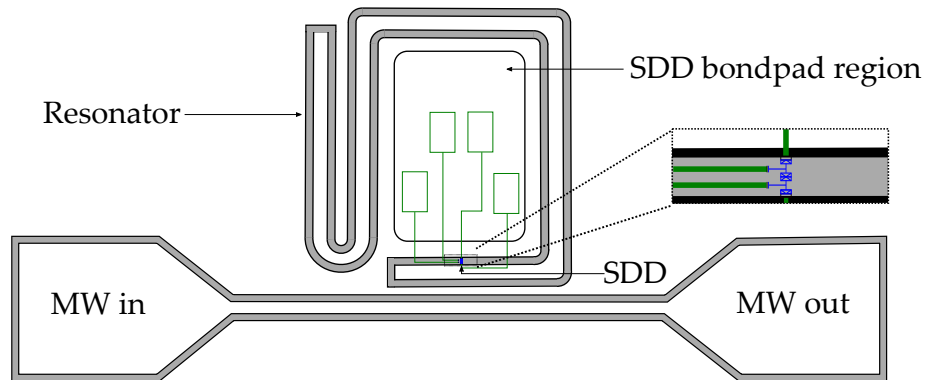
Figure 8.1: Schematic diagram of a transmission line resonator to be used with the SDD as a single microwave photon detector. Bondpads for the gates and leads of the SDD are coloured in green. The SDD is placed near the antinode of the resonator so that the coupling electromagnetic field is maximal [162].

8.2.1 Superconducting resonators for single photon detection

As discussed in Chapter 5, the SDD has the potential to be a single microwave photon detector. Such a detector would be most suitable for detecting photons in a quantum computing architecture based on circuit quantum electrodynamics (cQED) [56]. We note that there needs to be some improvement in the dark count of the device ($\sim$ 2 kHz), which can possibly be achieved using additional attenuation on the microwave cables. The property that needs the most improvement, however, is the detection efficiency.

The quantum efficiency is low due to the poor impedance matching between the device and the microwave gate. This can be improved on by embedding the SDD with a superconducting transmission line resonator, with an impedance closer to that of the environment [163]. Such resonators have been used in cQED to provide strong coupling between a superconducting qubit and microwave photons [56].

Dr Megan Edwards has designed and fabricated superconducting resonators for the purpose of enhancing the quantum efficiency of the SDD photon detector. The SDD would be fabricated on top the resonator via electron beam lithography and placed at the antinode of the electric field for maximum coupling. The device would then be tuned to detect photons whose frequency is within the linewidth of the resonant frequency of the loaded resonator [162].

These resonators are quarter wavelength transmission line resonators, defined by optical lithography. The conductor material is chosen to be aluminium, deposited by

evaporation. The quality factor of the resonators was measured to be $\sim 10^3$. To achieve the single photon limit, we estimate that a quality factor of $\sim 10^6$ would be necessary. This could be achieved by using a fabrication technique which produces a high quality film of aluminium e.g. molecular beam epitaxy [164].

8.2.2 Measuring the spin dephasing time of quasiparticle pair

Alternatively, the SDD could be used to study the dynamics of quasiparticle spin in the superconducting double dot. Spin states are largely decoupled from charge noise induced by two level fluctuators [129], resulting in longer relaxation times than in charge states [96, 116]. In particular, quasiparticles have been shown to have a long spin lifetime in superconducting aluminium ($T > 100\,\mu$s) [158].

The similarity between the SDD and the semiconductor double quantum dot (DQD) means that we are able to use techniques pioneered in this system [96, 97] to perform a measurement of the spin coherence time, T_2, of a single quasiparticle pair. The study of spin coherence of quasiparticles allows us to determine the feasibility of a superconducting spin qubit.

8.2.2.1 Spin states

For two electrons or quasiparticles, here are four possible spin configurations. There is one singlet state

$$|S\rangle = \frac{1}{\sqrt{2}}\left(|\uparrow\downarrow\rangle - |\downarrow\uparrow\rangle\right), \tag{8.1}$$

and three triplet states

$$
\begin{aligned}
|T_+\rangle &= |\uparrow\uparrow\rangle \\
|T_0\rangle &= \frac{1}{\sqrt{2}}\left(|\uparrow\downarrow\rangle + |\downarrow\uparrow\rangle\right) \\
|T_-\rangle &= |\downarrow\downarrow\rangle.
\end{aligned}
\tag{8.2}
$$

For the (1,1) quasiparticle band at zero magnetic field, the singlet and triplet spin states are degenerate. However, like the double quantum dot, the singlet state (S(2,0)) is lower in energy (by 2Δ) than the triplet states (T(2,0)). This is because the quasiparticles in the singlet configuration can recombine to form a Cooper pair, but cannot in the triplet state.

132
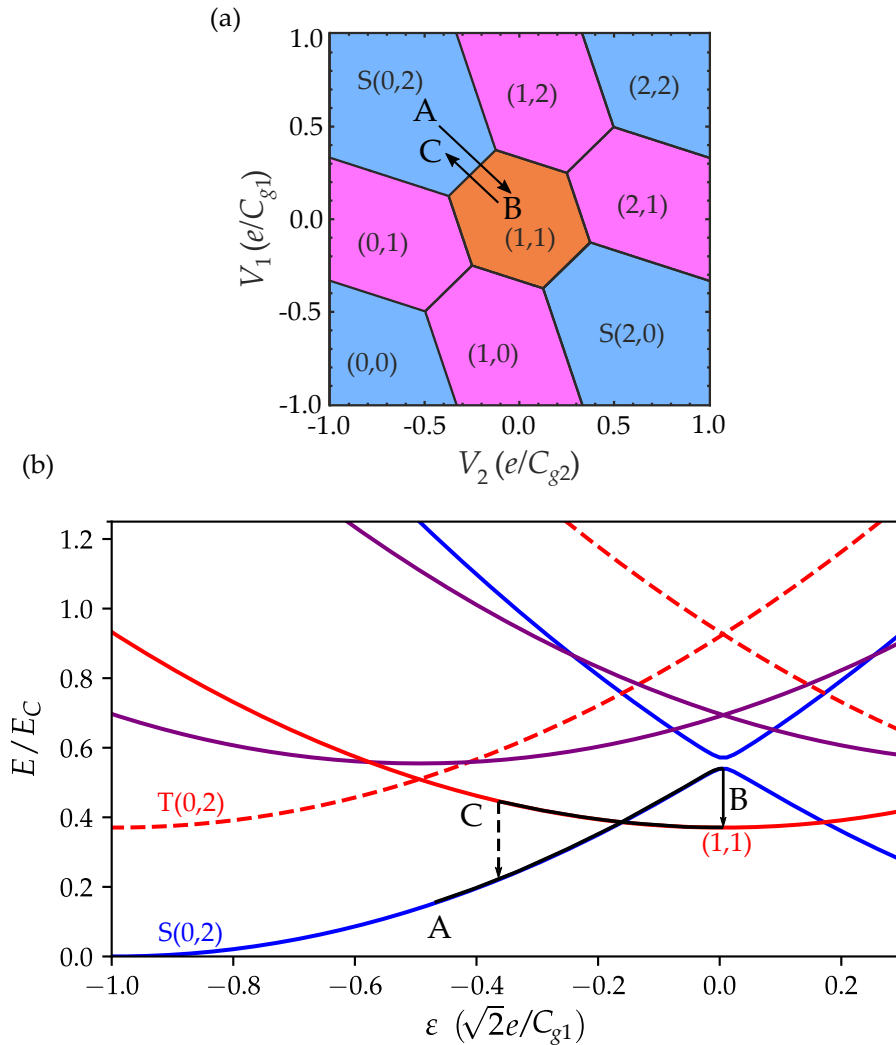
Figure 8.2: Protocol of measuring the dephasing time of a quasiparticle spin. We start in the Cooper pair S(0,2) state (point A) and apply a gate voltage pulse and go to point B. The system relaxes to the (1,1) state, and a Cooper pair breaks. We wait a time τ to allow the quasiparticles to dephase into a statistical mixture of spin states. We then apply a gate pulse to point C. If the spins are in the singlet configuration, the system will relax to S(0,2). If the spins are in the triplet configuration, the system will remain in the (1,1) state as the triplet T(0,2) quasiparticle band is higher in energy.

To perform the spin measurement, we require the (1,1) state to be the ground state for some region in gate space. We recall in Chapter 4 that this occurs in the high charging energy regime i.e. $E_{C1,C2} > 2\Delta$.

8.2.2.2 Measurement protocol

In Fig.. 8.2(a), I show the charge stabilty diagram of the SDD in the high charging energy regime, labelled with points A, B and C. In Fig. 8.2(b), I plot the energy diagram of the SDD in the antidiagonal axis. We plot an additional energy state, the triplet T(2,0) which corresponds to two unpaired quasiaparticles in one dot in a triplet spin configuration.

The measurement protocol is based on spin-to-charge conversion, similar to that performed in semiconductor double quantum dots, such as Petta et al. [96]. A voltage pulse from the (2,0) region (point A) to the (1,1) breaks a Cooper pair (point B). Initially, the quasiparticles will be in the singlet S(1,1) state, but will begin to dephase to a statistical mixture of the S(1,1) and T(1,1) states. After a wait time τ fast voltage pulse takes the ground state from (1,1) to a region where S(2,0) is the ground state (point C). If the quasiparticles are in the single state, they will recombine to form a Cooper pair and relax to the ground state. If the quasiparticles are in the triplet state, they will remain in the T(1,1) state. A nearby charge sensor detects the charge state, from which the spin state is determined. By repeating the protocol and varying τ, we can plot the singlet probability against τ and extract the dephasing time T_2^*.

8.2.2.3 Readout

In Chapter 4, we used a Cooper pair box as a charge sensor. For this measurement, we would require a charge sensor to be able to perform a single-shot readout with high fidelity. This has been achieved in metallic double dots with the use of a radio-frequency single electron transistor (RF-SET) [165].

The response of the RF-SET is measured via radio-frequency reflectometry, similar to the measurement of quantum capacitance of the SDD. The power of the reflected RF signal is maximum when the SET is in Coulomb blockade, and decreases when the transistor becomes conducting [166]. The reflected power is a function of the local electrostatic environment, set by the voltage gates of the SDD and SET and the charge occupation of the dots.

8.2.2.4 A superconducting spin qubit

The SDD has the potential to be used as a superconducting spin qubit, which would be operated like the semiconductor double quantum dot (DQD) spin qubit [167].

However, it is necessary to have a well-defined qubit basis. In the DQD, this is $|S\rangle$ and $|T_0\rangle$, which are separated via the exchange interaction energy [96]. In the SDD, the quasiparticles do not have a well-defined momentum. This potentially affects the ability to perform well-controlled qubit gates via the exchange interaction.

An alternative method would be to apply a magnetic field to split the $|T_+\rangle$ and $|T_-\rangle$ states from the $|S\rangle$ and $|T_0\rangle$ states. The qubit levels would then be the $|S\rangle$ and $|T_+\rangle$. These states differ in spin angular momentum by $\hbar$ and the transition can be driven by electron spin resonance. This would be possible with the use of a on-chip microwave antenna to drive an oscillating magnetic field [168].

The energy splitting between $|S\rangle$ and $|T_+\rangle$ would need be greater than the thermal energy. This would require a magnetic field of $B \sim 500$ mT [169]. It is important that the superconducting gap is large enough at this field, such that when in the (2,0) state, non-equilibrium quasiparticle excitations are suppressed.

Although spin lifetimes (T_1) of quasiparticles may be long in superconducting aluminium ($\gtrsim 1$ μs), an open question remains on T_2 of quasiparticle spins. Quay et al. [170] have performed "quasiparticle spin resonance" (QSR) in superconducting aluminium transistors. The authors measured an average quasiparticle spin coherence time of $T_2 \sim 100$ ps, and find that the dominant decoherence mechanism is spin-orbit scattering. It is possible that coherence times could be improved if the time averaged number of generated quasiparticle pairs is approximately unity, like in the SDD. T_2 would be measured using spin-Hahn echo pulse sequences, as described in Petta et al. [96].

Derivation of N_{eff} - the number of available quasiparticle excitations

From Tuominen et al. [64], the number of quasiparticle states available for thermal excitation in a BCS superconductor is given as

$$N_{eff} = 2VD(E_F) \int_\Delta^\infty \exp\left(-\frac{E-\Delta}{kT}\right) \frac{E}{\sqrt{E^2 - \Delta^2}} dE, \tag{A.1}$$

where V is the volume of the superconductor and $D(E_F)$ is the density of states at the Fermi level (in the normal state). The factor of 2 comes from the fact that we should also integrate over the negative energies (hole-like quasiparticles) [17].

This integral is analytically solved to give

$$N_{eff} = 2VD(E_F)\Delta \exp\left(\frac{\Delta}{kT}\right) K_1\left(\frac{\Delta}{kT}\right). \tag{A.2}$$

K_1 is known as the first-order modified Bessel function of the second kind [147]

$$K_1(z) = \sqrt{\frac{\pi}{2z}} \frac{e^{-z}}{\left(\frac{1}{2}\right)!} \sum_{r=0}^\infty \frac{\left(\frac{1}{2}\right)!}{r!\left(r+\frac{1}{2}\right)!} (2z)^{-r} \int_0^\infty e^{-t} t^{r+\frac{1}{2}} dt. \tag{A.3}$$

From the gamma function, $\left(\frac{1}{2}\right)! = \frac{\sqrt{\pi}}{2}$. Now in this case, $z = \Delta/kT$, and since we are in the regime $\Delta/kT \gg 1$, let's only consider the first term ($r = 0$) in the infinite

sum. We get

$$K_1\left(\frac{\Delta}{kT}\right) \simeq \sqrt{\frac{\pi}{2}}\sqrt{\frac{kT}{\Delta}} \cdot \frac{2e^{-\Delta/kT}}{\sqrt{\pi}} \cdot \frac{\frac{\sqrt{\pi}}{2}}{1 \cdot \frac{\sqrt{\pi}}{2}} \cdot \frac{\sqrt{\pi}}{2}, \tag{A.4}$$

where the last factor in the term comes from the integral $\int_0^\infty e^{-t}\sqrt{t}dt$. Substituting this into Eqn A.2 gives

$$\begin{aligned} N_{eff} &= 2VD(E_F)\Delta\exp\left(\frac{\Delta}{kT}\right) \cdot \sqrt{\frac{\pi}{2}}\sqrt{\frac{kT}{\Delta}}\exp\left(-\frac{\Delta}{kT}\right) \\ &= \sqrt{2\pi\Delta kT}VD(E_F), \end{aligned} \tag{A.5}$$

which was to be proved.

Note the definition of $D(E_F)$. In some publications, this is defined as the *single-spin* normal-state density of states at the Fermi level. In this case, the final expression above has an additional factor of 2.

BIBLIOGRAPHY

[1] N. J. Lambert et al., "Experimental observation of the breaking and recombination of single Cooper pairs," *Physical Review B* **90** 14, 140503(R) (2014).

[2] N. J. Lambert et al., "Quantum capacitance and charge sensing of a superconducting double dot," *Applied Physics Letters* **109** 11, 112603 (2016).

[3] N. J. Lambert et al., "Microwave irradiation and quasiparticles in a superconducting double dot," *Physical Review B* **95** 23, 235413 (2017).

[4] B. Yurke et al., "Observation of 4.2-K equilibrium-noise squeezing via a josephson-parametric amplifier," *Physical Review Letters* **60** 9, 764–767 (1988).

[5] M. Mück and R. McDermott, "Radio-frequency amplifiers based on dc SQUIDs," *Superconductor Science and Technology* **23** 9, 093001 (2010).

[6] D. Drung et al., "Highly sensitive and easy-to-use SQUID sensors," *IEEE Transactions on Applied Superconductivity* **17** 2, 699–704 (2007).

[7] A. Peacock et al., "Single optical photon detection with a superconducting tunnel junction," *Nature* **381** 6578, 135–137 (1996).

[8] A. J. Ferguson, "Quasiparticle cooling of a single Cooper pair transistor," *Applied Physics Letters* **93** 5, 052501 (2008).

[9] G. Wendin, "Quantum information processing with superconducting circuits: a review," *Reports on Progress in Physics* **80** 10, 106001 (2017).

[10] IBM, "IBM Q." `http://www.research.ibm.com/ibm-q/`.

[11] M. Tinkham, *Introduction to Superconductivity*. Dover, 2nd ed., 1996.

[12] S. B. Kaplan et al., "Quasiparticle and phonon lifetimes in superconductors," *Physical Review B* **14** 11, 4854–4873 (1976).

[13] R. Barends et al., "Minimizing quasiparticle generation from stray infrared light in superconducting quantum circuits," *Applied Physics Letters* **99** 11,

113507 (2011).

[14] K. Lang et al., "Banishing quasiparticles from Josephson-junction qubits: Why and how to do it," *IEEE Transactions on Appiled Superconductivity* **13** 2, 989–993 (2003).

[15] L. Sun et al., "Measurements of quasiparticle tunneling dynamics in a band-gap-engineered transmon qubit," *Physical Review Letters* **108** 23, 230509 (2012).

[16] P. J. de Visser et al., "Generation-Recombination Noise: The Fundamental Sensitivity Limit for Kinetic Inductance Detectors," *Journal of Low Temperature Physics* **167** 3-4, 335–340 (2012).

[17] J. T. Muhonen, M. Meschke, and J. P. Pekola, "Micrometre-scale refrigerators," *Reports on Progress in Physics* **75** 4, 046501 (2012).

[18] C. M. Natarajan, M. G. Tanner, and R. H. Hadfield, "Superconducting nanowire single-photon detectors: physics and applications," *Superconductor Science and Technology* **25** 6, 063001 (2012).

[19] L. Hofstetter et al., "Cooper pair splitter realized in a two-quantum-dot Y-junction," *Nature* **461** 7266, 960–3 (2009).

[20] L. G. Herrmann et al., "Carbon nanotubes as Cooper-pair beam splitters," *Physical Review Letters* **104** 2, 026801 (2010).

[21] D. van Delft and P. Kes, "The discovery of superconductivity," *Physics Today* **63** 9, 38–43 (2010).

[22] W. Meissner and R. Ochsenfeld, "Ein neuer effekt bei eintritt der supraleitfähigkeit," *Naturwissenschaften* **21** 787 (1933).

[23] J. Bardeen, L. N. Cooper, and J. R. Schrieffer, "Theory of superconductivity," *Physical Review* **108** 5, 1175–1204 (1957).

[24] L. N. Cooper, "Theory of superconductivity," *American Journal of Physics* **28** 2, 91–101 (1960).

[25] B. Josephson, "Possible new effects in superconductive tunnelling," *Physics Letters* **1** 7, 251–253 (1962).

[26] B. D. Josepshon, "Coupled superconductors," *Reviews of Modern Physics* **36** 1, 216–220 (1964).

[27] R. Kleiner et al., "Superconducting quantum interference devices: State of the art and applications," *Proceedings of the IEEE* **92** 10, 1534–1548 (2004).

[28] M. Hämäläinen et al., "Magnetoencephalography—theory, instrumentation,

and applications to noninvasive studies of the working human brain," *Reviews of Modern Physics* **65** 2, 413–497 (1993).

[29] J. P. Wikswo and J. P. Barach, "Possible sources of new information in the magnetocardiogram," *Journal of Theoretical Biology* **95** 4, 721–729 (1982).

[30] H. L. Grossman et al., "Detection of bacteria in suspension by using a superconducting quantum interference device," *Proceedings of the National Academy of Sciences* **101** 1, 129–134 (2003).

[31] Y. S. Greenberg, "Application of superconducting quantum interference devices to nuclear magnetic resonance," *Reviews of Modern Physics* **70** 1, 175–222 (1998).

[32] R. McDermott et al., "SQUID-detected magnetic resonance imaging in microtesla magnetic fields," *Journal of Low Temperature Physics* **135** 5/6, 793–821 (2004).

[33] C. A. Hamilton, "Josephson voltage standards," *Review of Scientific Instruments* **71** 10, 3611 (2000).

[34] J. Kohlmann, R. Behr, and T. Funck, "Josephson voltage standards," *Measurement Science and Technology* **14** 8, 1216–1228 (2003).

[35] N. I. of Science and T. (NIST), "A Primary Voltage Standard for the Whole World." `https://www.nist.gov/news-events/news/2013/04/primary-voltage-standard-whole-world`.

[36] D. Ristè et al., "Millisecond charge-parity fluctuations and induced decoherence in a superconducting transmon qubit," *Nature Communications* **4** 1913 (2013).

[37] P. W. Shor, "Polynomial-time algorithms for prime factorization and discrete logarithms on a quantum computer," *SIAM Review* **41** 2, 303–332 (1999).

[38] K. D. Petersson, *High Frequency Manipulation and Measurement of Charge and Spin States in GaAs Quantum Dot Devices*. PhD thesis, University of Cambridge, 2009.

[39] J. Clarke and F. K. Wilhelm, "Superconducting quantum bits," *Nature* **453** 7198, 1031–1042 (2008).

[40] G. Catelani et al., "Decoherence of superconducting qubits caused by quasiparticle tunneling," *Physical Review B* **86** 18, 184514 (2012).

[41] A. M. Tyryshkin et al., "Electron spin coherence exceeding seconds in high-purity silicon," *Nature Materials* **11** 2, 143–147 (2011).

[42] A. M. Zagoskin, *Quantum Engineering: Theory and Design of Quantum Coherent Structures*. Cambridge University Press, 2011.

[43] M. H. Devoret and R. J. Schoelkopf, "Superconducting circuits for quantum information: An outlook," *Science* **339** 6124, 1169–1174 (2013).

[44] D. D. Awschalom et al., "Quantum spintronics: Engineering and manipulating atom-like spins in semiconductors," *Science* **339** 6124, 1174–1179 (2013).

[45] M. Veldhorst et al., "A two-qubit logic gate in silicon," *Nature* **526** 7573, 410–414 (2015).

[46] C. Monroe and J. Kim, "Scaling the ion trap quantum processor," *Science* **339** 6124, 1164–1169 (2013).

[47] D. P. DiVincenzo, "The physical implementation of quantum computation," *Fortschritte der Physik* **48** 9-11, 771–783 (2000).

[48] D. Ristè et al., "Deterministic entanglement of superconducting qubits by parity measurement and feedback," *Nature* **502** 7471, 350–354 (2013).

[49] Y. Nakamura, C. D. Chen, and J. S. Tsai, "Spectroscopy of energy-level splitting between two macroscopic quantum states of charge coherently superposed by Josephson coupling," *Physical Review Letters* **79** 12, 2328–2331 (1997).

[50] Y. Nakamura, Y. A. Pashkin, and J. S. Tsai, "Coherent control of macroscopic quantum states in a single-Cooper-pair box," *Nature* **398** 6730, 786–788 (1999).

[51] J. Koch et al., "Charge-insensitive qubit design derived from the cooper pair box," *Physical Review A* **76** 4, 042319 (2007).

[52] A. A. Houck et al., "Life after charge noise: recent results with transmon qubits," *Quantum Information Processing* **8** 2-3, 105–115 (2009).

[53] D. Vion et al., "Manipulating the quantum state of an electrical circuit," *Science* **296** 5569, 886–889 (2002).

[54] T. Larsen et al., "Semiconductor-nanowire-based superconducting qubit," *Physical Review Letters* **115** 12, 127001 (2015).

[55] A. Blais et al., "Cavity quantum electrodynamics for superconducting electrical circuits: An architecture for quantum computation," *Physical Review A* **69** 6, 062320 (2004).

[56] A. Wallraff et al., "Strong coupling of a single photon to a superconducting qubit using circuit quantum electrodynamics," *Nature* **431** 7005, 162–167

(2004).

[57] C. Eichler et al., "Observation of entanglement between itinerant microwave photons and a superconducting qubit," *Physical Review Letters* **109** 24, 240501 (2012).

[58] D. I. Schuster et al., "ac stark shift and dephasing of a superconducting qubit strongly coupled to a cavity field," *Physical Review Letters* **94** 12, 123602 (2005).

[59] L. DiCarlo et al., "Demonstration of two-qubit algorithms with a superconducting quantum processor," *Nature* **460** 7252, 240–244 (2009).

[60] L. DiCarlo et al., "Preparation and measurement of three-qubit entanglement in a superconducting circuit," *Nature* **467** 7315, 574–578 (2010).

[61] J. Majer et al., "Coupling superconducting qubits via a cavity bus," *Nature* **449** 7161, 443–447 (2007).

[62] H. Paik et al., "Observation of high coherence in Josephson junction qubits measured in a three-dimensional circuit QED architecture," *Physical Review Letters* **107** 24, 240501 (2011).

[63] C. Rigetti et al., "Superconducting qubit in a waveguide cavity with a coherence time approaching 0.1 ms," *Physical Review B* **86** 10, 100506 (2012).

[64] M. T. Tuominen et al., "Experimental evidence for parity-based 2e periodicity in a superconducting single-electron tunneling transistor," *Physical Review Letters* **69** 13, 1997–2000 (1992).

[65] F. W. J. Hekking et al., "Coulomb blockade of two-electron tunneling," *Physical Review Letters* **70** 26, 4138–4141 (1993).

[66] P. Lafarge et al., "Measurement of the even-odd free-energy difference of an isolated superconductor," *Physical Review Letters* **70** 7, 994–997 (1993).

[67] B. Jankó and V. Ambegaokar, "Parity fluctuations between coulomb blockaded superconducting islands," *Physical Review Letters* **75** 6, 1154–1157 (1995).

[68] G. Catelani et al., "Quasiparticle relaxation of superconducting qubits in the presence of flux," *Physical Review Letters* **106** 7, 077002 (2011).

[69] R. Lutchyn, L. Glazman, and A. Larkin, "Quasiparticle decay rate of Josephson charge qubit oscillations," *Physical Review B* **72** 1, 014517 (2005).

[70] M. D. Shaw et al., "Kinetics of nonequilibrium quasiparticle tunneling in superconducting charge qubits," *Physical Review B* **78** 2, 024503 (2008).

[71] J. M. Martinis, M. Ansmann, and J. Aumentado, "Energy decay in

superconducting Josephson-junction qubits from nonequilibrium quasiparticle excitations," *Physical Review Letters* **103** 9, 097002 (2009).

[72] J. Aumentado et al., "Nonequilibrium Quasiparticles and 2*e* Periodicity in Single-Cooper-Pair Transistors," *Physical Review Letters* **92** 6, 066802 (2004).

[73] A. J. Ferguson et al., "Microsecond resolution of quasiparticle tunneling in the single-Cooper-pair transistor," *Physical Review Letters* **97** 10, 106603 (2006).

[74] N. Court et al., "Quantitative study of quasiparticle traps using the single-Cooper-pair transistor," *Physical Review B* **77** 10, 100501 (2008).

[75] M. H. Ansari, "Rate of tunneling nonequilibrium quasiparticles in superconducting qubits," *Superconductor Science and Technology* **28** 4, 045005 (2015).

[76] H. Q. Nguyen et al., "Trapping hot quasi-particles in a high-power superconducting electronic cooler," *New Journal of Physics* **15** 8, 085013 (2013).

[77] C. Wang et al., "Measurement and control of quasiparticle dynamics in a superconducting qubit," *Nature Communications* **5** 5836 (2014).

[78] S. Gustavsson et al., "Suppressing relaxation in superconducting qubits by quasiparticle pumping," *Science* **354** 6319, 1573–1577 (2016).

[79] G. Vardulakis et al., "Superconducting kinetic inductance detectors for astrophysics," *Measurement Science and Technology* **19** 1, 015509 (2007).

[80] P. K. Day et al., "A broadband superconducting detector suitable for use in large arrays," *Nature* **425** 6960, 817–821 (2003).

[81] P. J. de Visser et al., "Number Fluctuations of Sparse Quasiparticles in a Superconductor," *Physical Review Letters* **106** 16, 167004 (2011).

[82] P. de Visser and J. Baselmans, "Microwave-induced excess quasiparticles in superconducting resonators measured through correlated conductivity fluctuations," *Applied Physics Letters* **100** 16, 162601 (2012).

[83] F. Giazotto et al., "Opportunities for mesoscopics in thermometry and refrigeration: Physics and applications," *Reviews of Modern Physics* **78** 1, 217–274 (2006).

[84] K. Y. Tan et al., "Quantum-circuit refrigerator," *Nature Communications* **8** 15189 (2017).

[85] H. Nguyen et al., "Sub-50-mK electronic cooling with large-area superconducting tunnel junctions," *Physical Review Applied* **2** 5, 054001

(2014).

[86] J. Zmuidzinas and P. Richards, "Superconducting detectors and mixers for millimeter and submillimeter astrophysics," *Proceedings of the IEEE* **92** 10, 1597–1616 (2004).

[87] R. H. Hadfield, "Single-photon detectors for optical quantum information applications," *Nature Photonics* **3** 12, 696–705 (2009).

[88] S. Miki, F. Marsili, and A. Casaburi, "Recent research trends for superconducting detectors: introduction for the special issue 'focus on superconducting dectectors'," *Superconductor Science and Technology* **29** 5, 050301 (2016).

[89] P. Recher, E. Sukhorukov, and D. Loss, "Andreev tunneling, Coulomb blockade, and resonant transport of nonlocal spin-entangled electrons," *Physical Review B* **63** 16, 165314 (2001).

[90] M. Ansmann et al., "Violation of bell's inequality in Josephson phase qubits," *Nature* **461** 7263, 504–506 (2009).

[91] A. Das et al., "High-efficiency Cooper pair splitting demonstrated by two-particle conductance resonance and positive noise cross-correlation.," *Nature Communications* **3** 1165 (2012).

[92] J. Schindele, A. Baumgartner, and C. Schönenberger, "Near-Unity Cooper Pair Splitting Efficiency," *Physical Review Letters* **109** 15, 157002 (2012).

[93] O. Naaman and J. Aumentado, "Poisson Transition Rates from Time-Domain Measurements with a Finite Bandwidth," *Physical Review Letters* **96** 10, 100201 (2006).

[94] V. F. Maisi et al., "Excitation of single quasiparticles in a small superconducting Al island connected to normal-metal leads by tunnel junctions," *Physical Review Letters* **111** 14, 147001 (2013).

[95] J. R. Petta et al., "Manipulation of a single charge in a double quantum dot," *Physical Review Letters* **93** 18, 186802 (2004).

[96] J. R. Petta et al., "Coherent manipulation of coupled electron spins in semiconductor quantum dots," *Science* **309** 5744, 2180–2184 (2005).

[97] R. Hanson and D. D. Awschalom, "Coherent manipulation of single spins in semiconductors," *Nature* **453** 7198, 1043–1049 (2008).

[98] A. J. Ferguson, "The Superconducting Spin Qubit," 2011. EPSRC Grant Proposal.

[99] J. P. Pekola et al., "Environment-Assisted Tunneling as an Origin of the Dynes Density of States," *Physical Review Letters* **105** 2, 026803 (2010).

[100] S. A. Kivelson and D. S. Rokhsar, "Bogoliubov quasiparticles, spinons, and spin-charge decoupling in superconductors," *Physical Review B* **41** 16, 11693–11696 (1990).

[101] J. F. Cochran and D. E. Mapother, "Superconducting transition in aluminum," *Physical Review* **111** 1, 132–142 (1958).

[102] R. Meservey and P. M. Tedrow, "Properties of very thin aluminum films," *Journal of Applied Physics* **42** 1, 51–53 (1971).

[103] N. A. Court, A. J. Ferguson, and R. G. Clark, "Energy gap measurement of nanostructured aluminium thin films for single Cooper-pair devices," *Superconductor Science and Technology* **21** 1, 015013 (2007).

[104] R. Dynes, V. Narayanamurti, and J. Garno, "Direct measurement of quasiparticle-lifetime broadening in a strong-coupled superconductor," *Physical Review Letters* **41** 21, 1509–1512 (1978).

[105] C. M. Wilson and D. E. Prober, "Quasiparticle number fluctuations in superconductors," *Physical Review B* **69** 9, 094524 (2004).

[106] H. Grabert and M. H. Devoret, *Single Charge Tunneling: Coulomb Blockade Phenomena in Nanostructures*. Plenum Press, 1992.

[107] P. Lafarge et al., "Direct observation of macroscopic charge quantization," *Zeitschrift für Physik B: Condensed Matter* **85** 3, 327–332 (1991).

[108] P. Lafarge et al., "Two-electron quantization of the charge on a superconductor," *Nature* **365** 6445, 422–424 (1993).

[109] N. A. Court, *Quasiparticle Dynamics in a Single Cooper-Pair Transistor*. PhD thesis, University of New South Wales, 2008.

[110] T. T. Tero T. Heikkilä, *The Physics of Nanoelectronics: Transport and Fluctuation Phenomena at Low Temperatures*. OUP, 2013.

[111] C. W. J. Beenakker, "Theory of coulomb-blockade oscillations in the conductance of a quantum dot," *Physical Review B* **44** 4, 1646–1656 (1991).

[112] L. P. Kouwenhoven, D. G. Austing, and S. Tarucha, "Few-electron quantum dots," *Reports on Progress in Physics* **64** 6, 701 (2001).

[113] W. G. van der Wiel et al., "Electron transport through double quantum dots," *Reviews of Modern Physics* **75** 1, 1–22 (2002).

[114] R. Hanson et al., "Spins in few-electron quantum dots," *Reviews of Modern*

146

Physics **79** 4, 1217–1265 (2007).

[115] Y. A. Pashkin et al., "Quantum oscillations in two coupled charge qubits," *Nature* **421** 6925, 823–826 (2003).

[116] K. D. Petersson et al., "Quantum coherence in a one-electron semiconductor charge qubit," *Physical Review Letters* **105** 24, 246804 (2010).

[117] J. Binney and D. Skinner, *The Physics of Quantum Mechanics*. Oxford University Press, 2014.

[118] C. Heij, *Single-charge transport in coupled nanostructures*. PhD thesis, TU Delft, 2001.

[119] T. Duty et al., "Coherent dynamics of a Josephson charge qubit," *Physical Review B* **69** 14, 140503 (2004).

[120] M. Sillanpää et al., "Direct Observation of Josephson Capacitance," *Physical Review Letters* **95** 20, 206806 (2005).

[121] R. J. Schoelkopf et al., "The radio-frequency single-electron transistor (rf-set): A fast and ultrasensitive electrometer," *Science* **280** 5367, 1238–1242 (1998).

[122] K. W. Lehnert et al., "Measurement of the excited-state lifetime of a microelectronic circuit," *Physical Review Letters* **90** 2, 027002 (2003).

[123] M. Field et al., "Measurements of coulomb blockade with a noninvasive voltage probe," *Physical Review Letters* **70** 1311–1314 (1993).

[124] L. DiCarlo et al., "Differential charge sensing and charge delocalization in a tunable double quantum dot," *Physical Review Letters* **92** 22, 226801 (2004).

[125] F. Persson et al., "Excess dissipation in a single-electron box: The sisyphus resistance," *Nano Letters* **10** 3, 953–957 (2010).

[126] S. Mukherjee, M. Manninen, and P. S. Deo, "Quantum capacitance: A microscopic derivation," *Physica E: Low-dimensional Systems and Nanostructures* **44** 1, 62 – 66 (2011).

[127] T. Duty et al., "Observation of quantum capacitance in the Cooper-pair transistor," *Physical Review Letters* **95** 20, 206807 (2005).

[128] R. Mizuta et al., "Quantum and tunneling capacitance in charge and spin qubits," *Physical Review B* **95** 4, 045414 (2017).

[129] M. Constantin, C. C. Yu, and J. M. Martinis, "Saturation of two-level systems and charge noise in Josephson junction qubits," *Physical Review B* **79** 9, 094520 (2009).

[130] N. J. Lambert. Private communication.

[131] G. C. O'Neil et al., "Quasiparticle density of states measurements in clean superconducting AlMn alloys," *Journal of Applied Physics* **107** 9, 093903 (2010).

[132] National High Magnetic Field Labratory, "Low Temperature Physics - The What, the How, the Why."
`https://nationalmaglab.org/education/magnet-academy/`
`learn-the-basics/stories/low-temperature-physics`.

[133] D. J. Cousins et al., "An advanced dilution refrigerator designed for the new lancaster microkelvin facility," *Journal of Low Temperature Physics* **114** 5/6, 547–570 (1999).

[134] F. Pobell, *Matter and Methods at Low Temperatures*. Springer-Verlag, 2007.

[135] A. Kent, *Experimental Low Temperature Physics*. Palgrave Macmillan, 1993.

[136] G. K. White and P. Meeson, *Experimental Techniques in Low-Temperature Physics (Monographs on the Physics & Chemistry of Materials)*. Oxford University Press, 2002.

[137] M. Shaw et al., "Quantum capacitance detector: A pair-breaking radiation detector based on the single cooper-pair box," *Physical Review B* **79** 14, 144511 (2009).

[138] B. I. Bleaney and B. Bleaney, *Electricity and Magnetism Vol. 1*. Oxford University Press, 2013. `http://www.ebook.de/de/product/18121948/b_`
`i_bleaney_b_bleaney_electricity_magnetism_v01_3e.html`.

[139] F. Persson, *Fast dynamics and measurements of single-charge devices*. PhD thesis, Chalmers University of Technology, 2010.

[140] L. Roschier, M. Sillanpää, and P. Hakonen, "Quantum capacitive phase detector," *Physical Review B* **71** 2, 024530 (2005).

[141] A. C. Betz et al., "Dispersively detected pauli spin-blockade in a silicon nanowire field-effect transistor," *Nano Letters* **15** 7, 4622–4627 (2015).

[142] T. Klaassen et al., "Absorbing coatings and diffuse reflectors for the herschel platform sub-millimeter spectrometers HIFI and PACS," in *Proceedings, IEEE Tenth International Conference on Terahertz Electronics*. IEEE, 2002.

[143] "Eccosorb SF information page."
`http://www.eccosorb.com/products-eccosorb-sf.htm`.

[144] H. Nyquist, "Thermal agitation of electric charge in conductors," *Physical Review* **32** 1, 110–113 (1928).

[145] C. Ciccarelli and A. J. Ferguson, "Impedance of the single-electron transistor at radio-frequencies," *New Journal of Physics* **13** 9, 093015 (2011).

[146] N. J. Lambert et al., "A charge parity ammeter," *Nano Letters* **14** 3, 1148–1152 (2014).

[147] G. B. Arfken and H. J. Weber, *Mathematical Methods for Physicists.* Elsevier LTD, Oxford, 2005.

[148] R. Fitzhugh, "Statistical properties of the asymmetric random telegraph signal, with applications to single-channel analysis," *Mathematical Biosciences* **64** 1, 75–89 (1983).

[149] M. Shaw et al., "Experimental realization of a differential charge qubit," *IEEE Transactions on Applied Superconductivity* **17** 2, 109–112 (2007).

[150] M. A. Sillanpää, L. Roschier, and P. J. Hakonen, "Inductive single-electron transistor," *Physical Review Letters* **93** 6, 066805 (2004).

[151] M. A. Sillanpää, L. Roschier, and P. J. Hakonen, "Charge sensitivity of the inductive single-electron transistor," *Applied Physics Letters* **87** 9, 092502 (2005).

[152] B. A. Turek et al., "Single-electron transistor backaction on the single-electron box," *Physical Review B* **71** 19, 193304 (2005).

[153] L. D. Landau and E. M. Lifshitz, *Statistical Physics.* Elsevier Science & Technology, 1980. `http://www.ebook.de/de/product/3024932/l_d_landau_e_m_lifshitz_statistical_physics.html`.

[154] A. Hädicke and W. Krech, "Tunneling through ultrasmall NIS junctions in terms of andreev reflection. a nonlinear response approach," *Physica Status Solidi* **191** 1, 129–139 (1995).

[155] A. D. Córcoles et al., "Protecting superconducting qubits from radiation," *Applied Physics Letters* **99** 18, 181906 (2011).

[156] L. Frunzio et al., "Fabrication and characterization of superconducting circuit QED devices for quantum computation," *IEEE Transactions on Appiled Superconductivity* **15** 2, 860–863 (2005).

[157] K. Inomata et al., "Single microwave-photon detector using an artificial λ-type three-level system," *Nature Communications* **7** 12303 (2016).

[158] H. Yang et al., "Extremely long quasiparticle spin lifetimes in superconducting aluminium using MgO tunnel spin injectors," *Nature Materials* **9** 7, 586–593 (2010).

[159] P. M. Echternach et al., "Progress in the development of a single Cooper-pair box qubit," *Quantum Information Processing* **8** 2-3, 183–198 (2009).

[160] C. M. Wilson et al., "Coherence times of dressed states of a superconducting qubit under extreme driving," *Physical Review Letters* **98** 25, 257003 (2007).

[161] A. Rossi, T. Ferrus, and D. A. Williams, "Electron temperature in electrically isolated Si double quantum dots," *Applied Physics Letters* **100** 13, 133503 (2012).

[162] M. Edwards, *Towards the detection of microwave light using superconducting quantum systems.* Phd thesis, University of Cambridge, 2015.

[163] D. Fang et al., "Electrical excitation and detection of magnetic dynamics with impedance matching," *Applied Physics Letters* **101** 18, 182402 (2012).

[164] R. Barends et al., "Coherent Josephson qubit suitable for scalable quantum integrated circuits," *Physical Review Letters* **111** 8, 080502 (2013).

[165] T. M. Buehler et al., "Single-shot readout with the radio-frequency single-electron transistor in the presence of charge noise," *Applied Physics Letters* **86** 14, 143117 (2005).

[166] A. Aassime et al., "Radio-frequency single-electron transistor as readout device for qubits: Charge sensitivity and backaction," *Physical Review Letters* **86** 15, 3376–3379 (2001).

[167] D. Loss and D. P. DiVincenzo, "Quantum computation with quantum dots," *Physical Review A* **57** 1, 120–126 (1998).

[168] J. J. Pla et al., "A single-atom electron spin qubit in silicon," *Nature* **489** 7417, 541–545 (2012).

[169] A. J. Ferguson et al., "Spin-dependent quasiparticle transport in aluminum single-electron transistors," *Physical Review Letters* **97** 8, 086602 (2006).

[170] C. H. L. Quay et al., "Quasiparticle spin resonance and coherence in superconducting aluminium," *Nature Communications* **6** 8660 (2015).